



Universitat de Girona

ADVANCES IN FIBRE BRAGG GRATING SENSORS FOR DAMAGE DETECTION IN COMPOSITE LAMINATES: APPLICATION IN QUASI-STATIC AND FATIGUE DELAMINATION TESTS

Daniel SANS CANOVAS

Dipòsit legal: Gi. 1001-2013

<http://hdl.handle.net/10803/117357>



Advances in fibre Bragg grating sensors for damage detection in composite laminates: application in quasi-static and fatigue delamination tests està subjecte a una llicència de [Reconeixement 3.0 No adaptada de Creative Commons](https://creativecommons.org/licenses/by/3.0/)

© 2013, Daniel Sans Canovas



UNIVERSITAT DE GIRONA

DOCTORAL THESIS

ADVANCES IN FIBRE BRAGG GRATING SENSORS FOR
DAMAGE DETECTION IN COMPOSITE LAMINATES:
APPLICATION IN QUASI-STATIC AND FATIGUE
DELAMINATION TESTS

DANIEL SANS CANOVAS

2013



UNIVERSITAT DE GIRONA

DOCTORAL THESIS

ADVANCES IN FIBRE BRAGG GRATING SENSORS FOR
DAMAGE DETECTION IN COMPOSITE LAMINATES:
APPLICATION IN QUASI-STATIC AND FATIGUE
DELAMINATION TESTS

DANIEL SANS CANOVAS

2013

TECHNOLOGY DOCTORATE PROGRAM

ADVISORS

DR. JOAN ANDREU MAYUGO MAJÓ
Universitat de Girona, Spain

DR. JORDI RENART CANALIAS
Universitat de Girona, Spain

A thesis submitted for the degree of Doctor by the
University of Girona

To whom it may concern,

Dr. Joan Andreu Mayugo Majó, Assistant Professor at the *Universitat de Girona* of the Department of *Enginyeria Mecànica i de la Construcció Industrial*, and Dr. Jordi Renart Canalias, Lecturer at the *Universitat de Girona* of the Department of *Enginyeria Mecànica i de la Construcció Industrial*,

CERTIFY that the study entitled *Advances in fibre Bragg grating sensors for damage detection in composite laminates: application in quasi-static and fatigue delamination tests* and submitted for the doctoral degree with International Mention, has, under their supervision, been carried out by Daniel Sans Canovas,

Girona, May 2013,

Dr. Joan Andreu Mayugo Majó
Universitat de Girona, Spain

Dr. Jordi Renart Canalias
Universitat de Girona, Spain

Dedicat a les persones a qui ho dec tot: els meus pares

Acknowledgements

Firstly, I would like to thank my advisors Dr. Joan Andreu Mayugo Majó and Dr. Jordi Renart Canalias for giving me the opportunity to carry out my thesis under their supervision. They guided my work over the past years, always making themselves available for discussions, the mechanics of writing scientific articles and solving any newly encountered problem. In particular, many thanks to Dr. Joan Andreu Mayugo Majó, who was the applicant for the Spanish Government projects (*TRA2006-15718-C02-01* and *DPI2009-08048*) under which my thesis was carried out.

Many thanks also to my colleagues in the Analysis and Advanced Materials for Structural Design research group who helped me enjoy an unforgettable time over these past years and for the invaluable discussions we have had related to my work. I would particularly like to mention the members of the lab who spent many hours assisting me with the tests I had to carry out. Special thanks are given to Prof. Josep Costa for his support in the technical writing process and for his availability to discuss any issue I put to him.

I also want to thank Dr. Malte Frövel from INTA for assisting me whenever I visited the INTA lab for manufacturing purposes, and for providing the experimental results, used in Chapter 3, to validate the simulations. Also César Gutierrez deserves a special acknowledgement for supplying the numerical spectra used for the discussions presented in Chapter 3.

I also want to state my gratitude to Prof. John Botsis for giving me the opportunity to visit the Laboratory of Applied Mechanics and Reliability at the *Ecole Polytechnique Fédérale de Lausanne* (EPFL). Many thanks also to the colleagues I met there during my research stay.

My parents have always supported me unconditionally and I feel extremely fortunate to have had them behind me at every step of my life. Throughout these past

years I have had nothing but encouragement from my family in my work, and for that I am grateful to Jaume, Marta and Oriol.

And last but not least, I would like to give my most heartfelt thanks to the person who is sharing her life with me, who supports me whatever, wherever, whenever, and who has infinite patience and comprehension, who, in short, has decided to love me unconditionally. Núria, gràcies de tot cor. Per tot.

Funds

The present work is within the framework of the Doctorate Technology Program of the *Universitat de Girona*. This thesis has been funded by the Spanish Government (*Ministerio de Economía y Competitividad*, MINECO, *Secretaria de Estado de Investigación, Desarrollo e Innovación*) through the research grant *BES-2007-14649* from the FPI program, and is within the framework of the EVISER (Virtual testing and structural monitoring of composite stiffened panels) and EVISER2 projects, of which are funded by the Spanish Government under the codes *TRA2006-15718-C02-01* and *DPI2009-08048*, respectively.

Part of the work has been carried out during a stage at the *Ecole Polytechnique Fédérale de Lausanne* (EPFL), under the mobility grant *SEST1000I001491XV0* from the MINECO FPI mobility program.

Publications

The present work has produced the following publications:

- Sans D., Stutz S., Renart J., Mayugo J.A., Botsis J. *Crack tip identification with long FBG sensors in mixed-mode delamination*, *Composite Structures*, 2012;94(9): 2879-2887. DOI: 10.1016/j.compstruct.2012.03.032
- Sans D., Renart J., Costa J., Gascons N., Mayugo J.A. *Assessment of the influence of the crack monitoring method in interlaminar fatigue tests using fibre Bragg grating sensors*, accepted for publication in the journal *Composite Science & Technology*, 2013. DOI: 10.1016/j.compscitech.2013.04.022

The present work has also produced the following conference presentations:

- Sans D., Mayugo J.A., Gascons N., Frövel M., Gutierrez C. *Optical fibre Bragg grating sensors embedded in Carbon/Epoxy laminates: numerical study of micromechanical behavior*, *COMATCOMP-09*, OCT-2009, San Sebastián, Spain.
- Sans D., Stutz S., Botsis, J., Mayugo J.A. *Characterization of mixed-mode delamination fracture with embedded long FBG sensors and numerical simulations*, *COMPTEST-2011*, FEB-2011, Lausanne, Switzerland.
- Sans D., Renart J., Mayugo J.A., Costa J. *Effect of the crack length monitoring technique during fatigue delamination testing on crack growth data*, *COMPTEST-2013*, APR-2013, Aalborg, Denmark.

List of Figures

2.1	FBG sensor response scheme	6
2.2	Coated FBG sensor scheme	6
2.3	Schematic of instrumented composite specimens	11
2.4	FBG spectrum of a thermally loaded composite specimen	12
2.5	Numerical model of embedded FBG with solid elements	12
2.6	Schematic of an instrumented epoxy specimen	13
2.7	Numerical model of an embedded FBG	14
2.8	Schematic and axisymmetric numerical model of an embedded FBG .	15
2.9	Response spectrum and relation to delamination length	16
2.10	Surface bonded FBG	18
2.11	Double notched specimen with an embedded FBG	20
2.12	Compact Tension specimen and loads scheme	21
2.13	T-Matrix simulated spectra and experimental response	22
2.14	DCB specimen with an embedded long FBG sensor	23
2.15	Instrumented aircraft skin panel	25
2.16	Details of multidirectional embedment configurations	26
2.17	FBG sensors network scheme	27
2.18	Instrumented sub-scale wing	28
3.1	Geometry and mesh of the 3D model	38
3.2	Geometry and mesh of the axisymmetric model	39
3.3	Discretisation of an optical fibre for T-Matrix	41
3.4	Experimental set-up of instrumented tensile composite samples	42
3.5	Longitudinal strain distributions through the cross-section	45
3.6	Distribution of the effective Poisson ratio	46

3.7	Distribution of the R_{max} indicator	47
3.8	Distribution of the $EPR - PR$ indicator	48
3.9	T-Matrix spectra of the axisymmetric models	50
3.10	T-Matrix spectrum of the three-dimensional model	53
4.1	Experimental samples scheme	60
4.2	Mixed-Mode Bending rig scheme	60
4.3	Detail of the lateral view of a marked sample	61
4.4	Comparison between stable and unstable crack propagation	63
4.5	Scheme of the MMB numerical model	66
4.6	Constitutive bilinear law of the cohesive elements	67
4.7	Experimental R-curve of the samples tested at 22% mode mixture	68
4.8	Experimental R-curve of the samples tested at 25% mode mixture	69
4.9	Experimental R-curve of the samples tested at 30% mode mixture	69
4.10	Experimental R-curve of the samples tested at 50% mode mixture	70
4.11	Experimental R-curve of the samples tested at 75% mode mixture	70
4.12	Fracture toughness against mode mixture	71
4.13	Sectional micrographs of an instrumented sample	72
4.14	P- δ curve of the samples tested at 22% mode mixture	73
4.15	P- δ curve of the samples tested at 25% mode mixture	74
4.16	P- δ curve of the samples tested at 30% mode mixture	74
4.17	P- δ curve of the samples tested at 50% mode mixture	75
4.18	P- δ curve of the samples tested at 75% mode mixture	75
4.19	Axial strain and gradient of the samples tested at 25%	77
4.20	Axial strain and gradient of the samples tested at 22% and 30%	78
4.21	Axial strain and gradient of the samples tested at 50% and 75%	79
4.22	Fracture surface of an opened sample	80
4.23	Fracture surface of different mode mixtures	81
5.1	Schematic of the experimental samples configuration	86
5.2	Detail of the lateral view of a marked sample	89
5.3	Axial strain as against the number of cycles measured by the FBGs	89
5.4	Potential fitting of the instrumented samples FAT1 and FAT2	92
5.5	Potential fitting of the non instrumented sample FAT3	93

LIST OF FIGURES

5.6	Fatigue crack propagation and statical critical energies	94
5.7	Fatigue crack propagation of the instrumented samples	96
5.8	Crack length against the number of loading cycles	98
5.9	Proposed correction to the visual method	99

List of Tables

3.1	Parameters involved in the embedment conditions	40
3.2	M21/T800 mechanical properties	43
3.3	Three-dimensional and axisymmetric numerical simulations results . .	49
3.4	Results of the experimental tensile test	52
4.1	AS4/8552 mechanical properties	59
4.2	Tests configuration and instrumented samples description	61
4.3	Parameters used for the MMB simulations	72
5.1	FBG Locations in relation to the loading points	87
5.2	Statical critical energies of the samples	91
5.3	Potential fitting parameters	93
5.4	Calculated Paris law parameters	97

List of Symbols

Symbol	Description
B	Mode mixture in an MMB test.
C	Compliance of the specimen.
E_{ii}	Young's moduli in ii direction.
E_s	Young modulus of the sensor.
E_c	Young modulus of the coating.
$EPR - PR$	Indicator accounting for a constant effective Poisson ratio over the measurements.
G_{ij}	Shear moduli in ij plane.
G	Fracture toughness.
G_I	Mode I fracture toughness.
G_{II}	Mode II fracture toughness.
G_C	Critical fracture toughness.
G_{IC}	Mode I critical fracture toughness.
G_{IIC}	Mode II critical fracture toughness.
G_c^{est}	Estimated critical fracture toughness for MMB test [1].
$G_{I\text{max}}$	Maximum or peak cyclic mode I strain energy release rate [2].
$G_{I\text{max}}^0$	Maximum or peak cyclic mode I strain energy release rate at the beginning of the test.
$G_{I\text{th}}$	Mode I energy threshold for which the crack propagation stops in a fatigue test.
K_i^s	Sensitivities to i strain component at the sensor.

Symbol	Description
K_T^s	Sensitivity to temperature at the sensor.
K_i^∞	Sensitivities to i strain component at the host.
K_T^∞	Sensitivity to temperature at the host.
K	Conversion factor from wavelength to strain.
K^{free}	Conversion factor from wavelength to strain of a non embedded optical fibre.
K_{norm}	Normalized conversion factor from wavelength to strain.
K_{AN}	Analytically calculated conversion factor.
K_{OPT}	Normalized conversion factor calculated in the models.
K_p	Penalty stiffness of the cohesive elements.
K_{Imax}	Maximum stress intensity factor per cycle in a fatigue test.
L_g	Grating length.
L_{eff}	Effective length for a tensile test.
L_c	Clamped length for a tensile test.
L	Half span of the MMB specimen [1].
N	Fatigue loading cycles.
P_g	Weight of the MMB rig.
P_c^{est}	Estimated critical load for MMB test [1].
P	Applied load.
P_{max}	Maximum load per cycle in a fatigue test.
Q	Material constant of the Paris law corresponding to the intercept in the straight part.
$R_{\text{max}}^{\text{intr}}$	Indicator accounting for the intrusiveness of the optical fibre.
R_{max}	Indicator accounting for a faithful strain measurement.
R_{host}	Radius of the host in the axisymmetric model.
R_s	Radius of the optical fibre.
R_c	Radius of the coating.
R	Amplitude ratio of a fatigue test.

Symbol	Description
a_0	Initial crack length.
a_f	Final crack length at the end of a delamination test.
a	Crack length.
b	Specimen's width.
c	Lever length of the MMB test apparatus [1].
c_g	Center of gravity of the MMB rig.
d	Damage variable of the cohesive elements.
d_{crack}	Distance from the crack surface to the FBG position in the thickness direction.
d_{FBG}	Distance from load application point to FBG inlet.
da/dN	Fatigue crack growth rate.
$\frac{dC}{da}$	Variation of the compliance with crack length increments.
$\frac{dn_0}{dT}$	Variation of n_0 with temperature changes.
h	Specimen's half thickness.
m	Material constant of the Paris law corresponding to the slope in the straight part.
n_0	Initial index of refraction.
p_{ij}	Photo-elastic coefficients.
p_e	Effective photo-elastic coefficient.
r^2	Correlation coefficient.
t	Teflon insert acting as delamination plane.
$\Delta\lambda_{\text{avg}}$	Shift of the Bragg wavelength.
ΔT	Temperature variations.
ΔG	Amplitude of the energy release rate in a fatigue test.
ΔK_{I}	Amplitude of the stress intensity factor in mode I in a fatigue test.
Δa	Difference between VIS and FBG methods measurements in a fatigue test.
α	Thermal expansion coefficient.

Symbol	Description
β	non-dimensional crack length correction for mode mixture [1].
γ	mode mixture transformation parameter for setting lever length [1].
δ	Applied displacement.
δ_{\max}	Maximum cycle applied displacement.
δ_{\min}	Minimum cycle applied displacement.
δ_{cr}	Critical displacement of a quasi-static test.
ε	Strain.
ε^{h}	Strain at the host with embedded optical fibre.
ε^{hnf}	Strain at the host without embedded optical fibre.
ε^{f}	Strain at the optical fibre.
η	Mode's interaction parameter.
λ_{B_0}	Bragg wavelength.
ν^*	Effective Poisson ratio (also abbreviated EPR).
ν_0	Initial effective Poisson ratio.
ν_{ij}	Poisson coefficient in ij plane.
ν_s	Poisson coefficient of the sensor.
ν_c	Poisson coefficient of the coating.
τ_3^0	Interface strength in mode I loading.
τ_{sh}^0	Interface strength in mode II loading.
χ	Crack length correction parameter [1].

List of Abbreviations

Abbreviation	Description
AR	Aspect ratio.
CFRP	Carbon fibre reinforced plastics.
DCB	Double cantilever beam test/specimen.
EPR	Effective Poisson ratio.
ERR	Energy release rate.
FBG	Fibre Bragg grating.
FEA	Finite element analysis.
MD	Multidirectional laminates.
MMB	Mixed mode bending test/specimen.
NL	Loss of the linearity point in a delamination test [1, 3].
OF	Optical fibre.
OLCR	Optical low-coherence reflectometry.
PTFE	Poly-tetra-fluor-ethylene.
PROP	Average value of the propagation points.
RN	Reference node.
SHM	Structural health monitoring.
SCB	Side clamped beam fixture.
UD	Unidirectional layers/laminates.
UV	Ultra violet light.
VIP	Visual initiation of the crack growth in a delamination test [1, 3].

Abbreviation	Description
VIS	Visual edge crack monitoring method.
VIS _c	Corrected visual edge crack monitoring method.
5% MAX	Minimum value between the 5% increment of the compliance [1, 3].

Contents

List of Figures	xv
List of Tables	xvii
List of Symbols	xix
List of Abbreviations	xxiii
Abstract	xxix
Resumen	xxxiii
Resum	xxxvii
1 Introduction	1
1.1 Motivation	1
1.2 Objectives	2
1.3 Thesis layout	3
2 State of the art	5
2.1 Introduction	5
2.2 FBG strain sensors	7
2.3 Damage monitoring with FBG sensors	16
2.4 SHM with FBG sensors	24
2.5 Summary	28
3 Reliability of uniform measurements	31
3.1 Introduction	31

3.2	Methodology	35
3.2.1	Indicators for reliable strain measurement	36
3.2.2	Numerical models	37
3.2.3	Transfer Matrix Method	40
3.2.4	Experimental set-up	42
3.3	Results and Discussion	43
3.3.1	Sensibility Analysis (model A)	43
3.3.2	Axisymmetric analysis (model B)	44
3.3.3	Experimental results	52
3.3.4	Three-dimensional analysis (model C)	52
3.4	Conclusions	54
4	Crack tip identification in MMB	57
4.1	Introduction	57
4.2	Methods and Materials	58
4.2.1	Materials and samples description	58
4.2.2	Mechanical testing	59
4.2.3	Strain measurements	64
4.2.4	Crack tip identifications	64
4.2.5	Numerical simulations	65
4.3	Results and Discussion	67
4.3.1	Identification of parameters for numerical modeling	67
4.3.2	Experimental and numerical results	72
4.3.3	Crack tip identifications	75
4.4	Conclusions	82
5	Real time fatigue monitoring	83
5.1	Introduction	83
5.2	Methodology	85
5.2.1	Specimens	85
5.2.2	Fatigue tests parameters	87
5.2.3	Determination of crack length	88
5.2.4	Strain measurements	90
5.3	Results and Discussion	91

<i>CONTENTS</i>	xxvii
5.4 Conclusions	100
6 Conclusions	103
6.1 Introduction	103
6.2 Conclusions	104
6.3 Future works	106
Bibliography	109

Abstract

The use of composite materials in industrial applications such as aeronautical, aerospace or wind energy production, has greatly increased in recent decades. Due to their inherent properties, these materials allow lighter, larger and more resistant structures. However, the use of composite materials for components or structures with highly stringent requirements, is hampered by the lack of knowledge of their reliability. In other words, new modes of fracture have to be understood, and controlled, in order to improve the design of composite structures and guarantee their load bearing mission. This issue has motivated research efforts in recent years, resulting in numerical models to simulate different damage mechanisms, the characterisation of materials, as well as different sensing methods that enable composite health to be monitored. One of the sensing methods that has evolved in recent years, is the use of embedded fibre Bragg grating sensors (FBGs), principally because of their adequacy to be embedded, their multiplexing capability and their low intrusiveness in the mechanical properties of the host. Since composite structures are layered structures, they are prone to delamination, and so a method to control or monitor these delaminations is required to help improve the reliability of these materials.

This work is divided into three main areas that contribute to the understanding of composites and the damage detection of such materials. In the first part of this thesis, some fundamental aspects about the use of fibre Bragg grating (FBG) sensors for internal strain measurements in composite laminates are discussed. The sensitivity factor K , which relates the axial strain to the sensor optical output, has been formulated in previous works under two principal assumptions. The first hypothesis assumes that the axial strain remains constant at the host and at the fibre, whereas

the second hypothesis postulates that there is no transverse strain coupled to the fibre from the host. The domain of validity of these assumptions is discussed for uniform strain measurements in this first part. Several numerical models of a unidirectional specimen under tensile loading have been implemented and validated with experimental tests for this purpose. The collected data allow the influence of parameters such as the effective length of the specimen, the thickness of the specimen, the Young's modulus of the coating and its radius, on the reliability of uniform strain measurements to be analysed. The analyses show that, when a sensor is embedded in a composite specimen under longitudinal loading conditions, the coupon aspect ratio (thickness-length relation) is the most influential parameter on the reliability of the strain measurements.

In the second principal work of this thesis, a highly accurate method for locating the crack tip position using long embedded Fibre Bragg Grating (FBG) sensors together with the Optical Low Coherence Reflectometry (OLCR) technique, is presented. With this technique the local Bragg wavelength over the whole grating is measured, and therefore, the axial strain profile within the grating can be evaluated. Carbon/epoxy samples are tested under different mode ratios through the standard Mixed-Mode Bending (MMB) test. Embedded long FBG sensors are used to measure the axial strain profile along the whole grating at different stages of the test. The crack tip can be precisely identified with the long embedded FBGs. The results are validated by means of a visual inspection after complete delamination of the sample. The results indicate that the long FBG sensor detects the crack tip inside the sample at least as precisely as the traditionally performed visual inspections carried out during the test by means of the lateral markings.

The third and final undertaking consists of developing an experimental application of FBGs to dynamic measurements. The FBGs are used to monitor a delamination fatigue test of composite coupons. One of the main experimental problems when performing delamination fatigue tests on composite materials is monitoring the crack length. Crack length is commonly monitored by means of travelling optical devices in a discrete representation and/or is derived from the specimen's previously calibrated compliance. In this part, an accurate method, based on the use of fibre

Bragg grating sensors, is proposed and applied to a carbon reinforced composite subjected to fatigue mode I loading through the well-known double cantilever beam (DCB) test. The results are compared to those achieved by visual inspection. From those results, an analysis of the crack growth rate curve is performed, and the Paris law parameters and energy threshold are calculated. Results indicate that optical inspection methods predict well the exponent in the Paris law equation, but the energy threshold is strongly dependent on the method used to measure the crack growth.

In summary, FBGs are studied through an in-depth literature review. Secondly, they are analysed, in terms of reliability, as strain sensors for uniform strain fields. Then, these sensors are used as crack tip detectors in a mixed-mode bending test. Finally, a practical application that justifies the use of FBGs in composites is proposed and developed. Results indicate that even though FBGs are an expensive alternative for monitoring the health of composite structures, their precision indicates the merit of the additional cost, in terms of advancing in the use of composites in high structural requirement composite components.

Resumen

El uso de materiales compuestos en aplicaciones de carácter industrial como por ejemplo la aeronáutica, aeroespacial o la producción de energía eólica, se ha visto enormemente incrementado a lo largo de las últimas décadas. Debido a sus extraordinarias propiedades, el uso de estos materiales permite la construcción de estructuras más ligeras, grandes y resistentes. Sin embargo, el uso de estos materiales en componentes o estructuras de alta responsabilidad estructural se ve coartado por la deficiencia de conocimiento sobre su fiabilidad estructural. En otras palabras, debido a la configuración de dichos materiales aparecen nuevos modos de fractura que deben ser comprendidos y controlados para mejorar el diseño de estructuras de material compuesto y garantizar, así, su misión como portadores de carga. Este tema ha motivado muchos esfuerzos en investigación durante los últimos años, concretamente en campos como la simulación numérica de diferentes mecanismos de daño, la caracterización de materiales o diferentes métodos de monitorización que permiten controlar la salud estructural de los materiales compuestos. Uno de los métodos de monitorización más prometedores y que más ha evolucionado en los últimos tiempos es el uso de fibras ópticas grabadas con redes de Bragg (FBG), principalmente, debido a características como su capacidad para ser embebidos sin que a su vez afecten el comportamiento mecánico del material huésped o su capacidad de multiplexión. Uno de los mecanismos de daño más común en los materiales compuestos, debido a que son estructuras laminadas, es la delaminación o daño interlaminar. Se antoja imprescindible, entonces, un método que permita monitorizar los crecimientos de grietas y que ayude a incrementar la fiabilidad de estos materiales.

El presente trabajo está dividido en tres tareas principales que contribuyen a la comprensión de los materiales compuestos y la detección de daño en estos materiales.

En la primera parte de la presente tesis se discuten algunos aspectos significantes sobre el uso de FBGs para medir campos de deformación en el interior de laminados de material compuesto. El factor de sensibilidad, K , que relaciona la deformación axial presente en el sensor (y a su vez de su material huésped) con la respuesta óptica del sensor, fue formulado en trabajos previos bajo dos premisas principales. Por una lado se asume que la deformación axial es constante en el material huésped y en el sensor, mientras por el otro se asume que no existe deformación transversal acoplada a la fibra óptica del material huésped. En ésta parte del trabajo se discute el dominio de validez de dichas premisas, para una configuración y un caso de carga concreto, cuando se usan estos sensores para medir campos de deformación uniformes. Se han implementado varios modelos numéricos a nivel micromecánico de un laminado unidireccional con un FBG embebido y se han simulado a cargas longitudinales. Uno de los modelos, el tridimensional, se ha validado mediante resultados experimentales. Los datos se han usado para analizar varios parámetros relacionados con el embebido, como por ejemplo la longitud efectiva y el grosor del espécimen y la rigidez y radio del recubrimiento. Los análisis muestran que cuando un sensor es embebido en una probeta de material compuesto bajo cargas longitudinales, la fiabilidad de la respuesta está fuertemente ligada a la relación de aspecto de la probeta.

En la segunda parte del presente trabajo se ha propuesto un método de localización de la punta de una grieta en crecimiento bajo cargas de modo mixto mediante sensores FBG largos junto a la técnica de interrogación conocida como *optical low coherence reflectometry* (OLCR). La mencionada técnica permite medir la longitud de onda local de Bragg a lo largo de toda la red, que a su vez se convierte en deformación axial. Se han ensayado probetas de material compuesto carbono/epoxi bajo diferentes modos de crecimiento de grieta. Los resultados experimentales han sido confirmados con las correspondientes simulaciones numéricas y mediante inspección visual de las superficies de fractura después de la completa delaminación. Los resultados obtenidos indican que los sensores largos son capaces de identificar la punta de la grieta por lo menos tan precisamente como los métodos visuales.

La tercera y última parte del presente trabajo consiste en desarrollar una aplicación práctica de los FBG en tiempo real. En este caso se utilizan varios sensores,

cortos y multiplexados, en una sola fibra óptica para monitorizar el crecimiento de grieta en ensayos a fatiga en modo I. Uno de los mayores problemas de este tipo de ensayos es, precisamente, la monitorización del crecimiento de grieta. Este proceso se realiza mediante cámaras o microscopios móviles en una representación discreta y/o se obtiene a partir de un análisis de flexibilidad. En esta parte se presenta un método preciso para la obtención de los parámetros necesarios para el diseño de materiales compuestos bajo cargas de fatiga en modo I mediante el ensayo conocido como doble viga en voladizo (del inglés *double cantilever beam* y su acrónimo DCB). Los resultados obtenidos mediante los FBG se comparan con los obtenidos mediante técnicas visuales. Estos resultados se usan para analizar las curvas de la velocidad de crecimiento de grieta y para calcular los parámetros que definen la ley de Paris. Los resultados obtenidos indican que, si bien ambos métodos estiman correctamente el exponente de la ley de Paris, el umbral energético de paro de crecimiento de grieta y la velocidad de crecimiento de grieta a un nivel de carga dado son muy dependientes del método usado para medir la grieta.

En resumen, se ha realizado un estudio profundo de los FBG mediante un detallado estado del arte. A continuación, se ha analizado, en términos de fiabilidad, el uso de FBGs como medidores de campos de deformación uniformes. Luego, estos sensores se han usado en una aplicación práctica para detectar la punta de la grieta en ensayos de delaminación a modo mixto. Y finalmente, se ha propuesto y analizado el uso de FBGs para monitorizar el crecimiento de grieta en tiempo real ayudando así a la evolución de métodos que permitan caracterizar más fielmente las propiedades de los materiales compuestos. Los resultados de la presente tesis indican que, aunque los sensores FBG son todavía una alternativa cara para monitorizar la salud estructural de estructuras de material compuesto, su precisión indica que, por el momento, el esfuerzo económico merece la pena en términos de la comprensión y certificación del uso de materiales compuestos como componentes estructurales portadores de carga.

Resum

L'ús de materials compostos en aplicacions de caràcter industrial com per exemple l'aeronàutica, aeroespacial o la de producció d'energia eòlica, ha crescut exponencialment durant les últimes dècades. Degut a les seves extraordinàries propietats, l'ús d'aquests materials permet la construcció d'estructures més lleugeres, grans i resistents. Tot i així, l'ús d'aquests materials en components d'alta responsabilitat estructural està limitat per la manca de coneixement en relació a la seva fiabilitat estructural. En altres paraules, degut a la configuració d'aquests materials, apareixen nous modes de fractura que han de ser compresos i controlats per tal de millorar-ne el disseny, i garantir, així, la seva missió com a elements estructurals. Aquest tema ha motivat molts esforços en investigació durant els últims anys, concretament en camps com la simulació numèrica de diferents mecanismes de dany, la caracterització de materials o diferents mètodes de monitorització que permeten controlar la salut estructural dels materials compostos. Un dels mètodes de monitorització més prometedors i que més ha evolucionat en els últims temps és l'ús de fibres òptiques gravades amb xarxes de Bragg (FBG), principalment, degut a característiques com la seva capacitat per a ser embeguts sense perjudici en el comportament mecànic del material hoste o la seva capacitat de multiplexió. Un dels mecanismes de dany més comú en els materials compostos, al ser estructures laminades, es la delaminació o dany interlaminar. Es torna imprescindible, llavors, un mètode que permeti monitoritzar els creixements d'esquerdes i que ajudi a incrementar la fiabilitat d'aquests materials.

Aquest treball està dividit en tres tasques principals que contribueixen a la comprensió dels materials compostos i a la detecció de dany en components d'aquests materials. En la primera part d'aquesta tesi es discuteixen alguns aspectes sig-

nificants sobre l'ús de FBGs per a mesurar camps de deformació en l'interior de laminats de material compòsit. El factor de sensibilitat, K , que relaciona la deformació axial del sensor (que a la vegada s'assumeix com la del material hoste en la zona del sensor) amb la resposta òptica del sensor, fou formulat en treballs previs sota l'assumpció de dues premisses. Mentre la primera assumeix que la deformació axial és constant tant al material hoste com a la fibra òptica, la segona predica que no hi ha deformació transversal acoblada del material hoste a la fibra òptica. En aquesta part del treball es discuteix el domini de validesa d'aquestes premisses, per a una configuració i un cas de càrrega concrets, quan aquests sensors s'utilitzen per a mesurar camps de deformació uniformes. S'han implementat diversos models numèrics a nivell micromecànic d'un laminat unidireccional amb un FBG embegut i s'han simulat sota càrregues longitudinals. Un dels models, el tridimensional, s'ha validat mitjançant resultats experimentals. Les dades s'han utilitzat per a analitzar diversos paràmetres relacionats amb l'embegut, com per exemple la longitud efectiva i el gruix de la proveta i la rigidesa i radi del recobriment. Els anàlisis mostren que quan un sensor és embegut en una proveta de material compost sota càrregues longitudinals, la fiabilitat de la resposta rau en la relació d'aspecte de la proveta.

En la segona part d'aquesta tesis s'ha proposat un mètode de localització de la punta d'una esquerda en creixement de mode mixt mitjançant sensors FBG llargs junt amb la tècnica d'interrogació coneguda com *optical low coherence reflectometry* (OLCR). Aquesta tècnica permet mesurar la longitud d'ona local de Bragg al llarg de tota la xarxa, que a la vegada es converteix en deformació axial. S'han assajat provetes de material compost carboni/epoxi sota diferents modes de propagació. Els resultats experimentals han estat confirmats amb les corresponents simulacions numèriques i mitjançant inspecció visual de les superfícies de fractura després de la completa delaminació. Les dades obtingudes indiquen que els sensors llargs són capaços d'identificar la punta de l'esquerda como a mínim tan precisament com els mètodes visuals.

La tercera i última part d'aquest treball consisteix en desenvolupar una aplicació pràctica dels FBG en temps real. En aquest cas s'han utilitzat sensors curts i multiplexats en una sola fibra òptica per a monitoritzar el creixement d'esquerda en

assaigs a fatiga en mode I. Un dels principals problemes d'aquest tipus d'assaig és, precisament, la monitorització del creixement d'esquerda. Aquest procés es realitza mitjançant càmeres o microscopis mòbils en una representació discreta i/o s'obté a partir d'un anàlisi de flexibilitat. En aquesta part es presenta un mètode precís per a l'obtenció dels paràmetres necessaris per al disseny de materials compostos subjectes a fatiga sota carregues de mode I mitjançant l'assaig conegut com doble biga en voladís (de l'anglès *double cantilever beam* i el seu acrònim DCB). Els resultats obtinguts amb els FBG es comparen amb els obtinguts mitjançant tècniques visuals. Aquests resultats es fan servir per analitzar les corbes de la velocitat de creixement d'esquerda i per calcular les paràmetres del material segons la llei de Paris. Els resultats obtinguts indiquen que, si bé ambdós mètodes estimen correctament l'exponent de la llei de Paris, el lliurar energètic on l'esquerda s'atura i la velocitat de creixement d'esquerda a un nivell de càrrega concret són molt dependents del mètode utilitzat per a mesurar l'esquerda.

En resum, s'ha realitzat un estudi profund dels FBG mitjançant un detallat estat de l'art. A continuació, s'ha analitzat, en termes de fiabilitat, l'ús de FBGs com a mesuradors de camps de deformació uniformes. Seguidament, s'han utilitzat aquests sensors en una aplicació pràctica per a detectar la punta d'esquerda en assaigs de delaminació en mode mixt. I finalment, s'ha proposat i analitzat l'ús de FBGs per a monitoritzar el creixement d'esquerda en temps real, contribuint així, al desenvolupament de mètodes que permetin caracteritzar més eficientment les propietats dels materials compostos. Els resultats d'aquesta tesis indiquen que, tot i que els sensors FBG són encara una alternativa cara per a monitoritzar la salut estructural d'estructures de material compost, la seva precisió indica que, per ara, l'esforç econòmic val la pena en termes de la comprensió i certificació de l'ús de materials compostos com a components estructurals portadors de càrrega.

Chapter 1

Introduction

1.1 Motivation

The use of composites has widely increased in industrial applications in recent decades, especially in those sectors where the properties of the composites are more appreciated. Aircraft, aerospace or wind blade turbine industries have been benefiting from the use of composites over the past years. The mechanical characteristics of composites such as a high specific stiffness (stiffness-weight relationship) or their resistance to corrosion, are remarkable qualities of such materials. Nevertheless, their applicability in elements of crucial structural integrity, is hampered by the difficulty of predicting life expectancy in service. That is to say their reliability. This difficulty arises from the amount of different damage mechanisms that can appear in a composite structure. These damage mechanisms are divided into interlaminar and intralaminar damage. The first group includes damage patterns such as fibre failure, matrix failure, or fibre-matrix debonding. The second group encompasses delaminations (i.e. the loss of adherence between two adjacent layers) that are mainly caused by fatigue or by an impact. Delaminations strongly affect the resistant capabilities of a composite component, and they are difficult to detect as they take place inside the structure, often being barely visible.

In order to predict the life expectancy in service of composite structures, technological developments in the sensing field for damage detection have been widely reported in recent years. The use of optical fibres as strain sensors is increasing due

to their capabilities of being able to be embedded in the material (by simply introducing a small intrusion), and to be multiplexed, which makes it possible to have several sensors in one optical fibre and one data acquisition equipment. Specifically, fibre Bragg grating sensors (from here on referred to as FBGs) are being increasingly used mainly because of their low intrusiveness, their precision and their capability to encode directly, in terms of wavelength, which leads to an output completely independent from light intensity or losses in connections or light source.

Characterising the behaviour of FBGs when embedded in composite laminates has become an appealing line of research because of the importance of knowing the micro-mechanical interactions produced between the sensor and the laminate. These micro-mechanical interactions modify the stress and strain fields in the optical fibre and the surrounding material and, at the same time, affect the sensor's reflected spectrum. In addition, FBGs are considered one of the best solutions for monitoring the health state of composites, and valuable information such as crack tip detection, or damage patterns identification can be achieved through their use from the reflected or transmitted spectrum. FBGs can also be used to characterise composites, as the monitoring of the crack length constitutes a key factor when measuring, for instance, the fracture toughness of composite coupons.

In summary, proving the suitability of FBGs to monitor the interior of composite structures, constitutes a promising research field to fully validate composites as structural elements of stability and integrity, and in particular, to predict their life expectancy in service.

1.2 Objectives

The main objective of the present work is to investigate the suitability of FBGs embedded in composite materials to measure changes in the strain field, and in turn, their applicability to detect delaminations when they are embedded in composite laminates. In order to achieve this aim, the following partial objectives are considered:

- To determine the applicability of embedded FBGs as strain sensors in com-

posite materials and analyse the reliability of the measurements principally in relation to the actual strain present in the host material and the shape of the optical spectrum.

- To obtain experimental evidence on the suitability of embedded FBGs to detect the crack tip in a delamination test. This is carried out by means of long FBGs embedded into composite coupons under mixed-mode delamination loading.
- To investigate the applicability of FBGs in fatigue delamination measurements. This is fulfilled by means of mode I fatigue delamination tests and multiplexed FBGs.

1.3 Thesis layout

This dissertation is divided into 6 chapters. **Chapter 1** is a first introduction to this work. An in-depth state of the art look at FBGs in laminate composites is presented and developed in **Chapter 2**, where the working principles of fibre Bragg grating sensors and their applications as strain and temperature sensors, as well as their capability as damage detectors within composite structures. A short review about the structural health monitoring (SHM) field is also included.

The main body of the thesis is structured as follows:

Chapter 3 presents a parametrical numerical study, supported by experimental results, on the reliability of the measurements carried out with FBG sensors. The working principles of FBG sensors are based on two main assumptions that make it possible to convert the Bragg wavelength shift into changes in the strain and temperature fields. The reliability of an FBG measurement principally depends on: (i) the homogeneity of the strain field in which the sensor is subjected, (ii) the coincidence of the strain state of the host material to that measured by the sensor and (iii) the compensation of transverse effects. In this chapter, the outcome of the formulation hypotheses is discussed for a single case, which helped to enhance the comprehension of the FBGs, their applicability, and enabled the initiation of the

use of FBGs for damage detection. This part was carried out with the collaboration of Dr. Malte Frövel from the *Instituto Nacional de Técnica Aeroespacial* (further known as INTA) and who provided the experimental results. César Gutiérrez also participated in this chapter providing the spectra of the simulated FBGs.

Chapter 4 deals with a particular application of long FBG sensors for monitoring the crack propagation in a mixed-mode delamination test. The suitability of long FBG sensors for detecting the crack tip position is proved and the differences of the crack tip measurement when measured at the coupon's side or by means of FBGs, are reported. The higher accuracy of FBGs measurements is also proved. This part also contains numerical simulations to support the experimental results for different mode mixtures. This work was carried out in the *Laboratoire de Mécanique Appliquée et d'Analyse de Fiabilité* (LMAAF) in the *Ecole Polytechnique Fédérale de Lausanne* (EPFL) under the supervision of Prof. Botsis and with the collaboration of Dr. Stutz. The expertise of the research group *Anàlisi i Materials Avançats per al Disseny Estructural* (AMADE) from the University of Girona was also fundamental in developing the mixed-mode delamination tests.

Chapter 5 presents an application of multiplexed FBGs for detecting the crack tip in a delamination mode I fatigue test. Composite coupons with embedded FBG arrays are led to mode I fatigue loading and the crack tip is discretely monitored at some positions both with FBGs and a travelling camera. In this part, it is proved that the measurements carried out by the FBGs are not only more accurate than visual measurements, but also more reliable throughout the test when it is displacement controlled. In this chapter it is proved that multiplexed FBGs are a valid tool to monitor the health of composite coupons, and by extension, of composite structures. This work was made possible thanks to the expertise of AMADE members in mode I fatigue loading and the opportunity to measure the FBGs locations in the LMAAF lab.

Chapter 6 concludes with the main achievements of this thesis and suggests issues that deserve further investigation.

Chapter 2

State of the art: FBG sensors in laminate composites

2.1 Introduction

An FBG sensor is an optical sensor recorded within the core of a standard optical fibre and whose principal characteristic is that it reflects a narrow bandwidth of light which responds faithfully to changes in temperature and strain fields (Fig. 2.1). This relationship between strain and temperature changes and the input wavelength shift becomes linear in the typical range of measurements in engineering applications. Hence, due to optical fibre's photosensitivity, changes in strains and temperature fields are obtained as a function of reflected bandwidth when the related parameters are known.

When an optical fibre is radiated by ultraviolet light the refractive index of the fibre changes. This effect is known as photosensitivity. As depicted by Hill and Meltz [4], the magnitude of the refractive index (Δn) depends on several factors such as the irradiation conditions, the composition of glassy materials forming the fibre core, or any processing of the fibre prior to irradiation. The typical irradiation conditions are an exposure to ultraviolet light for a few minutes at an intensity range of 100-1000 mJ/cm².

FBG sensors are usually coated in order to protect the optical fibre from the

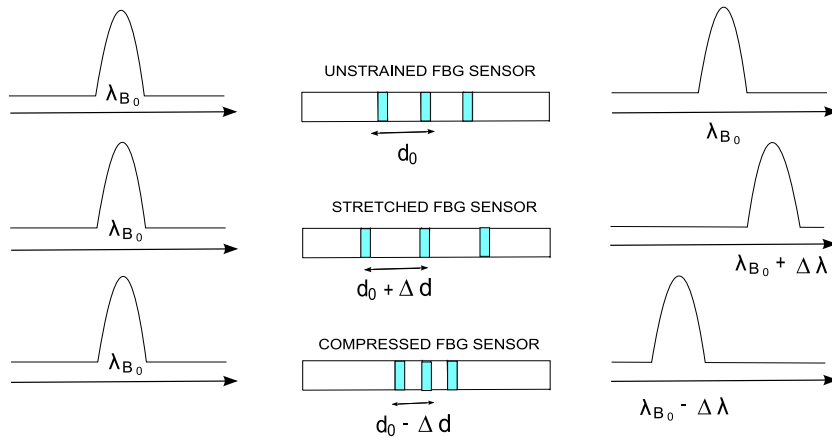


Figure 2.1: *FBG sensor response scheme, where λ_{B_0} is the input wavelength and the reflected bandwidth of an unstrained sensor (d_0), and $\Delta \lambda$ is the increment or decrement of the reflected bandwidth produced by a deformation of the sensor, Δd .*

environment and from being damaged during handling. Due to their dimensions (small radius) and mechanical properties, optical fibres are very fragile and difficult to manipulate. Fig. 2.2 depicts a scheme of a typical coated FBG sensor and its approximate dimensions.

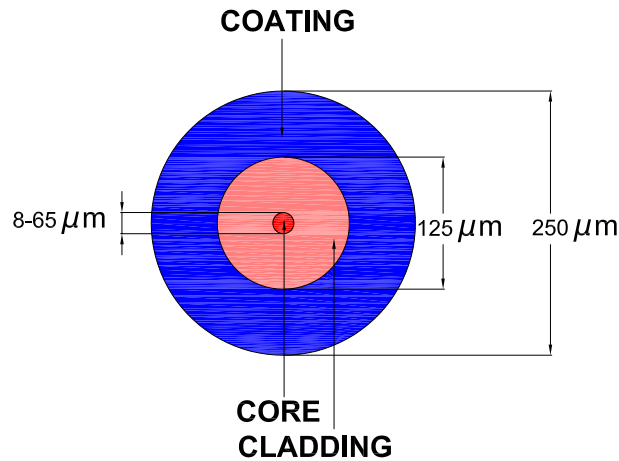


Figure 2.2: *Schematic of the transverse cross-section of a coated FBG sensor and typical dimensions.*

The interface between the sensor and the host material must be as compliant as possible because it has a marked effect on the reliability of the direct measurements

given by the sensor (Eaton *et al.* [5]). These measurements could be erroneous if the sensor is induced into non homogeneous strain fields. However, Li *et al.* [6] concluded that the strain transfer characteristics of fibre sensors depend on the mechanical properties of the interlayer, the host material, and the gauge length of the FBG sensor. In other words, the level of strain loss within the protective coating and the percentage transferred to the fibre core can be affected by the coating properties. The works developed by Stutz *et al.* [7, 8], where non coated sensors were used to increase the sensitivity of the sensor when subjected to non homogeneous strain fields, such as those produced near a crack tip, go in the direction of the use of non coated sensors.

2.2 FBG strain sensors in composite materials

An FBG sensor can be used to measure mechanical strains and temperature changes. These measurements can be carried out by the sensor either being bonded on the material surface or embedded in the host material. Prior studies have demonstrated that measurements given by the sensor when it is embedded, match with high confidence the measurement of the sensor when it is bonded (Frövel *et al.* [9]). The same authors also analysed the effects of the coating by comparing the results given by bonded sensors to the results obtained by embedded sensors without coating [10].

Van Steenkiste and Springer [11] developed a relationship between the strain and temperature changes and the shift in the reflected bandwidth as follows,

$$\frac{\Delta\lambda_{avg}}{\lambda_{B_0}} = K_1^s \varepsilon_1^s + K_h^s \varepsilon_h^s + K_d^s \varepsilon_d^s + K_4^s \varepsilon_4^s + K_5^s \varepsilon_5^s + K_6^s \varepsilon_6^s + K_T^s \Delta T^s \quad (2.1)$$

$$\frac{\Delta\lambda_{avg}}{\lambda_{B_0}} = K_1^\infty \varepsilon_1^\infty + K_h^\infty \varepsilon_h^\infty + K_d^\infty \varepsilon_d^\infty + K_4^\infty \varepsilon_4^\infty + K_5^\infty \varepsilon_5^\infty + K_6^\infty \varepsilon_6^\infty + K_T^\infty \Delta T^\infty \quad (2.2)$$

where $\Delta\lambda_{avg}$ is the wavelength shift, λ_{B_0} is the Bragg wavelength, K_i^s are the sensitivities of the sensor to every strain component at the sensor zone, K_i^∞ are the sensitivities of the sensor to every strain component at the host material zone, ε_i^s are the components of the strain field at the sensor zone and ε_i^∞ are the components of the strain field at the host material zone. K_T^s and K_T^∞ are the sensitivities to

temperature changes in the sensor and the host material, respectively, and ΔT^s and ΔT^∞ are the temperature changes in the sensor and the host material, respectively. For an isotropic sensor, embedded in a composite specimen in a direction parallel to the reinforcing fibres, the shift in the reflected wavelength becomes a function of the axial strain. According to Butter and Hocker [12], the relationship between $\Delta\lambda$ and the axial strain (ε_1) is formulated under two main assumptions: the first supposes that the axial strain is the same at both the host and the fibre, whereas the second assumption postulates that there is no transverse strain from the host coupled to the fibre.

Tang *et al.* [13] analysed the reliability of the measurements given by embedded FBGs from the point of view of the formulation hypotheses. In a numerical temperature analysis, different parameters, such as Young modulus of the host, optical fibre or coating, were analysed in order to check their effects on the reliability of the sensor measurements. It was concluded that, for this particular case, a thick host and a large FBG gauge length improved the effectiveness of the measurements. Moreover, the authors also concluded that a very stiff coating is beneficial for the strain transfer but, at the same time, it affects the calibration of the embedded sensors. The validation of the strain measurements by means of FBG sensors was also checked by Emmons *et al.* [14] reaching similar conclusions.

Li *et al.* [6] specifically studied the effects of the host material to the strain transfer coefficients when embedding an FBG sensor. The authors found from theoretical analysis that the strain transfer characteristics of fibre sensors depend on the mechanical properties of the interlayer, the host material, and the gauge length. In the same work, the shear modulus of the host was found to be a very important factor that influences the strain transfer. A similar study was carried out by Luyckx *et al.* [15] where multi-axial strain transfer was analysed by numerical means. The authors concluded that, even though an embedded FBG sensor is generally considered to be one of the best solutions for determining the internal strain field of composite elements, the strain measured is not necessarily equal to the one present in the structure. The authors attributed this discrepancy to the material and geometrical properties of the sensor and the host structure. The experimental validation of this

study was presented by Voet *et al.* [16]. Hadjiprocopiou *et al.* [17, 18] presented two numerical studies focused on the optimisation of the properties of the coating, concluding that an optimum interface coating aided to minimise the stress concentrations.

Liu *et al.* [19] and Kuang *et al.* [20] defined an effective parameter as that which relates the strain component along the fibre direction with the optical measurements. From Eqs. 2.1 and 2.2, neglecting temperature variations, and due to sensor-material configuration (where only K_1^∞ , K_h^∞ , K_1^s and K_h^s have a non zero value), this relationship is defined as

$$\frac{\Delta\lambda_{avg}}{\lambda_{B_0}} = (1 - p_e)\varepsilon_1^\infty \quad (2.3)$$

where p_e is the effective photo-elastic constant and ε_1^∞ is the strain at the host in the fibre direction. Frövel *et al.* [9, 10, 21–23] define this parameter, which relates the strain along the fibre direction and optical measurements, as K_{norm} . The authors describe this parameter as

$$K_{norm} = \frac{\frac{\Delta\lambda_{avg}}{\varepsilon_1^\infty}}{\lambda_{B_0}} = K_1^\infty - \nu_{12}K_h^\infty \quad (2.4)$$

where ν_{12} is the Poisson ration in the 1-2 plane of the host material. K_{norm} is used as a normalised conversion factor since it is divided by the axial strain of the host, that was measured with a strain gage.

From the previous works, it is concluded that the changes in strains in the FBG vicinity are directly related to changes of the reflected wavelength, and when the strain field is not uniform the wavelength depends on the position in the FBG. In order to determine the local wavelength along the FBG, a method based on the Optical Low Coherence Reflectometry (henceforth known as OLCR) technique and the layer peeling algorithm was used in [7, 24, 25]. In these works, where the length of the FBG was long enough to be subjected to a non uniform strain field, the relation between the local wavelength and the local axial strain along the Z axis, was

$$\frac{\Delta\lambda_B(z)}{\lambda_{B_0}} = (1 - p_e)\varepsilon_z(z) \quad (2.5)$$

where $\Delta\lambda_B(z)$ is the shift of the local wavelength (as it depends on z) and $\varepsilon_z(z)$ is the local Bragg wavelength in the fibre direction. This is a simplified form supposing no out-of-axis strain other than those created by Poisson's coefficient. In the case of short FBGs (for instance 1 mm long), the strain is considered to be constant over the sensors' length, and therefore the interrogation of the FBGs gives just one peak, perfectly shifted but not a distorted spectrum. With regards to the OLCR technique, this enables the measurement of the length, location and index of refraction modulation of the FBGs. The measurements of non-homogeneous strain fields were the principal benefit of this method [26], as the full strain distribution can be measured without the need to know the initial strain state. The OLCR technique has also been used to measure moisture absorption [27], residual strains from curing shrinkage [24] and to determine strains around cracks in pure epoxy [28] and composites [29], where fibre bridging parameters were also determined with the same technique.

Mulle *et al.* [30], carried out a non temperature dependent experiment to evaluate the thermal expansion of carbon/epoxy laminates with FBG sensors and compared it to other experimental techniques such as high temperature resisting foil gages or thermo-mechanical analysis. The studied specimens, shown in Fig. 2.3, were unidirectional and cross-ply laminates made up by M21/T700 stacked laminae. The authors concluded that in unidirectional (UD) specimens no transverse effects were observed, while in the multidirectional (MD) specimens (the 0-90 cross-ply laminates) the detected transverse effects were assumed to be responsible for the variations detected in the results.

Along similar lines, Güemes *et al.* [31] studied the response of the sensor under longitudinal and transverse stresses in a multidirectional laminate with a quasi-isotropic configuration. In this work, the authors analysed the spectral response of the Bragg gratings both before and after the build up of stresses during the curing and cooling stage, and before and after the stress released at the vicinity of a hole. The authors used the transfer matrix (T-matrix) method to estimate the longitudinal and transverse stresses given the measured wavelength shifts of the two peaks of

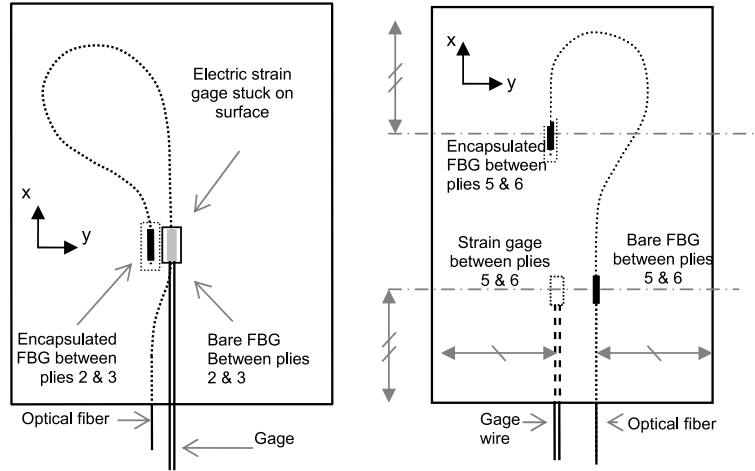


Figure 2.3: *Schematic representation of UD (left) and cross-ply (right) specimens and their instrumentation used for thermal expansion measurements. Source [30].*

the spectrum. This method divides the grating into sections with uniform coupling properties along the grating length, the 3D elements used in the specimen models need to be transformed into 2D elements for each cross-section in which the grating is divided. With this transformation done, and given any stress state in the sensor, the index of refraction value is first calculated along with the principal optical axes, for each individual element in each cross-section in the optical fibre. This calculation is made using a strain-optic law [11, 32]. Fig. 2.4 depicts the spectrum of the embedded FBG when unloaded and when thermally loaded. The authors observed that the FBG spectrum split when a thermal loading of $-20\text{ }^{\circ}\text{C}$ was applied, which was attributed to the laminate configuration. In fact, the multidirectional configuration induced thermal transverse residual stresses. Güemes and co-workers concluded that the transverse strain information caused by the transversal load, was contained in the bandwidth between the two split peaks of the reflected spectrum.

Prabhugoud and Peters [32] also used the T-matrix Method to obtain the response of embedded FBGs, presenting a methodology to apply this method to a Bragg grating strain sensor subjected to highly non uniform strain field. In all studied cases, the T-matrix approximation converged to solution. Fig. 2.5 depicts a numerical discretisation of an optical fibre for calculating the response spectrum from the stresses in the elements.

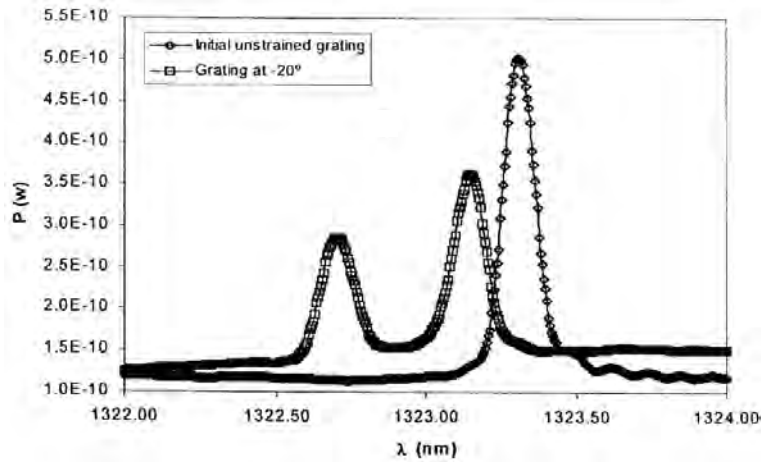


Figure 2.4: Spectra of an unstrained embedded FBG and a thermally loaded embedded FBG. Source [31].

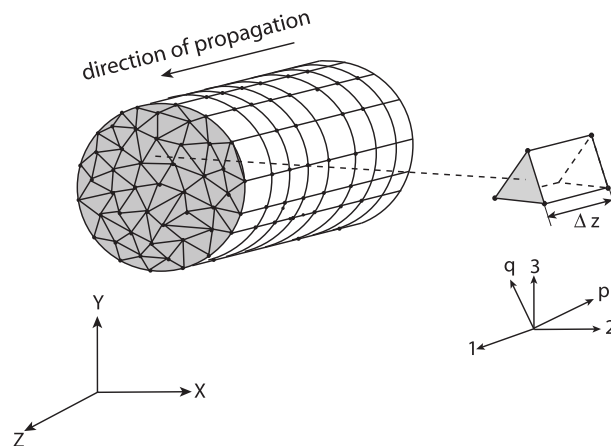


Figure 2.5: Discretisation of optical fibre into FBG sensor elements. X and Y are the global fibre axes, p and q are the local polarisation axes and 1-2-3 are the local principal axes. Source [33].

The effects of multi-axis strain sensitivities, and in particular the effects of transverse strains, were studied by Prabhugoud and Peters in [33–36]. The authors demonstrated, by analyzing the sensitivity of the FBG, that the highest sensitivity took place under transverse loading, and also showed that reducing the fibre cladding diameter significantly improves the sensitivity of the fibre to transverse loads. By analyzing different fibre types, Prabhugoud and Peters concluded that all of them exhibited the same sensitivity to thermal loading. When Prabhugoud and Peters

[33] formulated a Finite Element model of an embedded FBG, it was demonstrated that for any complicated loading conditions the response of the FBG allowed for a fast calculation. The numerical work carried out under diametrical compression, demonstrated the accuracy of their formulation.

Karalekas *et al.* [27] using FBG sensors, performed a methodological study to monitor the process induced strains (i.e. residual strains) in a single fibre composite. An embedded sensor in an epoxy cylindrical specimen (Fig. 2.6) was used to monitor the strain distribution along its axis when subjected to cycles of thermal ageing between 70° and 110° . By using the data from the FBG, the thermal expansion coefficient was evaluated and, based on the strain data from the FBG, numerical simulations were carried out to obtain the residual strain distribution in the specimen.

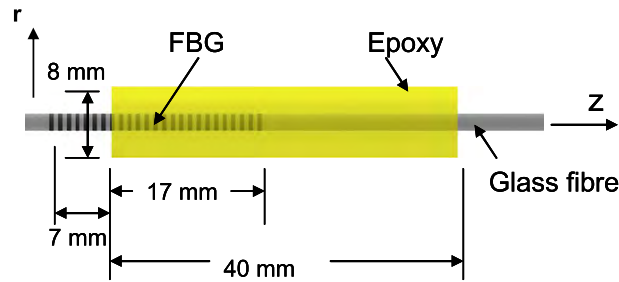


Figure 2.6: *Schematic representation of the cylindrical specimen with partly embedded long FBG.*
Source [27].

The results demonstrated the capabilities of the FBG sensors to provide useful information of the induced thermal strains and the curing degree during the production process. It was concluded that these data, supported by proper numerical models (Fig. 2.7), can lead to additional information for the knowledge of the curing processes in composites as well as aspects of fibre-matrix interface damage.

In previous articles in this same field of analysis of residual stresses with FBGs, Colpo *et al.* [24, 37] defined FBG sensors as excellent non-destructive tools for internal strain measurement in composite materials, especially when they are used simultaneously as sensor and reinforcement. In this study, long FBG sensors were

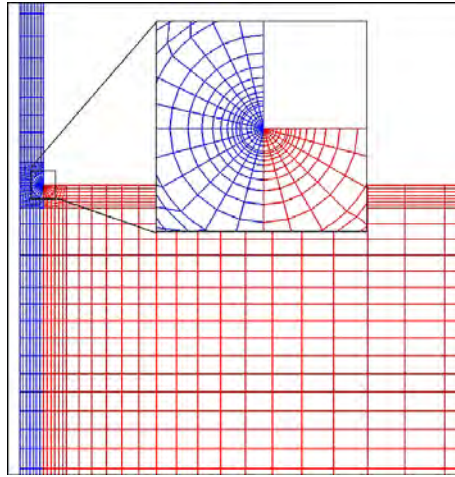


Figure 2.7: *Finite element mesh refinement to capture the local stress concentration at the interface between the fibre and the resin. Source [27].*

introduced in single fibre cylindrical specimens of epoxy in order to investigate the response to strain changes of the fibre due to shrinkage of the resin during polymerisation. In addition, Bragg wavelength distributions were determined as functions of the density of circumferential cracks in the radial direction, normal to the fibre. The experimental data together with numerical simulations were used to represent the complete residual stress field in the epoxy. The disturbance of the residual stress field, due to the presence of the fibre, was found to be extended up to 4 fibre radii (according to Van Steenkiste and Springer [11], the influence of the fibre on the strain fields reaches no more than two or three diameters of the fibre). The numerical results at the centre of the specimen matched very well with a theoretical model of a fibre in an infinite matrix. The shear stress transmission was well defined by the sufficiently refined radial mesh. The numerical simulations were performed with ABAQUS code (see Fig. 2.8). An axisymmetric model was implemented in order to reduce the calculating time. The authors paid special attention to simulating the fibre-matrix interface so as to have the interface shear stress well characterised.

Colpo *et al.* [24, 37] concluded that due to the ease of being embedded, FBG sensors can provide accurate strain measurements at selected locations. In this reviewed work, the grating response was analysed with the OLCR technique that enables for a full reconstruction of the strain profile over the grating. Besides, a

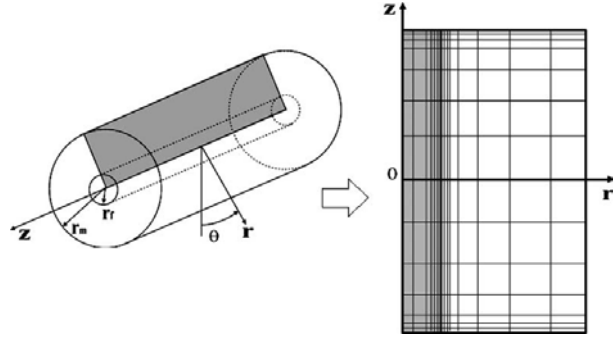


Figure 2.8: *Schema of the two-phase cylinder (left) and the numerical axisymmetric model (right).*
 Source [24].

three-dimensional model was implemented for simulating the effect of a longitudinal crack. Lai *et al.* [38] used embedded long FBGs to investigate the effect of nano/micro fillers in the residual strains evolution.

In relation to the works carried out by Eaton *et al.* [5] where the effects of the inclusion of the optical fibre in the host mechanical properties were analysed, Carrión *et al.* [39] confirmed that embedding sensors in CFRP laminates is safe for the mechanical integrity of polymeric structures. This is in good agreement with the work of Van Steenkiste and Springer [11], who wrote that strain and stress distributions in the material are modified by the presence of the sensor, but this information is already taken into account when formulating the sensitivities of the sensor to the far field strain and temperature changes. This was also confirmed by Takeda *et al.* [40]. A static tensile test was performed in order to confirm that the influence on the mechanical properties when embedding FBG sensors in composite laminates is negligible. The same conclusions were also confirmed by Güemes *et al.* [41]. Their work demonstrated that not only the effects of the intrusion were negligible (giving good results at tensile tests), but also the operativity of the fibre as strain sensors after all manufacturing processes (including autoclave curing and panel trimming) was kept. The authors showed that it is perfectly possible to embed optical fibre sensors into either flat panels or the web of structurally tailored stiffened panels. Optical fibre sensors were satisfactorily protected from external agents by the laminate itself and by a PTFE silicone-sealed tube.

2.3 Damage detection and identification with FBG sensors

Takeda is one of the most prolific authors in the field of damage detection and identification employing FBGs [30, 40, 42–48]. In one of these works, Takeda *et al.* [42] detected the delamination with a small diameter embedded FBG sensor. The relationship between the reflected spectra and the delamination size (Fig. 2.9) was clearly determined because the form of the spectrum changed sensitively as delamination length was growing. It was shown that the form of the spectrum strongly depends on the non-uniform strain distributions induced by the delamination. In addition, it was reported that the intensity ratio in the spectrum is an effective indicator for the prediction of the delamination length. The same authors used FBG sensors to detect the edge delamination in CFRP laminates under cyclic loading and in low velocity impact loading tests [40, 43]. Takeda and co-workers observed that under cyclic loading, the edge delamination is detected by the sensitive changes in the reflected spectrum.

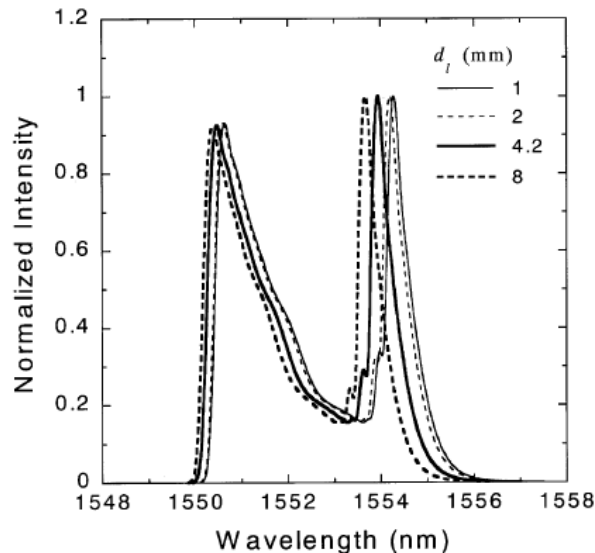


Figure 2.9: Influence of delamination length (d_t) on the reflection spectrum. Source [42].

Takeda *et al.* [30] reported a new approach for predicting multiple damage states with embedded FBG sensors. An optical analysis, connected with a numerical model

for damage analysis, is carried out to calculate the reflection spectrum of the FBG sensor. This linking enables them to calculate the reflection spectrum considering the damage process of the laminate. The reflection spectrum is strongly correlated with the longitudinal strain distribution of the FBG sensor, and each damage process has a characteristic reflection spectrum of the sensor. Yashiro *et al.* [44, 45] used FBG sensors to detect damage in CFRP open holed specimens. On one hand the authors show how to estimate a damage pattern with embedded FBG sensors [44]. The estimation of the damage patterns is carried out from the reflection spectrum, but different methods were used when estimating the applied strain. On the other hand the authors reported a numerical study and the experimental validation which confirms that the shape of the reflected spectrum is considerably deformed as the damage (splits, transverse cracks and delamination) near the hole extends [45]. It was also reported that the damage identification tool accurately estimates the damage patterns for the numerical model. As a final remark, Takeda *et al.* have also worked with chirped FBG sensors [46–48]. The main difference between these sensors and the standard ones is that the grating period is not constant. This feature gives a reflection spectrum that is not only composed by a peak, but also by a wide range of peaks.

Other noteworthy authors in this research field are Peters *et al.* [32, 49–57]. As introduced by the authors in [49], FBG reliability in the long term still remains questionable due to large-scale manufacturing difficulties and local stress concentrations because of interface between the sensor and host material. Knowing the state of the sensor, and separating it from the state of the host material, is very important to be confident of the information given by the sensor. The authors address the issue of separating sensor failure or degradation from that of the surrounding material. This work was carried out by analyzing the response of a surface mounted Bragg grating sensor during impact loading of a composite plate and its objective was to investigate the *debonding fibre-material*, *fibre degradation* and *fibre breakage* failure modes. The experimental setup of this work for an impact specimen is presented in Fig. 2.10.

After low-velocity impact tests and measuring the response spectra of the FBG,

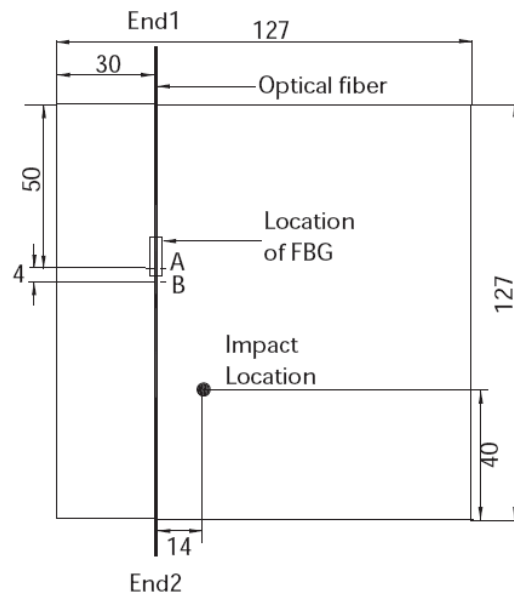


Figure 2.10: *Specimen with bonded optical fibre for impact test. A and B corresponds to breakage points on the optical fibre. Source [49].*

Prabhugoud and co-authors observed some failure in the grating such as debonding between the optical fibre and the specimen, misalignment between the two fibre cores at the location of the break, or a coupling between core and cladding modes due to changes in the conditions surrounding the optical fibre.

Along similar lines, Pearson *et al.* [53–55] obtained detailed information on the progression of damage in two-dimensional laminate woven composites in low-velocity impact experiments by means of both, embedded and surface mounted FBG sensors. Surface bonded and embedded FBG sensors were used to monitor the development of post impact residual strains in woven composites. The authors concluded that the embedded strain measurements indicate a reduction in through-the-thickness compression from fabrication after successive impacts.

Prabhugoud *et al.* [56, 57] presented an efficient interpretation algorithm for damage detection with embedded FBG sensors. The algorithm simulates the response of FBG sensors when subjected to multi-component loading. The aim of these works was to implement them in structural health monitoring (SHM) algorithms for

composites. A simulation method to determine the effects of axial, bending and shear loading on the response of an embedded FBG sensor was presented. This work first, experimentally verifies the effect of fibre bending on the Bragg grating. Then, a numerically efficient method to calculate the response of sensors embedded in unidirectional composites was developed using both FEA and optimal shear-lag theory. The application of their method was demonstrated by a numerical example which simulated the response of sensors embedded in one fibre layer to a transverse crack.

Peters *et al.* also analysed the response of embedded FBGs to non homogeneous strain fields such as those present in the stress concentrations zones [50–52], as seen in the work developed by Sorensen in her doctoral thesis [58]. The response of the FBG sensor to non-uniformity was studied in a compact tension specimen [50] and in a notched laminate [51]. The authors concluded that FBG sensors are suitable tools when embedded as strain sensors, even when the strain profile along the inscribed zone is not constant. When the applied strain is uniform, the shift in the wavelength of maximum reflectivity, which is linearly related to the axial strain, can be measured. However, when the strain field is non-uniform the spectrum is no longer a shifted single peak but rather changes the form as well.

These last works were carried out with the participation of Botsis and co-workers who have also been identified as expert authors in the FBG sensors field [7, 8, 25, 26, 28, 29, 50–52, 59, 60]. Following the works related to the use of FBGs in non homogeneous strain fields, Studer *et al.* [29] demonstrated that FBG sensors allow a distributed measurement along a known segment of the optical fibre whose length and location can be controlled during the grating recording, and then can be used to measure local effects due to debonding in composite materials. The authors presented a method using long FBG sensors, to determine micro-mechanical phenomena in composites such as crack bridging. This work demonstrated that embedding a long FBG into a reinforcing fibre allows the measurement of the bridging forces and the deduction of interface parameters. This technique does not require that the exact location of the crack was previously known. The authors also demonstrated that Bragg grating was sensitive enough to the bridging force, even for a

realistic case of an initially zero-width crack grown by fatigue. This feature mitigates the requirement to previously know the crack location in order to place the grating. It has been deduced that long gratings measure a strain distribution that gives important information on the matrix-fibre interface (such as slip or debond length) and the fibre-matrix frictional coefficient suitable for the validation of interface models. The authors presented the advantages that made the long FBG sensors a suitable tool for micro-mechanical investigation of the fracture mechanics in CFRP.

In the same research group and using FBG sensors, Ciaccari *et al.* [59] presented a new method for measuring non-uniform strain fields. This method is based on the measurement of the complex impulse response of the grating with the OLCR technique and the retrieval of the local Bragg wavelength through the layer-peeling technique. This study was focused on FBG sensors whose grating length was 24.1 mm. The sensors were embedded in double-edge-notched thin plates made of epoxy (see Fig. 2.11). The Bragg wavelength as well as the axial strain distribution were accurately retrieved along the grating from the measurement of the complex response of the FBG. The viability of non-uniform strain measurements was demonstrated for a single type of experiment which tested various geometrical and loading configurations. A good agreement between experimentally obtained strain distributions along the grating and the numerical simulations was obtained.

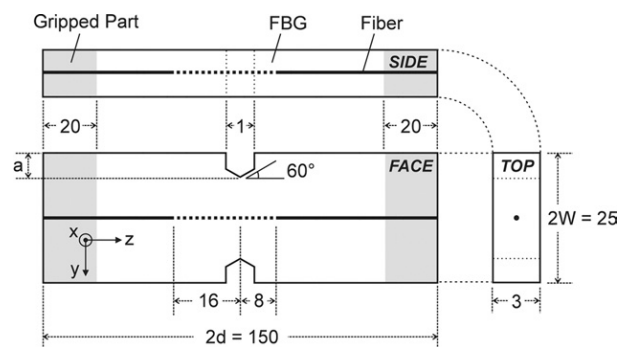


Figure 2.11: *Geometry of double-edge-notched specimen. Source [59].*

Colpo *et al.* [28] present an experimental numerical study of the long FBG sensors when placed near a crack tip. A long FBG sensor was positioned perpendicular to the crack growth direction in a Compact Tension specimen made by epoxy, as

shown in Fig. 2.12.

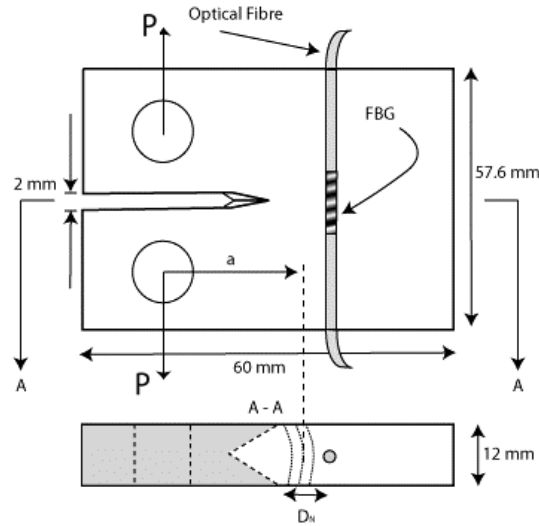


Figure 2.12: *CT specimen geometry and loads with an embedded long FBG sensor. Source [28].*

Two configurations were investigated: (a) when the fibre is ahead of the crack front, and (b) when the fibre is behind the crack front. Results indicated that simulated spectrum matched better with the experimental one when the FBG sensor was positioned ahead the crack front instead of being behind the crack tip (see Fig. 2.13).

The authors concluded that long FBG sensors combined with appropriate signal interrogation methods are very well suited tools for measuring distributed strain fields such as those attached to damaged zones. It was also concluded that the commonly used T-Matrix method fails when predicting strain profiles at highly non-uniform strain fields. With regards to the lacks of the T-matrix method, Prabhugoud *et al.* presented a modified T-Matrix method which accounts for these spectra modifications, but it has not been comprehensively checked by extensive experimental data [32]. Colpo *et al.* [28] concluded that the OLCR technique and the inverse scattering are, nowadays, one of the most advanced tools for directly characterising the local strain state in an FBG sensor. In addition, the accuracy of measurements was ensured by the agreement between experimental data and numerical simulations. Botsis *et al.* [26] demonstrated that that internal strain measurements by means of embedded FBG sensors, together with numerical modeling, are suitable tools for

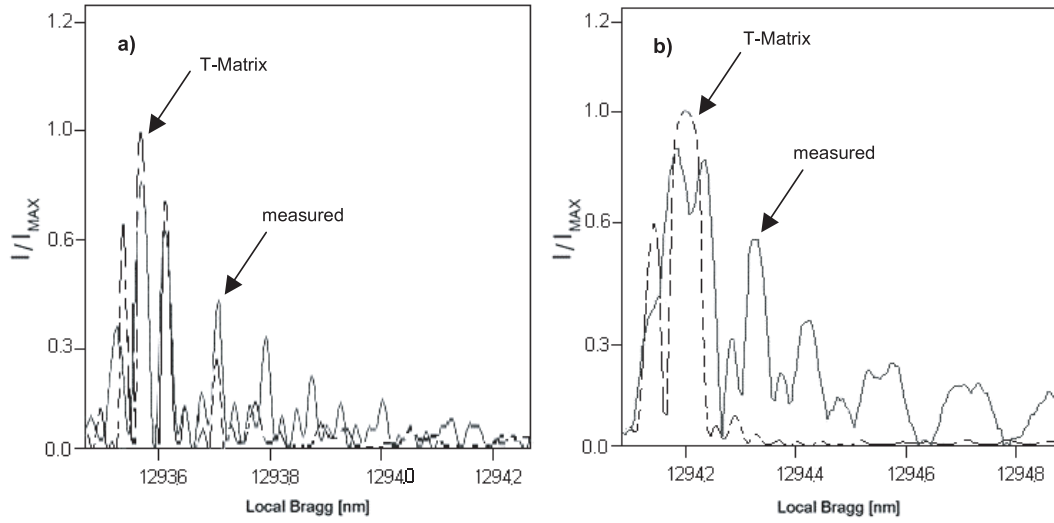


Figure 2.13: Measured and simulated spectra using the T-Matrix formulation for FBG sensor placed ahead the crack tip (a), and behind the crack tip (b). Source [28].

characterising the deformation and fracture behaviour of polymeric materials.

Sorensen *et al.* [25, 60] refers to bridging tractions measurement and simulation with FBG sensors. The works discuss bridging laws, determined from a novel methodology using distributed strains and an inverse-numerical technique, that are compared to those obtained using a method based on the experimental measurements of energy release rate and crack opening displacement. Both types of bridging laws were implemented in a numerical model that uses cohesive elements to calculate strains along the FBG sensor and to predict crack growth progression in a DCB specimen shown in Fig. 2.14. Global force-displacement responses were well described by the cohesive model. However, the J-integral method required an additional assumption about the length of the bridging zone. In addition, further parameters, such as initial stiffness or maximum stress, are needed to describe the crack initiation behaviour of the cohesive elements, which make simulating the crack front position and longitudinal strains more difficult. This work enabled the determination of bridging stress distributions in mode I delamination of uniaxial carbon reinforced composite specimens. When the bridging laws were implemented into a cohesive zone model, significant differences in load-displacement results, depending on the choice of the parameters involved in the J-integral approach, were

observed. The results of this work demonstrated that strain data from embedded long FBG sensors and inverse numerical identification provide an independent semi-experimental means for determining bridging laws that are useful for characterising delamination behaviour in polymer composites.

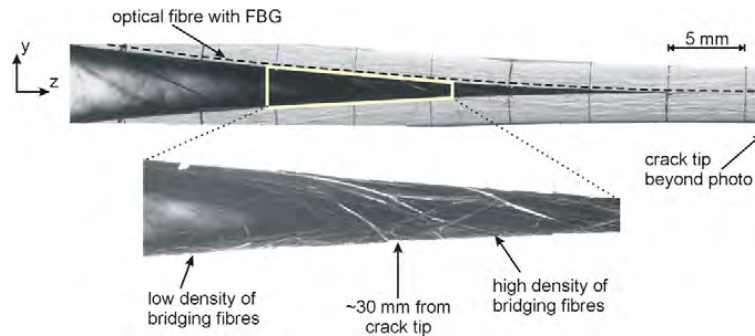


Figure 2.14: DCB specimen with an embedded FBG sensor aligned to the crack growth direction. Note the well developed delamination with bridging fibres. Source [60].

Following this work, Stutz *et al.* [7] presented a method to determine the bridging tractions for crack openings in mode I. The method was described as an inverse engineering solution by means of the OLCR technique and numerical modeling. The bridging tractions were determined by means of long FBGs in composite samples under quasi-static loading conditions.

Regarding the use of FBGs for dynamic measurements, Stutz *et al.* [8] reported the use of multiplexed FBGs to determine the fibre bridging in composite specimens under both fatigue and monotonic loading. Stutz also reported in his thesis [61] results on delamination analysis by means of FBG sensors embedded in composites under mode I and mode II loading conditions. Epaarachchi *et al.* [62] analysed the response of long FBGs embedded in glass fibre cross-ply composites under cyclic loading. It was concluded that the shape of the output FBG spectra contained valuable information about the composite structure such as local crack initiation/propagation stage. Silva-Muñoz *et al.* monitored the crack growth between composite structural joints with multiplexed FBGs [63]. 5 mm long FBGs were written into a single fibre and embedded in a composite double plate which was bonded to a composite base plate. The specimens were longitudinally loaded

under cyclic loading conditions. It was concluded that the strain evolution of the sensors changed as damage progressed and, in the case of study, the most suitable location of the sensors was the base plate, because it was close enough to the crack surface but also far enough to avoid the effects of the strain gradients. Bernasconi *et al.* [64] also used FBG sensors to monitor the fatigue crack growth in adhesively bonded joints of thick composite laminates. It was demonstrated that a resolution similar to that of ultrasonic testing could be achieved. Shin *et al.* [65] presented a quasi-continuous strain evolution over the number of cycles and which was obtained by means of multiplexed FBGs. The fatigue delamination was monitored in open-hole specimens.

2.4 FBG sensor networks for Structural Health Monitoring

As seen in Section 2.3, different damage types can be detected and identified depending on the shape of the reflected spectrum, which in turn depends on the induced strain field. The non homogeneity increases the distortion of the spectrum just as the non compensated transverse strains induce the peak splitting phenomenon. This effect, known as birefringence, causes the spectrum to split into two peaks that change their shape and become more and more separated as non uniformity increases. All these studies were carried out by inducing damage to a specimen with an embedded FBG sensor in a known position, and obviously a limit distance must exist for any sensor when embedded in the non homogeneous strain field zone. That is to say, the limit distance for detecting damage. At this point, it is important to remember that, as stated in Section 2.2, the inclusion of FBG sensors, since their diameter is very small, does not affect the host material in its mechanical properties. Therefore, one of the main characteristics of FBGs is the multiplexing capability, a composite structure can be monitored at different points with all the sensors in the same fibre, and in turn, the effects of such an SHM system does not affect the structure's mechanical behaviour.

Güemes *et al.* [41] studied the behaviour of an FBG sensor system subjected to non uniform strain fields. An experimental analysis of buckling in aircraft skin

panels was carried out with fibre optic sensors. They studied three blade stiffened CFRP panels with co-cured stiffener webs under compressive loads. The panels were instrumented with a system of six embedded fibre Bragg grating sensors. The sensors were located in the panels and in the stiffeners, as depicted in Fig. 2.15. The authors demonstrated that it is possible to embed optical fibre sensors not only in flat panels, but also in the web of structurally tailored stiffened panels. Optical fibres survived the manufacturing process including autoclave curing. Embedding an FBG network did not compromise the mechanical properties of the panel despite many sensors, as explained in the work of Fernandez [58], being used to reach reliable information of the health state of the structure. The main reason for the high number of sensors was that the sensibility of each sensor to a far damaged zone strongly depends on the distance.

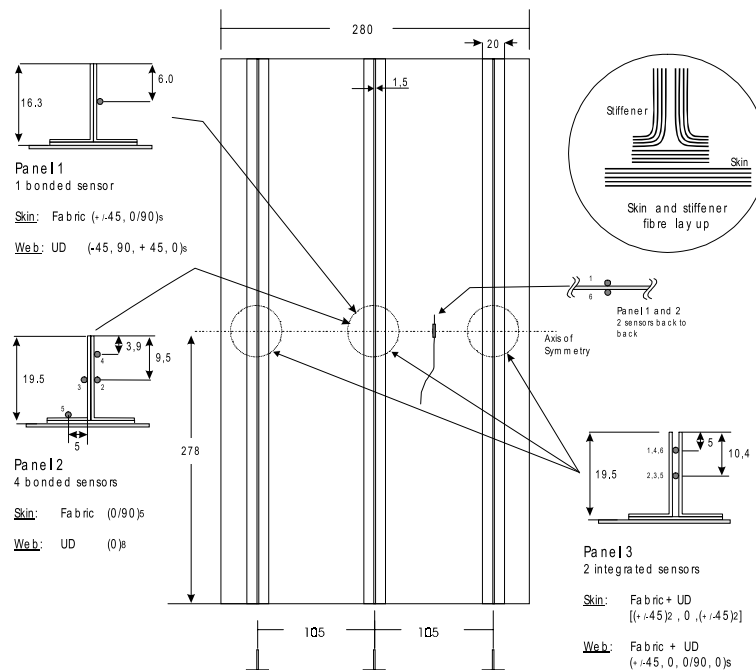


Figure 2.15: *Dimensions of the blade-stiffened panel with details of the instrumentation system for three different panels. Source [41].*

Fernandez [58] presented his thesis focused on FBG sensors as damage detectors. His work is focused on both FBG sensors and piezoelectric sensors for damage detection, and particularly centred on delamination monitoring and stiffeners debonding

from a composite panel detection via FBG sensors network placed in a determined way close to the zone where damage must appear. As concluded by Fernandez [58], the appearance of distributed sensors has been a revolution in the measurements field, and one which has an immediate application in the SHM field. The possibility of obtaining networks with a high density of integrated sensors enables, not only knowing exactly the strain field, but also enabling the study of local variations due to low density damage states with a very little intrusion in the structure.

Garret *et al.* [66–68] investigated on how to mount FBG networks and its optimisation for efficient damage detecting. The authors presented an optimised distribution of FBG sensors (see Fig. 2.16) for damage detection, and failure identification in composites under impact loading.

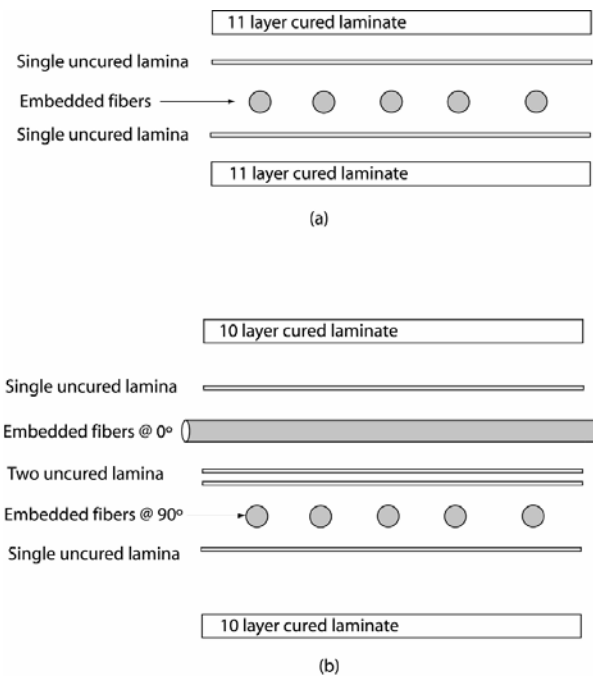


Figure 2.16: *Composite specimen configurations for (a) unidirectional embedment and (b) bidirectional embedment. Source [66]*

In this work, different densities (up to 6.3 optical fibres per centimeter) of optical fibres were embedded in composite laminates. Low-velocity impact damage responses were evaluated to determine the effects on the mechanical behaviour of

these laminates. It was concluded that for the particular 2D woven laminated composite system considered, relatively high densities of optical fibres were embedded between laminae without causing premature failure of the system during multiple low velocity impact events. Their results demonstrated the potential of embedding high density FBG sensor networks within woven composites to measure damage progression. Other configurations presented by Garret *et al.* [67, 68] are shown in Fig. 2.17.

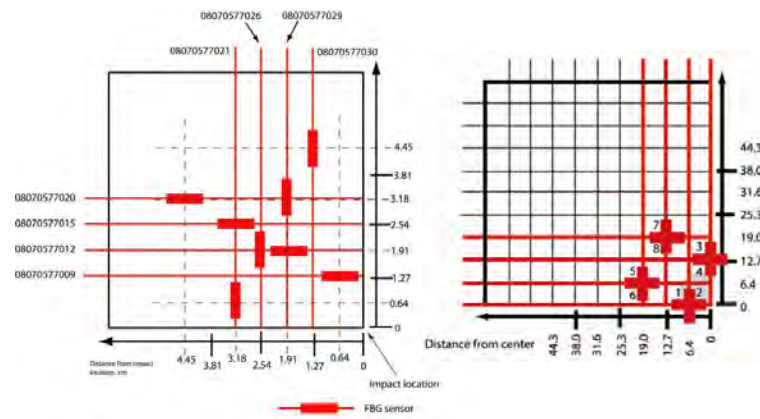


Figure 2.17: Schematic location of FBG sensors in laminate specimen. Only the upper left quadrant of specimen with impact location is shown. Source [67]

It is worth mentioning the work of another author who works in the field of practical applications for FBG sensor networks. Lee *et al.* [69] monitored the health of a sub-scale wing when it was in flight. In their article, FBG sensors were applied to measure dynamic strains inside a sub-scale wing under real-time wind tunnel testing. Apart from FBG sensors, electric strain gauges and PZT sensors were also used in that work, giving a good agreement in the measurements. Basically, the FBG sensor system used in the study was composed of a reference FBG sensor, two sensing FBG sensors and the required peripheral components such as interrogators. Fig. 2.18 depicts the configuration and geometry of the half sub-scale wing and the FBG sensors position.

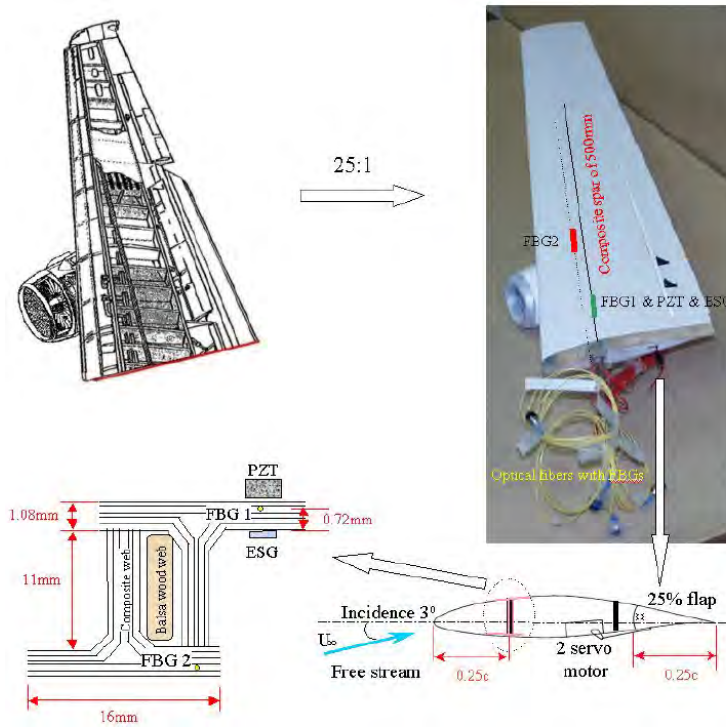


Figure 2.18: Configuration and geometry of the half sub-scale wing mounted by Lee et al. Source [69]

2.5 Summary

In this chapter, the state of the art applications in the field of fibre Bragg gratings is presented. The utility of the FBGs as embedded strain sensors was widely recognised early on. In terms of uniform strain fields and temperature sensing, it is desirable to have a clean response spectrum in order to make sure that the conversion into strains or temperatures fulfils the actual values within the samples. This is achieved if the formulation hypotheses are outcome, or in other words, when the transverse strains are compensated ($\varepsilon_2 = \varepsilon_3$), when FBGs are subjected to uniform strain fields, and finally when the strain transfer into the sensor is complete and the sensor measures the actual strain of the host material.

FBGs have also been widely used as damage detectors, either by analyzing the strain profile, or by extracting evidence from the response spectrum depending on the damage mode. The main problem for an FBG close to a damaged zone is

the non uniformity of the strain field. As explained, typical interrogation of FBG sensors only gives a spectral response, and when the grating length is subjected to an inhomogeneous strain field, the spectral response becomes distorted. Some authors have obtained valuable information from the distorted spectrum, but one of the most important contributions in recent years, and according to the author of this work's best knowledge, is the interrogation technique known as OLCR that allows a full reconstruction of the strain profile over the grating as well as accurately locating the FBGs within the optical fibre, along with the the use of short multiplexed FBGs where a uniform strain field that assesses a clean shift of the Bragg wavelength can be assumed. The most remarkable contributions in the review of the present literature are the work developed by Tang *et al.* [13] that in turn inspired the work developed in Chapter 3, the investigations developed by Botsis *et al.* [7, 8, 25, 26, 28, 29, 50–52, 59, 60] that motivated the work developed in Chapter 4 and finally the works developed by Stutz *et al.* [8] that inspired the investigation developed in Chapter 5.

Chapter 3

FBG sensor embedding conditions for reliable measurements of uniform strain fields

3.1 Introduction

In this chapter, the suitability of FBGs as strain sensors when embedded in composite laminates is discussed. The possibility of acquiring information about the strain state of the interior of a structure constitutes an important research line, because it can provide information about the health state of the component or structure. One of the best solutions for acquiring this information is embedding strain sensors within the composite parts. Fibre optic sensors, such as extrinsic and intrinsic Fabry-Perot interferometric sensors, distributed optical fibres [70] or Fibre Bragg Grating (FBG) sensors, are promising tools for monitoring the whole structure's state of health primarily because of their capability to be embedded. In particular, FBG sensors are being increasingly used to monitor and to measure the internal strain field of composite structures [5, 7–9, 20, 24, 26, 31, 33, 37, 38, 62, 63]. This is mainly due to their low intrusiveness [11, 39–41], or their capability to encode directly in terms of wavelength, which leads to a completely independent output to that of light intensity or losses in connections or light source. In summary, the main characteristics of these sensors are their light weight and small size, flexibility, immunity to electromagnetic fields and multiplexing capability.

When an FBG sensor is strained, the shift of the reflected Bragg wavelength ($\Delta\lambda$) is directly related to the axial strain of the fibre (ε_1) as follows:

$$\frac{\Delta\lambda}{\lambda_{B_0}} = K\varepsilon_1 \quad (3.1)$$

where $\Delta\lambda$ is the shift of the initial Bragg wavelength, λ_{B_0} is the initial Bragg wavelength, K is the sensitivity factor and ε_1 is the axial strain.

According to Van Steenkiste and Springer [11], the sensitivity factor K is formulated as

$$K = 1 - \frac{n_0^2}{2}[p_{12} - (p_{11} + p_{12})\nu^* - (\frac{2}{n_0^3} \frac{dn_0}{dT} + (p_{11} + 2p_{12})\alpha) \frac{\Delta T}{\varepsilon_1}] \quad (3.2)$$

where p_{ij} are the photoelastic coefficients, n_0 is the initial index of refraction, T is the temperature, α the thermal expansion coefficient and ν^* is the Effective Poisson Ratio (*EPR*) positively evaluated and it is expressed as

$$EPR = \nu^* = -\frac{(\varepsilon_2 + \varepsilon_3)/2}{\varepsilon_1} \quad (3.3)$$

where ε_2 and ε_3 are the transverse strains. In a transversely isotropic laminate, it can be assumed that ε_2 and ε_3 are equal, and consequently (Eq. 3.3) can be expressed as

$$EPR = \nu^* = -\frac{\varepsilon_2}{\varepsilon_1} \quad (3.4)$$

Considering that the temperature remains constant throughout the measurement, the sensitivity factor shown in (Eq. 3.2), only accounts for mechanical strain changes, and it is expressed as

$$K = 1 - \frac{n_0^2}{2}[p_{12} - (p_{11} + p_{12})\nu^*] \quad (3.5)$$

The relationship between $\Delta\lambda$ and ε_1 is formulated under two main assumptions [12]: the first supposes that the axial strain is the same at both the host and the fibre, whereas the second accepts that there is no transverse strain coupled to the fibre from the host. Therefore, when the FBG sensor is embedded into a host material it is possible to measure the internal strain field of the host. Nevertheless,

the precision of strain measurements given by the embedded optical sensor has to be assessed by checking the outcome of the assumptions. Prior analyses [10, 13, 22] demonstrated that the relationship between $\Delta\lambda$ and ε_1 is not constant through the grating under different load conditions. On the other hand, Emmons *et al.* [14] concluded that FBG sensors are a valid tool for accurate measurements in a case where the optical fibre is embedded parallel to the reinforcing fibres in a quasi-isotropic lay-up. The authors also concluded that constant strain fields could be measured, whereas non-uniform strain fields, as in the grips regions, were difficult to monitor because of the limitations of the formulation.

Botsis *et al.* [26] presented some essential aspects of FBG sensors such as a sensing system distinguishing between long FBG or short FBG sensors depending on the nature of the problem. On the one hand, long FBG sensors are normally subjected to non-uniform strain fields, thus requiring a complex interrogation method. On the other hand, when using short FBG sensors it is assumed that the strain field in the vicinity of the FBG is uniform over the grating. In a similar problem statement, Li *et al.* [6] concluded that studying the strain transfer between the FBG and the host material is essential for reliable measurements. The authors demonstrated that the mechanical properties of the interlayer, the host material and the length of the FBG, have a strong influence on the strain transfer under certain load conditions. Luyckx *et al.* [15, 16] concluded that, despite FBG sensors being considered one of the best solutions for determining the internal strain state of composite elements, the measured strain does not necessarily have to be equal to the actual strain field inside a structure. This discrepancy, as stated, is dependent on the material and geometrical properties of the sensor and the host structure. Other studies in the literature related to the stress concentration induced by embedded sensors [13, 17, 18, 71, 72] account for the parameters that give an optimal reduction of stress concentration under different load conditions.

According to the literature, the key to having a precise measurement is in calibrating the initial relationship between $\Delta\lambda$ and ε_1 , analyzing whether it remains constant through the geometry and the load story, and ensuring the agreement of the sensor and host axial strains. As demonstrated by Botsis *et al.* [26], when the

FBG is subjected to a non-uniform strain field, the local Bragg wavelength (λ_{B_0}) becomes a function of the axial position (z) in the FBG. Therefore, the axial strain is also expressed as a function of z . Consequently, when using an FBG with a determined grating length, in a simple linear interrogation, it has to be assumed by using Eq. 3.1, that the strain field is constant over the grating. Moreover, after a linear strain distribution is assumed, the spectral response of the FBG has to be faithful to the actual strain field within the sensor. This problem is resolved by assessing the outcome of the assumptions accepted for the formulation of the sensitivity factor K .

The first assumption, defined as the axial strains matching at both the fibre and the host, directly implies that there are insignificant or no effects on the host mechanical properties due to the intrusion produced by the inclusion of the optical fibre. In addition, this assumption is used to directly relate the host axial strain to the optical output. Therefore, a key issue is to determine whether the axial strains are equal in the host and in the fibre. The second assumption, related to transverse effects, is checked by evaluating the Poisson ratio of the embedded fibre over the grating length.

For a free sensor, EPR is equal to the Poisson ratio of the fibre and K is a constant. Nevertheless, when the fibre is embedded into a host, the absence of induced transverse deformations cannot be assured. Thus, the EPR can neither be taken as the initial Poisson ratio of the fibre nor as a predefined constant. The main method to check the second assumption outcome is to assess whether the EPR remains constant.

Tang *et al.* [13] analysed three critical issues by defining three indicators that accounted for the validity of the formulation assumptions. The first of which is the effect of embedding a fibre into the host mechanical properties. The second indicator accounts for the axial strains that have to be equal at the host and at the fibre. And the third is whether the EPR remains constant after calibration. In this chapter the same critical issues are dealt with in order to assess an accurate response of the FBG under uniform strain fields. Nevertheless, due to the nature of the problem some adaptations to the indicators developed by Tang *et al.* are

proposed. In addition, the analysis of the outcome of the formulation hypotheses is sustained by the corresponding reflection spectra of the FBGs that validate the results of the indicators. Also, a comparison between the numerical results of a three-dimensional model and the experimental results is carried out.

3.2 Methodology

This case study is focused on UD specimens under longitudinal loading conditions. Due to the nature of this case, the indicators presented by Tang *et al.* are firstly analysed to check their suitability to this loading case, and some of them are adapted in order to obtain more valuable information. As with Tang and co-workers, three indicators are used to check the reliability of the measurements given by the FBGs. The numerical part is performed using the commercial FEA software ANSYS® v11.0, and it is divided in three analyses. The first is a three-dimensional model (henceforth known as model A) implemented in the probabilistic design module of the aforementioned FEA software, in order to determine which mechanical properties are more highly correlated to the variations of the sensibility factor K . The second analysis is carried out by means of an axisymmetric model (henceforth known as model B) that performs the analysis of the described indicators. This model accounts for variations of geometrical parameters as well as the previously determined mechanical properties. The results of this numerical model are also used to obtain the reflected spectra of the FBG by means of the T-Matrix method. These spectra are used to sustain the expected reliability given by the indicators. The third analysis is performed through a three-dimensional model (model C). This model accounts for the geometries and dimensions (previously analysed parameters) of an actual sample. The value of the indicators for this sample's configurations are calculated as well as the numerical reflected spectrum. This model is validated by the experimental results obtained from tensile/compression test specimens instrumented with FBG sensors and strain gages. Only the tensile results are accounted for in this work since for the numerical models, the loading case is completely symmetric.

3.2.1 Indicators for reliable strain measurement

To perform a reliable strain measurement with an FBG sensor two assumptions have to be fulfilled: the first consists of having the same axial strain in the host and the optical fibre, whereas the second assumes that there is no transverse strain coupled from the host to the fibre. If there is, the Poisson ratio of the optical fibre has to be calibrated and has to be constant over both the whole grating and test. In addition, if the coupled transverse strain is not compensated in both directions, the peak splitting phenomenon appears. Nevertheless, as this work is performed in UD specimens, no decompensated transverse strains are expected. Tang *et al.* defined three issues to satisfy the validation of the formulation assumptions. At the same time, the authors defined 3 indicators to quantify the issues. In this section these indicators are adapted for the analysis of a tensile test of a composite specimen.

The first indicator that is proposed in [13], R_{\max}^{intr} , accounts for the longitudinal strain in the host with and without the fibre, and is defined as

$$R_{\max}^{\text{intr}} = \max \left(\left| \frac{\varepsilon_1^{\text{h}} - \varepsilon_1^{\text{hnf}}}{\varepsilon_1^{\text{hnf}}} \right| \right) \quad (3.6)$$

where ε_1^{h} is the axial strain of the host enveloping the fibre and $\varepsilon_1^{\text{hnf}}$ is the longitudinal strain of the host without the fibre.

Tang and co-authors used this indicator by giving the thermal imposed strain value to $\varepsilon_1^{\text{hnf}}$. In an isotropic laminate, and with a three principal thermal imposed strain, how the specimen behaves is known. Meanwhile, for specimens under mechanical longitudinal loading, the amount of material resistant to being deformed and the required length to reach it, cause the strain state in the centre of the specimen to be unpredictable. Hence, the same models without the optical fibre are performed to evaluate $\varepsilon_1^{\text{hnf}}$.

The second indicator accounts for the coincidence of the fibre and host axial strains, and in fact directly quantifies the accomplishment of the first assumption. It is expressed as

$$R_{\max} = \max \left(\left| \frac{\varepsilon_1^f - \varepsilon_1^h}{\varepsilon_1^h} \right| \right) \quad (3.7)$$

where ε_1^f is the axial strain of the fibre.

Finally, the third indicator, $EPR - PR$, accounts for whether the effective Poisson ratio remains constant after calibration. This indicator is defined as

$$EPR - PR = \frac{EPR}{PR} = \frac{\nu^*(z_0)}{\nu_0} \quad (3.8)$$

where ν_0 is the initial fibre's Poisson ratio and $\nu^*(z_0)$ defines the EPR at the most critical zone of the grating (z_0) further defined. This indicator is directly related to the second assumption, which assumes that there is no transverse strain coupled from the host to the fibre. According to Eq. 3.8, there is no coupling of the transversal strains when the EPR remains equal to the Poisson ratio of the optical fibre. The zone where the EPR is read differs to that used by Tang and co-authors because of boundary conditions.

3.2.2 Numerical models

The numerical simulations have been conducted with the commercial FEA software ANSYS® v11.0. Two types of numerical models have been implemented. On the one hand, a three-dimensional model (model A) which has been used to discriminate the mechanical properties that exert more influence on the calculation of the sensitivity factor K . On the other hand, once the mechanical properties to be analysed together with the geometrical variations have been determined, a parameterised axisymmetric model (B) has been implemented to obtain the variations of the indicators against variations of the input parameters. Model A has been implemented by fixing the mechanical parameters and geometrical properties, according to the manufactured samples (model C).

The numerical model used for the sensibility analysis (model A) is a 3D solid finite element model created from the extrusion of the transversal section. Bi-dimensional 4 node structural solid elements are used to generate the section mesh, and contains about 1000 elements (800 of which are contained in the sensor section

to increase the sensitivity). Element size is about 0.2 mm. Three-dimensional 8 node structural solid elements are used to extrude the depth of the specimen. The element length in the fibre direction is about 0.3 mm. Boundary conditions are applied to the top and the bottom of the grips' surface as follows: displacement through the fibre direction is imposed by 0.2% of the effective length of the specimen, which is the total length minus grips' length. Then, transverse displacements for the nodes at the centre axis of the FBG are restricted in order to avoid solid rigid motion. In this model, the mechanical properties and their statistical variations are used as input parameters. The input parameters are the Young modulus, Poisson ratio and torsion modulus of the host material, and the Young modulus of the coating (E_c). The output of this analysis is the strain state of the fibre and its statistical variations. A perfect bonding between all the interfaces is considered. Fig. 3.1 depicts a schematic of the geometry and mesh of this three-dimensional model used for the sensibility analysis.

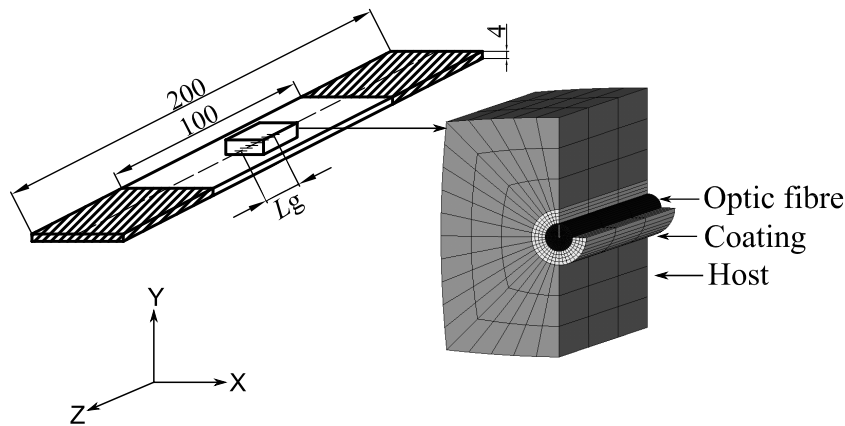


Figure 3.1: *Schematic geometry and mesh of the three dimensional CFRP specimen. L_g is the grating length set to 10 mm. Dimensions in mm.*

The second finite element model (B) is an axisymmetric representation of the problem. This symmetry option is chosen to reduce the computational cost as a large number of models, changing the geometry of the specimen, have to be computed. Bi-dimensional 4 node structural solid elements with axisymmetric behaviour are used to generate the section meshes. As in the three-dimensional case, the mesh is refined at the sensor zone. Fig. 3.2 depicts the scheme of the axisymmetric model.

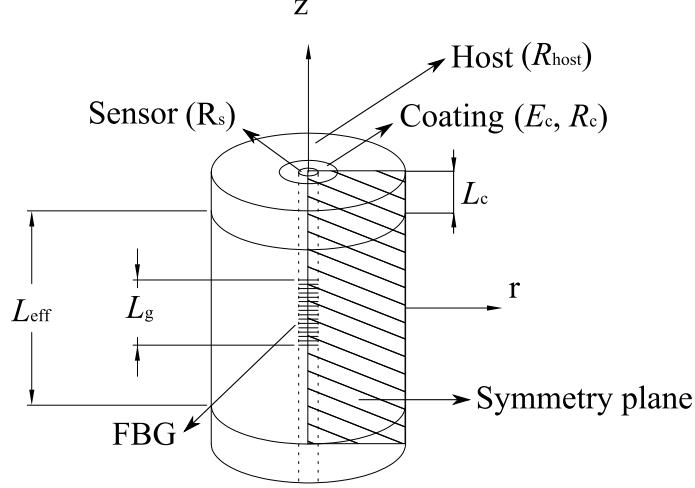


Figure 3.2: Schematic geometry of the axisymmetric numerical model. L_c is the constrained length, R_s is the sensor radius and L_g is the grating length set as 10 mm. As regards the variable parameters, R_c is the coating radius, R_{host} is the specimen thickness, L_{eff} is the effective length and E_c is the coating Young modulus. All values are reported in Table 3.1.

As regards to boundary conditions, all nodes belonging to $z = 0$ have the displacements restricted in both transverse directions to ensure that solid rigid motion is avoided. Then, nodes belonging at R_{host} position and at L_c are displaced $0.002 \cdot L_{\text{eff}}$ mm in order to apply a 0.2% longitudinal strain. L_g is the grating length (10 mm). The relation between the specimen's effective length and thickness, the aspect ratio (AR), is calculated as

$$AR = \frac{L_{\text{eff}} - L_g}{R_{\text{host}}} \quad (3.9)$$

The model was parameterised to analyse the variations of the indicators against the variations of input parameters. The input parameters and their interval of variation are shown in Table 3.1. As in the previous numerical model, a perfect bonding between the three interfaces is considered. In relation to the first indicator, the intrusion of the FBG on the host mechanical properties has to be evaluated by running the same model without an embedded FBG. It cannot be assumed that the imposed 0.2% longitudinal strain would be the longitudinal strain without the FBG since this 0.2% longitudinal strain is never reached when simulating an actual

specimen. This issue is due to the boundary conditions, because when the nodes of the grip surfaces are pulled, the longitudinal strain is transmitted by shear, and all the material below the pulled nodes is resistant to being strained.

Material	Parameter	Value/Interval of variation
Host (M21/T800)	Thickness (R_{host}) [mm]	[0.5,2.5]
	Effective length (L_{eff}) [mm]	[15,110]
Fibre optic	K^{free} [$10^{-7}/\mu\epsilon$]	7.966
	Radius (R_s) [mm]	0.0625
	Grating length (L_g) [mm]	10
Coating	E_c [GPa]	[0.16,16]
	Radius (R_c) [mm]	[0.125,0.25]

Table 3.1: *Mechanical and geometrical parameters. The effective length of both the fibre and the coating is the same as the host effective length. K^{free} is the sensibility factor for a free sensor.*

Finally, the three-dimensional unidirectional model (A) has been implemented to account for the properties of an actual manufactured sample. This model is known as model C and is performed with the same configuration, boundary conditions and mesh as that presented in Fig. 3.1. Perfect bonding between the interfaces is again considered. With this configuration the indicators as well as the response spectrum are determined. This spectrum is compared to the experimental value in order to validate the numerical results.

3.2.3 Transfer Matrix Method

For each numerical model the optical response spectra for both cases, when the specimen is both loaded and unloaded, is obtained. As the whole specimen model is implemented using a commercial FEA software, a finite element formulation is needed to calculate the optical response of the FBG [32]. To avoid performing the numerical integration of the coupled mode equations for the FBG, the T-matrix approximation is used, which is more computationally efficient. This method divides the grating into sections with uniform coupling properties along the grating length.

Thus, it is necessary to transform the 3D elements used in the specimen models into 2D elements for each cross-section in which the grating is divided (see Fig. 3.3). With this transformation done, and given any stress state in the sensor, the refraction index value is firstly calculated along with the principal optical axes, for each individual element in each cross-section in the optical fibre. This calculation is done using a strain-optic law [11, 32] as described in [73].

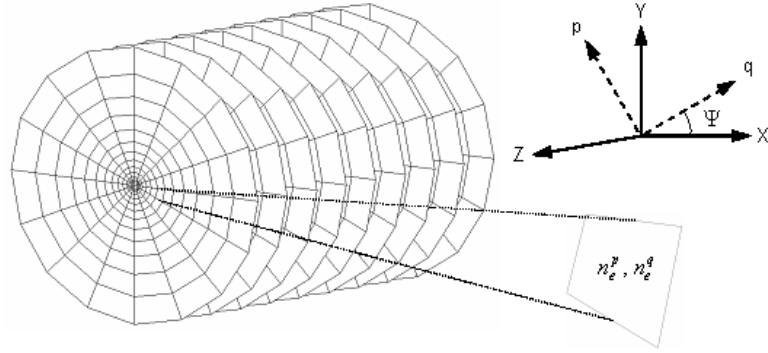


Figure 3.3: *Division of an optical fibre in cross-sections along the FBG length and discretisation using bi-dimensional elements. The polarisation axes for each element are p and q and the global coordinate axes are X - Y - Z .*

Once the refraction index for each element has been calculated on the principal optical axes in each element, the propagation constants for each Linearly Polarised Mode (LP) and the principal optical axes are calculated for each whole cross-section, which enables the calculation of the maximum and minimum effective index of refraction in each cross-section of the optical fibre. This calculation is done by solving the scalar wave equation of the optical fibre for each cross section, and by solving the global index ellipse equations in order to calculate the maximum and minimum propagation constant values [32].

The propagation constants in each cross-section and the strain applied to the sensor in the longitudinal axis of the grating are used as inputs for the T-matrix formulation. This formulation enables the transmission and reflection coefficients for a given wavelength to be calculated. When this calculation is performed along the bandwidth of the FBG, both the transmitted and reflected spectra are obtained.

3.2.4 Experimental set-up

The experimental data is obtained by using the results of a study on the influence of combined loads on the sensibility of embedded optical sensors. Tensile test specimens instrumented with both FBG sensors and strain gages are subjected to both tensile and compressive loads. The sensitivity factor is calculated by combining the optical response with the data of the strain gages placed on the samples and by considering that the internal axial strain is read the same at the top and bottom of the samples.

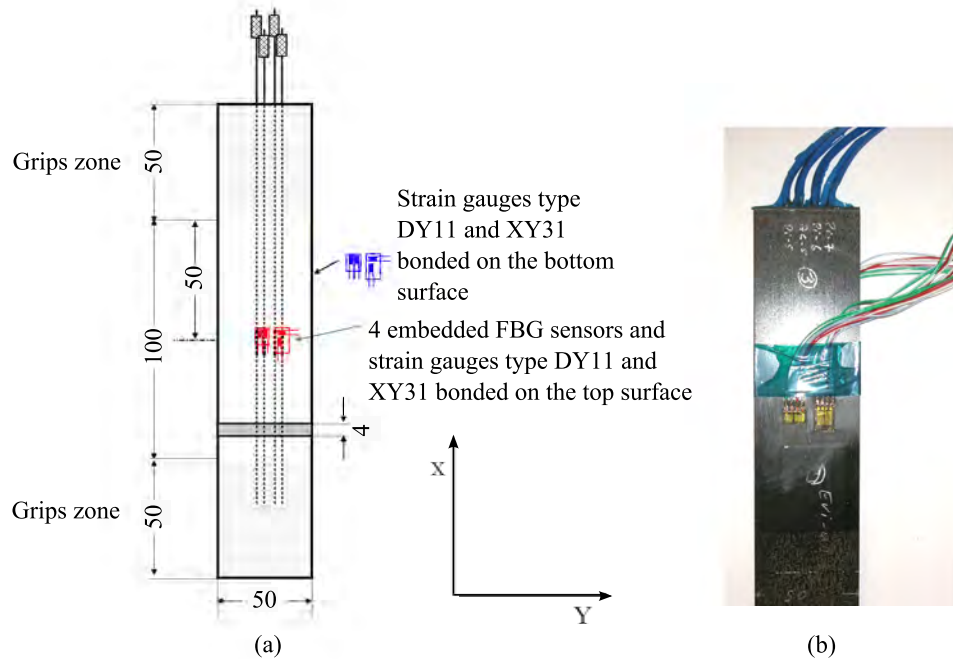


Figure 3.4: (a) *Experimental traction-compression unidirectional samples and (b) real image of an instrumented sample.*

The samples are manufactured from M21/T800 prepreps (properties in Table 3.2) in unidirectional lay-up (Fig. 3.4) with a stacking sequence $[0_{10}/OF/0_{10}]$ where OF is the optical fibre. The FBG sensors have been placed in the longitudinal mid-section in order to assess that they are measuring in a uniform strain zone. At both the front and the back sides of the specimen, two strain gages from HBM, Inc., have

been bonded. A bidirectional strain gage type XY31-3/120 (from here on known as type A) in Y direction, and a unidirectional strain gage type DY11-6/350 (from here on known as type B) in X direction. The gages have been bonded with the two components adhesive X-280 from HBM, Inc., and which were applied under constant mechanical pressure over 24 hours. The position of the strain gages coincides to the position of the 2 FBG sensors, which have been moved 7 mm from the centre longitudinal axis at both sides (see Fig. 3.4). The experimental equipment consists of a universal testing machine INSTRON 5584. The loads are measured by the load cell of the testing machine. Tensile and compressive tests are conducted in the strain range of $\pm 2000 \mu\epsilon$. The grips' speed is set to 1 mm/min throughout all the tests.

Material	Property	Value
Host (M21/T800)	E_{11} [GPa]	149 (*)
	E_{22} [GPa]	8.1 (**)
	G_{12} [GPa]	3.95 (**)
	ν_{12}	0.305 (*)
	ν_{23}	0.42 (**)
Fibre optic	ν_s	0.16
	E_s [GPa]	73.1
Coating	ν_c	0.4

Table 3.2: *Mechanical properties. The host is made by M21/T800 laminae lay-up. (*) corresponds to data tested by INTA. (**) corresponds to data tested by AMADE. Mechanical properties of fibre and coating are provided by FBG sensors' commercial suppliers.*

3.3 Results and Discussion

3.3.1 Sensibility Analysis (model A)

As previously mentioned, the first simulation (model A) is performed to study the influence of the mechanical properties on the strain transfer. The most relevant

result of the sensibility analysis carried out with numerical model A, is that the Young modulus of the coating is the only influential parameter on the strain state of the fibre. Nevertheless, it is found that the significance of this parameter on the results is only about 2.5%, whereas the influence of the rest of the mechanical parameters is even lower. Even though these variations are not significant, this means that any small variation due to mechanical properties on the strain state is because of the Young modulus of the coating.

3.3.2 Axisymmetric analysis (model B)

The axisymmetric analyses are carried out by using numerical model B, and geometrical parameters along with the Young modulus of the coating are considered. In these analyses the longitudinal strain distribution of both the host and the fibre are considered, as well as the *EPR* distribution through the grating, as outputs. These data are then used to calculate the indicators and find the most influent parameters.

Fig. 3.5 depicts the longitudinal strain distribution through the section (r) at $z = 0$ when $2000 \mu\epsilon$ are applied. It is shown that while for long specimens (i.e. 90 mm long), there is no variation between the sensor and the host longitudinal strain, for short specimens (i.e. up to 45 mm long) this difference increases until approximately $100 \mu\epsilon$, as in the case of $L_{\text{eff}} = 29\text{mm}$. In relation to the first formulation assumption, this is a key issue to study as the experimental calibration of the sensitivity factor K is carried out by measuring the longitudinal strain in the host with a strain gage on the surface. If the specimen is too short, K is not correctly evaluated, and consequently the measured strains in the interior of the host material will not be accurate.

Fig. 3.6 represents the distribution of *EPR* through half the grating of the sensor. It is shown that for large specimens the *EPR* remains constant through the grating and almost equal to the initial Poisson ratio ($\nu_s = 0.16$). However, for shorter specimens, not only does it not remain constant, but the *EPR* is also different to the Poisson ratio of the optical fibre.

The variations between the initial Poisson ratio and the *EPR*, the indicator pre-

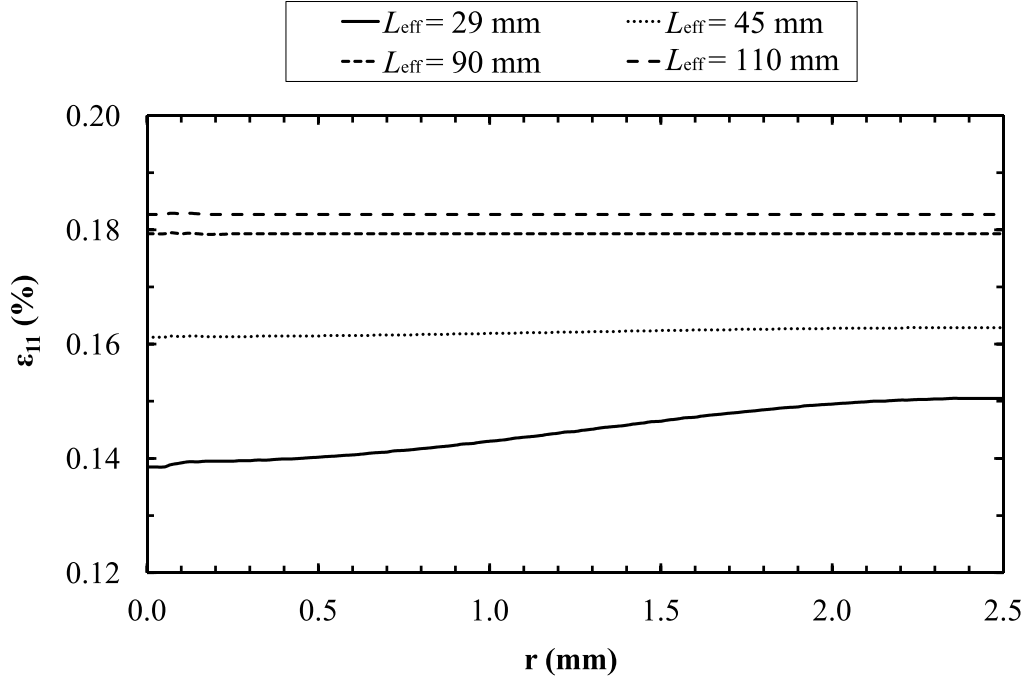


Figure 3.5: Longitudinal strain distribution through the section at $z=0$ for different effective lengths of the specimen and for $R_c = 0.125\text{mm}$, $R_{\text{host}} = 2.5\text{mm}$ and $E_c = 160\text{MPa}$.

viously defined as $EPR - PR$, are analysed in function of specimen length and thickness at the end of the grating. As depicted in Fig. 3.6, the higher variation between the EPR and the initial Poisson ratio is found at the end of the grating. Therefore, this indicator is analysed at this zone since it is the most critical, with z_0 taking the value of 5 mm. The $EPR - PR$ indicator is directly related to the second assumption, which presumes that there is no transverse strain coupled from the host to the fibre. Thus, a greater difference of the EPR to the initial Poisson ratio produces a higher coupling of transverse strain to the fibre. And, high variations of EPR through the grating produces higher inhomogeneities to the strain state.

Figs. 3.5 and 3.6 show that for a determined thickness, longer specimen lengths mean better agreement with the assumptions, which in turn means that the aspect ratio of the coupons (AR) is the most influential parameter for the formulation assumptions outcome. The $R_{\text{max}}^{\text{intr}}$ indicator accounts for the intrusion of the fibre on the host mechanical properties. By using two models (with and without the fibre) the maximum relative error between the host longitudinal strains is evaluated. Re-

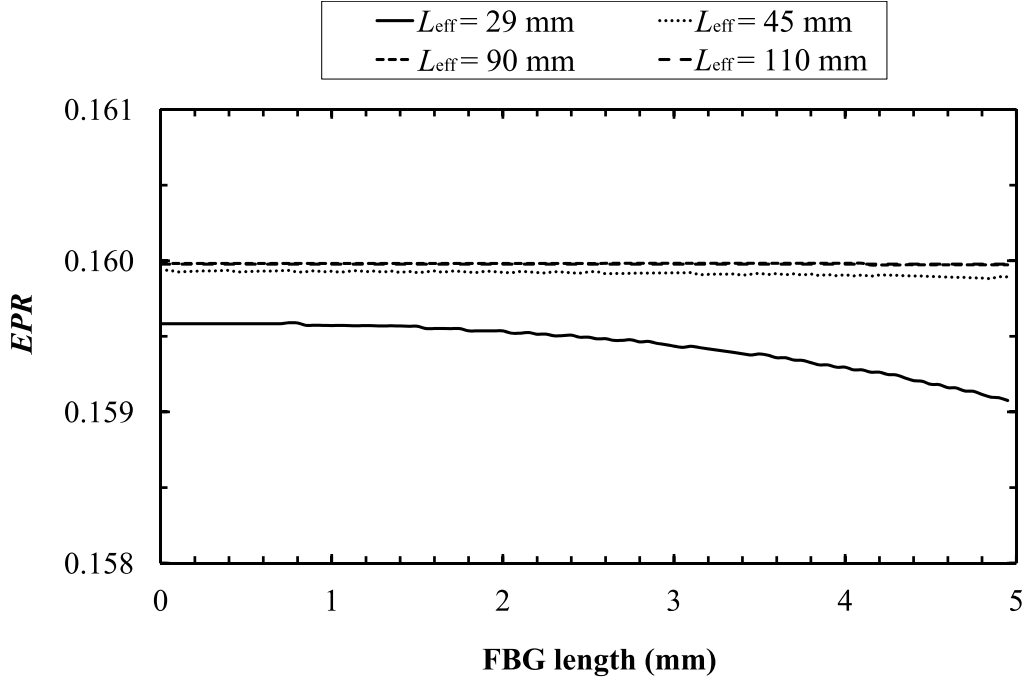


Figure 3.6: *Effective Poisson ratio distribution along the FBG length for different specimen effective lengths, for different effective lengths of the specimen and for $R_c = 0.125\text{mm}$, $R_{\text{host}} = 2.5\text{mm}$ and $E_c = 160\text{MPa}$.*

sults show that for every variation of the parameters, this error is always less than 0.6%. This means that for tensile test specimens the non-intrusion of the fibre is ensured in each of the studied cases.

The other two indicators are analysed against all parameter variations. When varying the coating radius and Young modulus, no variations of the indicators are found; i.e. the curves of R_{max} and $EPR-PR$ coincide exactly in each variation case. Hence, the only two parameters that directly affect the indicators are the specimen length and the thickness, or to be precise, the relation between them (AR).

According to [5, 13, 17], the use of an as high a compliant as possible interface between the sensor and the host material is recommended to avoid both non-homogeneous strain fields and transverse loads around the sensor. That is to say that transverse loads have to be countered due to their effects in the peak splitting phenomenon. Nevertheless, the present study has found that for specimens under

longitudinal loading, the Young modulus of the coating has no effect on the indicators' variations, nor on the precision of the sensor measurements. This kind of specimen, in which the longitudinal strain of the sensor is transmitted by shear, needs enough distance for the strain to be completely transmitted but the nature of the coating does not affect that distance. As discussed in [5], the effect of the coating is focused on the transverse strains, which are softened and finally avoid the peak splitting phenomenon due to birefringence, of which is not discussed in the present work.

Fig. 3.7 depicts the distribution of the R_{\max} indicator as a function of the logarithm of the aspect ratio. Note that, for any thickness value when the $\log(AR)$ reaches approximately 1, which in turn means an AR of approximately 9, the R_{\max} is approximately 0.1, which corresponds to a difference of 10% between the fibre and the host longitudinal strains.

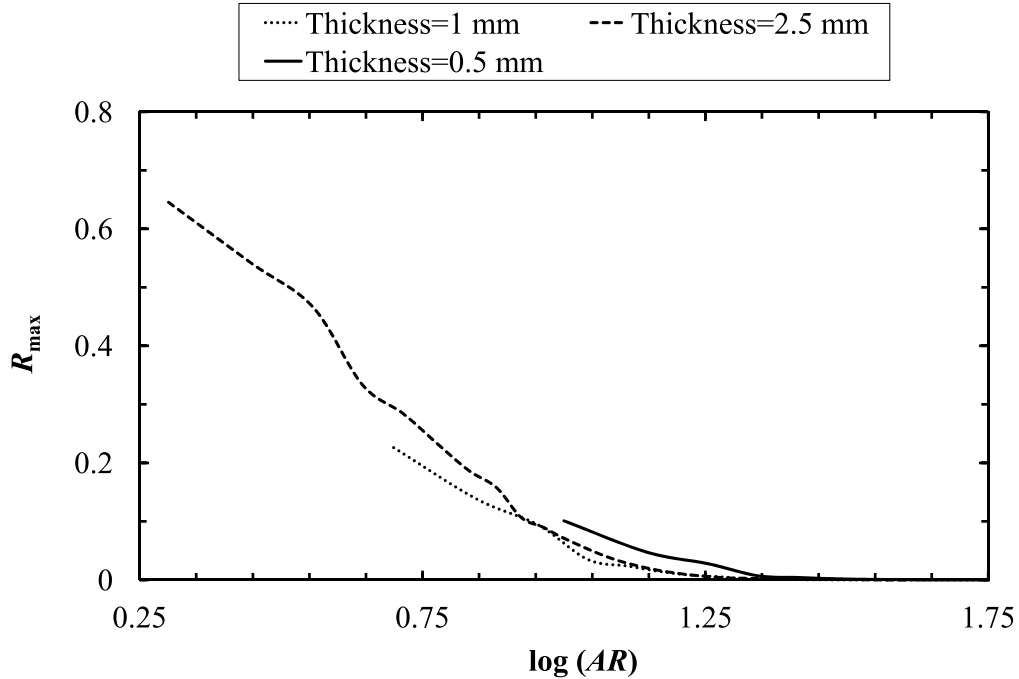


Figure 3.7: Distribution of the R_{\max} indicator against the AR for different specimen's thickness and for $R_c=0.125$ mm and $E_c=160$ MPa.

Therefore, the R_{\max} indicator appears to be a good evaluator of the first assump-

tion outcome. The closer to zero the indicator is, the closer the longitudinal strains of the host and the fibre are.

Fig. 3.8 depicts the variations between the EPR and the initial Poisson ratio. It can be seen, as when calculating the R_{\max} , that when the $\log(AR)$ reaches a value of approximately 1, which means an AR of approximately 9, the value of the $EPR - PR$ indicator reaches a value of approximately 1. If this value is assessed along the whole grating, ν^* remains constant, and no spectrum distortion is observed.

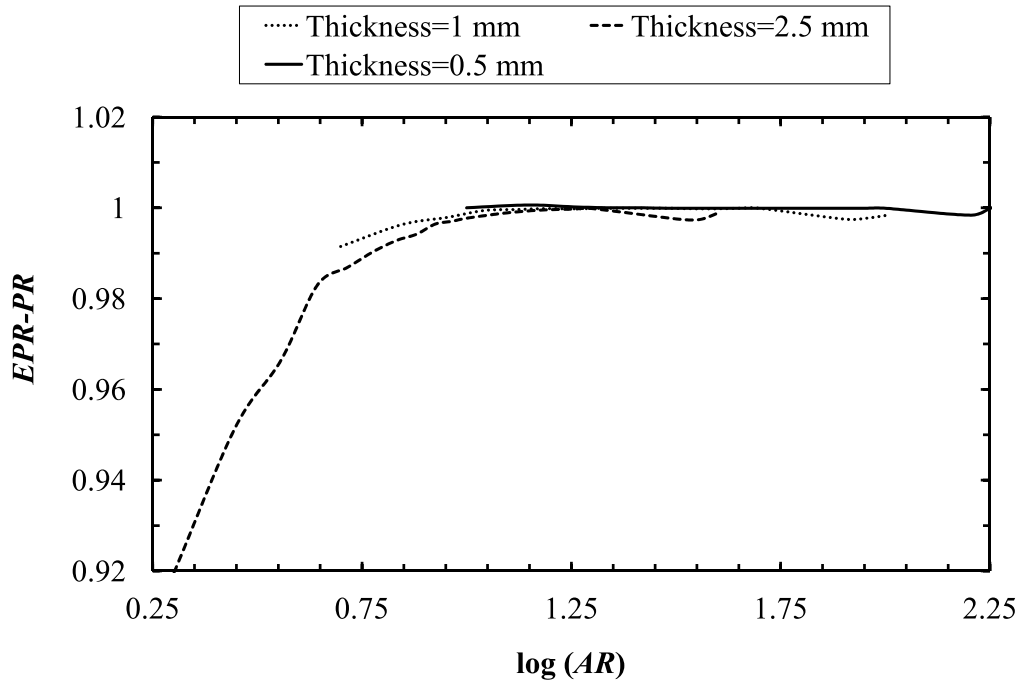


Figure 3.8: *Distribution of the $EPR - PR$ indicator against the AR for different specimen's thickness and for $R_c=0.125$ mm and $E_c=160$ MPa.*

In relation to the R_{\max} indicator, when $AR = 9$, the difference between host and sensor axial strains is about 10%. This difference is too high for considering the first formulation assumption outcome, since the calibration of the sensor for internal strain measurements is not accurate and finally the measurements are not precise. Meanwhile, with regards to the $EPR - PR$ indicator, for the same AR , there is no significant transverse strain coupled from the host to the fibre. Figs. 3.7 and 3.8 demonstrate that the aspect ratio of the coupon is the most influential parameter for

obtaining measurements in agreement with the formulation assumptions for coupons under uniform strain states. This means that the homogeneity of the strain field at the grating zone is assured if the specimen has enough material to transmit the longitudinal strain by shear.

The optical response spectrum is numerically computed for four different aspect ratio coupons. This is calculated by using the T-matrix formulation (detailed in Section 3.2.3) in combination with an optical finite-element approach for a previous calculation of the effective indexes of refraction. Each specimen gives a different spectrum, and it shows that there is a direct relation between the indicator values and the response spectrum. A summary of the results can be seen in Table 3.3.

Item	B-1	B-2	B-3	B-4	C
L_{eff} [mm]	15	29	45	100	100
AR	2	7.6	14.0	36.0	22.5
R_{max}	0.40	0.08	0.01	0.00	0.00
$EPR - PR$	0.924	0.994	0.998	0.999	0.998
EPR	0.147	0.159	0.160	0.160	0.160
$\Delta\lambda$ [nm]	0.975	1.696	1.975	2.275	2.165
λ_0 [nm]	1549.9	1549.9	1549.9	1549.9	1550.0
ε_1^h [$\mu\varepsilon$]	1368	1505	1629	1811	1742
ε_1^f [$\mu\varepsilon$]	822	1385	1612	1811	1742
K_{OPT} [$10^{-7}/\mu\varepsilon$]	7.653	7.901	7.905	8.105	8.018
K_{AN} [$10^{-7}/\mu\varepsilon$]	7.917	7.963	7.965	7.965	7.965

Table 3.3: Results of the B and C numerical models. For all B models, $R_{\text{host}}=2.5$ mm, $E_c=0.16\text{GPa}$ and $R_c=0.125$ mm. The sensitivity factor K for each specimen is calculated by simulating an actual calibration that is obtained by dividing the optical response over the host longitudinal strain (K_{OPT}). K_{AN} is the sensitivity factor calculated by means of analytical formulation.

Fig. 3.9 depicts the response spectrum for different specimen lengths with the

same thickness, which in turn means different aspect ratio coupons, when they are unloaded and longitudinally 0.2% strained. Note that all have the same initial reflected wavelength, while with the load applied, the responses differ due to their differing aspect ratios. The models are identified as B-1, B-2, B-3 and B-4.

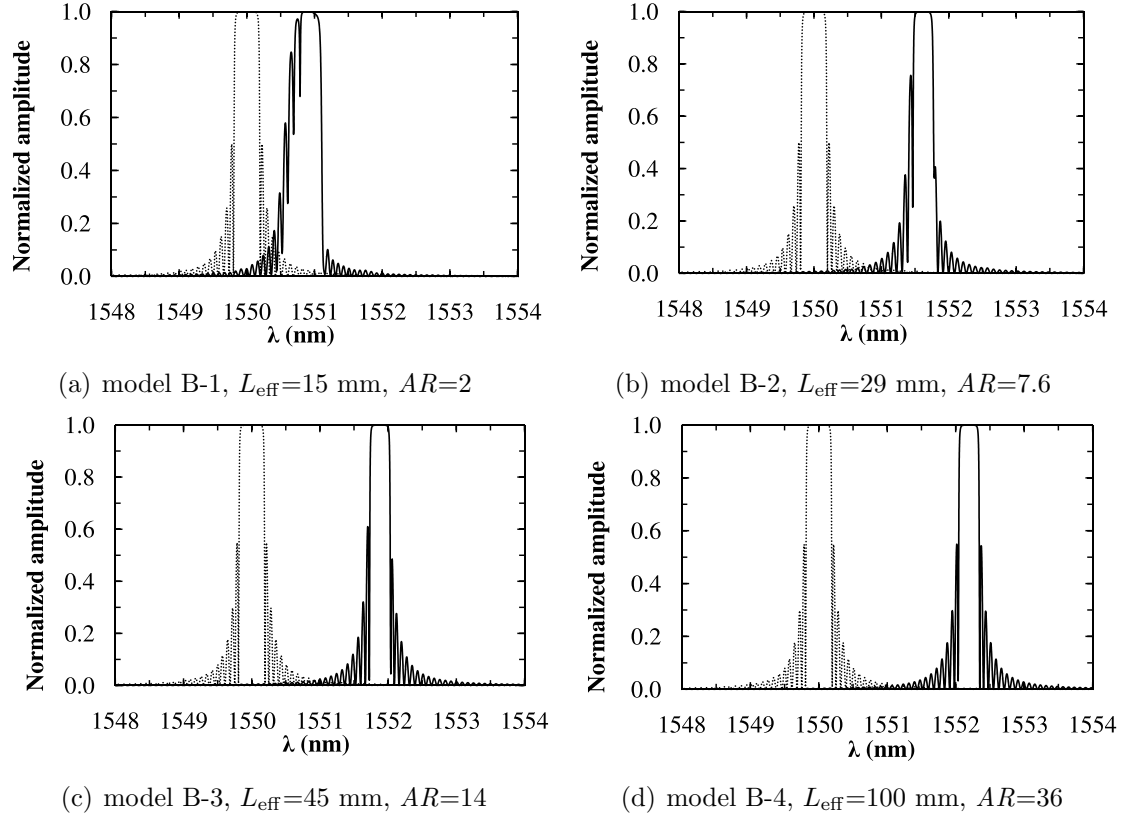


Figure 3.9: Reflected spectrum for the unstressed (dashed line) and 0.2% longitudinally strained (continuous line) axisymmetric model. Parameters of the model are $R_{\text{host}}=2.5$ mm, $R_c = 0.125$ mm and $E_c = 160$ MPa.

The spectrum calculated by means of model B-1, shown in Fig. 3.9(a), corresponds to the specimen with the lowest AR ($AR = 2$). The geometric properties of this coupon in relation to the grating length give a distorted spectrum because the strain is not fully transferred from the host to the FBG length. Hence, having the same load conditions as other numerical models, the strain read by the FBG is not faithful to the actual internal strain state. It should be noted that when analyzing the values of the indicators for this model, the value of the indicator $EPR - PR$

and the *EPR* distribution for short specimens, depicted in Fig. 3.6, the reflected spectrum is expected to be distorted even when the applied strain is homogeneous. Having a non-constant *EPR* distribution is solved by considering the maximum peak as the characteristic wavelength when calibrating K . Nevertheless, the calibration of this coupon in relation to internal strain measurements is not accurate (as R_{\max} indicator presumes) since the calibrated sensor gives an internal longitudinal strain measurement of $1368 \mu\epsilon$, while the longitudinal strain state in the sensor is $822 \mu\epsilon$. The difference of about $500 \mu\epsilon$, is not within the range of acceptability.

Fig. 3.9(b) depicts the reflected spectrum for the model B-2 (0.2% strained specimen). Due to the *AR* value and its corresponding R_{\max} and *EPR* – *PR* values, the reflected spectrum is expected to be just a little distorted, but less so than the previous one. Nevertheless, the calibration of this coupon in relation to internal strain measurements is not accurate due to the R_{\max} indicator value. The calibrated sensor gives an internal longitudinal strain measurement of $1505 \mu\epsilon$, while the longitudinal strain state in the sensor is $1385 \mu\epsilon$, as shown in Table 3.3.

The reflected spectrum of model B-3 is shown in Fig. 3.9(c). As the indicators predict a good agreement with the formulation assumptions, the reflected spectrum is expected to have shifted from the origin. Thus, an elastic response is expected for an elastic load step. Nevertheless, as depicted in Fig. 3.5, longitudinal strain in the grating and in the host are $1612 \mu\epsilon$ and $1629 \mu\epsilon$, respectively. As in the B-2 model case, there is almost no strain coupled from the host, but the evaluation of K is not perfectly accurate. Note that in this case the relative error between longitudinal strains is 1.05%, which makes the strain measurement precise enough.

Fig. 3.9(d) depicts the response spectrum for the model B-4. According to the R_{\max} and *EPR* – *PR* values, the response spectrum is expected to have perfectly shifted and the FBG to be correctly calibrated. In this case the sensibility factor K can be correctly calibrated since a single longitudinal strain for the whole specimen is found, as depicted in Fig. 3.5, and the longitudinal strain is $1811 \mu\epsilon$ in all zones. Hence, the internal strain measurement corresponds faithfully to the actual internal strain state.

3.3.3 Experimental results

For the 0.2% tensile loaded specimens, the shift of the reflected wavelength is determined. Assuming the axial strain in the optical fibre is the same as that read by the longitudinal strain gage, the sensibility factor is calculated. Experimental results used for calculations are presented in Table 3.4. The mean value for all the unidirectional samples is $K=8.08 \Delta 10^{-7}/\mu\varepsilon$. This value is used to validate the numerical calculations of the sensibility factor by means of model C. After the parameters of the experimental tensile tests specimens are validated, and the indicators are found to be in the range for a reliable strain measurement, those specimens are simulated and K is numerically computed.

Item	Value
R_{\max}	0.00
$EPR - PR$	0.998
EPR	0.160
λ_0 [nm]	1549.965
$\Delta\lambda$ [nm]	2.129
$\varepsilon_1^{\text{host}}$ [$\mu\varepsilon$]	1700
K [$10^{-7}/\mu\varepsilon$]	8.08

Table 3.4: Results of the tensile test specimens with $L_{\text{eff}}=100$ mm and $AR=22.5$. The sensitivity factor K is calculated by dividing the optical response by the measured gage strain.

3.3.4 Three-dimensional analysis (model C)

The numerical model C is calculated and analysed to obtain the values of the indicators. As the non intrusion is assessed for every case, and it is experimentally checked, this part only shows the value of the $EPR - PR$ and the R_{\max} indicators. For the conditions under which the specimen is designed and tested, R_{\max} found in the specimen is approximately zero and $EPR - PR$ is approximately one, as presented in Table 3.3. Then, the response spectrum when strained at 0.2% is expected

to have perfectly shifted since there is neither transverse coupled strain nor does the *EPR* present variations, and its calibration is accurate for internal measurements. The response spectrum for both the unloaded and longitudinally 0.2% tensile loaded specimen, along with the comparison with the experimental result, are presented in Fig. 3.10.

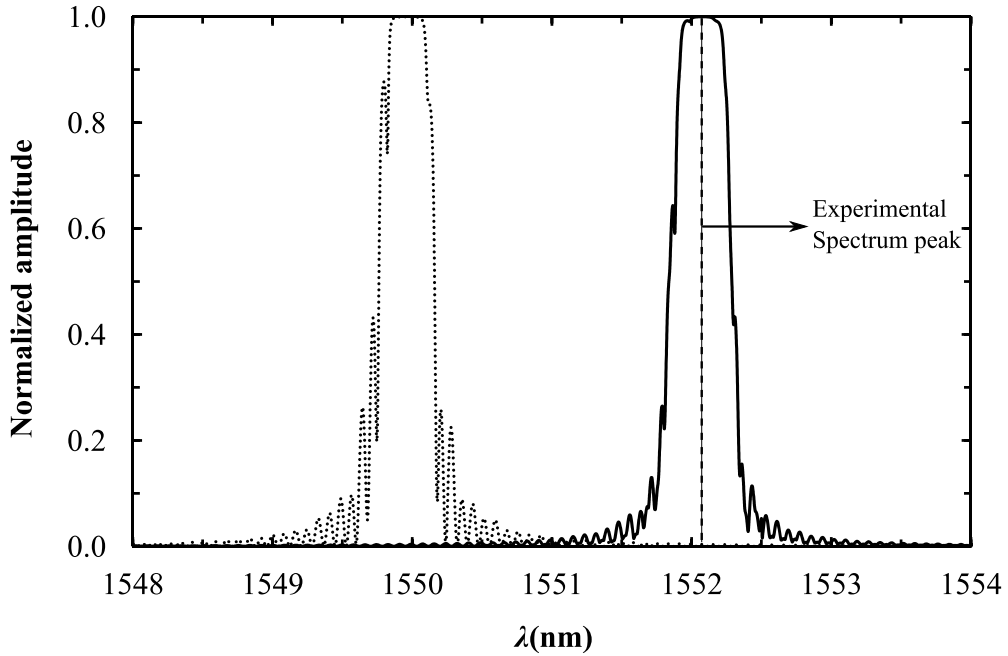


Figure 3.10: *Reflected spectra of the three-dimensional specimen when unstrained and 0.2% longitudinally loaded. This model has an effective length of 100 mm and a thickness of 4 mm.*

In this case the longitudinal strain, both at the fibre and at the host, is $1742 \mu\epsilon$. Then, the sensibility factor is calculable and presented in Table 3.3 as model C. Note that the numerical results show, for the analytical formulation of K , presented in Eq. (3.2), and the optically calculated K , calculable following Eq. (3.1), a relative error of only 0.66%. The value of the optically calculated sensibility factor $K=8.018 \Delta 10^{-7}/\mu\epsilon$ is reasonably close to the experimental value for these unidirectional specimens found as $K=8.08 \Delta 10^{-7}/\mu\epsilon$. Their relative error is only 0.77%.

3.4 Conclusions

A methodology to analyse the precision of the response spectra of FBG sensors for laboratory specimens under longitudinal loading is defined. All the numerical models are implemented within the aforementioned parameters. The influence of each parameter is analysed through the values of the indicators R_{\max} , R_{\max}^{intr} and $EPR - PR$. Finally, the optical response spectrum is obtained by calculating the effective index of refraction values for the finite element model of the FBG sensor and by using the T-matrix method.

The results obtained from the finite element sensibility analysis show that, for tensile test specimens, the influence of the material mechanical properties, such as the Young modulus of the coating, on the precision of the sensor measurements is not relevant.

The axisymmetric finite element analysis results demonstrate that the most influential parameter on the FBG strain state for longitudinally tensile loaded specimens is the aspect ratio of the coupon. For the materials and specimen configuration studied, the limit of applicability lies in the elastic range of the tests, where uniform strains are expected, and on the aspect ratio which has been found to be about 9. This AR value give an R_{\max} of 0.1 and an $EPR - PR$ of 1. The axisymmetric models with these indicators give distorted response spectra and an imprecise calibration of the sensitivity factor. Hence, when $EPR - PR$ tends to one and R_{\max} tends to zero, the calibration of the sensor and the precision of its measurements are assured. It has been demonstrated that $EPR - PR$ has a direct relationship to the response spectrum profile, while R_{\max} has a direct relationship to the correctness of the calibration for internal strain measurements.

The parameters of the three dimensional numerical model are within the expected range of a precise spectral response. Numerical results show good agreement with the experimental results.

It is also demonstrated that when the transverse loads compared to longitudinal

loads are not relevant, as in the case of specimens under longitudinal loading, the coating geometry and compliance have no effect on the precision of the measurements since there is no birefringence phenomenon to be accounted for. In other words, the use of a coating can be avoided in such cases in order to obtain higher sensibility in the FBG without losing any reliability of the measurement even though the optical fibre becomes more fragile.

It is important to note that the present study, in order to guarantee that the strain sensor provides a precise measurement of the internal strain state, has defined an AR of approximately 9 to ensure that there is no transverse strain coupled to the fibre ($EPR - PR$ indicator) and there is an AR of approximately 14 to ensure a maximum relative error between internal and external longitudinal strains of 1% (R_{\max} indicator).

Chapter 4

Crack tip identification with long FBG sensors in mixed-mode delamination

4.1 Introduction

The initiation of a crack within a composite structure and its propagation can lead to structural collapse, therefore it is essential to identify and characterise a crack inside a composite structure. Mixed-mode delamination is of high interest because when delamination occurs in an actual structure, it is not usually subjected to pure Mode I or Mode II loading, but rather to a combination of both [74, 75]. The standard ASTM D6671 Mixed-Mode Bending (MMB) test [1, 76–78], among others [79], to study the interaction of the two modes in fibre reinforced polymer composites, is therefore of high interest. The MMB test [1] allows for the characterisation of both initiation and delamination growth for a wide range of mixed-mode I/II ratios. Namely, ratios of G_{II}/G_C from 16% to 100%, where G_{II} is the active fracture energy in mode II and G_C is the total fracture energy, can be achieved.

When using FBG sensors in composite delamination samples, the strain field surrounding the FBG has to be considered. Since in such samples a stress concentration (i.e, delamination) is near the fibre sensor, the strain along the FBG is not uniform and large strain gradients are encountered along it. Recent work has

demonstrated that strain measurements near the delamination are feasible by using multiplexed short FBG sensors [8]. Such sensors, due to their small length, will often be subjected to strain considered as homogeneous, and in turn the relationship between the spectral sensor responses and the strain is given by a simple equation (i.e. independent of the axial distance z in Eq. (5.6)). Data from multiplexed short FBG sensors can be used to construct quasi-continuous strain profiles along the sensor. Meanwhile, [7, 24, 25] demonstrated that the disturbance of the optical fibre to the ERR is minimal and very local and a direct determination of the strain field with long FBG sensors is possible through the Optical Low Coherence Reflectometry (OLCR) interrogation technique of the sensor. The principal positive aspects in this method are the precision of the measurements, and the length of the FBG that enables a large sensing zone even for complex strain states. However, this technique obliges the strain measurement to be time independent. In other words, the strain measurement has to be static, which in turn makes it impossible to use this interrogation technique in real time monitoring in fatigue tests, for instance.

In this chapter, results of the crack tip location in MMB specimens with long FBGs are presented. Seven carbon/epoxy unidirectional samples, some of them with an embedded long FBG sensor, were subjected to mode mixtures G_{II}/G_C from 22% to 75%. In addition, numerical simulations reproducing the test were performed. The crack tip location was verified through a visual inspection using high definition photographs as well as from strain measurements from the embedded long FBGs.

4.2 Methods and Materials

4.2.1 Materials and samples description

The carbon/epoxy unidirectional samples were manufactured by stacking 16 layers of AS4/8552 unidirectional prepreps with stacking sequence of $[0_8/t/0_8]$, where t indicates the delamination plane. The mechanical properties of this material are shown in Table 4.1.

To follow the crack tip with the FBG sensor, a crack propagation of 35 mm was

E_{11} [GPa]	E_{22} [GPa]	ν_{12}	ν_{23} (estimated)	G_{12} [GPa]	G_{IC} [$\frac{J}{m^2}$]	G_{IIC} [$\frac{J}{m^2}$]
135	8.8	0.354	0.4	4.6	267	1028.64

Table 4.1: *AS4/8552 elastic and fracture mechanical properties. G_{IC} and G_{IIC} are taken from [80] and [81] respectively.*

desired, and an initial crack length had to be 25 mm according to the standard. Thus, the effective dimensions of the samples for testing were 120x25 mm with a nominal thickness of 2 mm, and the FBG was placed within these at 35 mm. All the samples were pre-cracked for a few millimetres by using the Side Clamped Beam (SCB) hinge system presented in [80]. Then, the crack tip was localised in each sample by wedging and by means of an optical microscope. Once the crack tip was marked in all samples, the loading blocks, whose dimensions are 10x10x25 mm, were glued 25 mm behind the crack tip to ensure the desired initial crack length. A schematic of the coupons ready for testing is shown in Fig. 5.1. A Teflon film with a thickness of 20 μm was placed between layers 8 and 9 to introduce an initial crack surface. In the specimens where an FBG sensor was embedded, the optical fibre was placed one layer above the crack surface, between layers 9 and 10, and aligned with the reinforcing fibres. The FBGs were 8 mm long and they were longitudinally placed at about 83 mm from the sample end so that an initial crack growth performed in pure mode I could be obtained without entering the sensing zone. The FBGs were written on single mode fibre (SM28) with a diameter of 125 μm and the coating was removed over the grating length plus a few mm on both its ends. The reference Bragg wavelength to measure local strains was taken at room temperature with the embedded FBGs and it was about 1300 nm for all of them.

4.2.2 Mechanical testing

Seven coupons were tested in nine different tests. Some of them were without optical fibres in order to examine the influence of the optical fibre on the specimens' mechanical response, except in the case of 50% mode mixture which was only checked through a numerical simulation. First, all samples were pre-cracked in pure mode

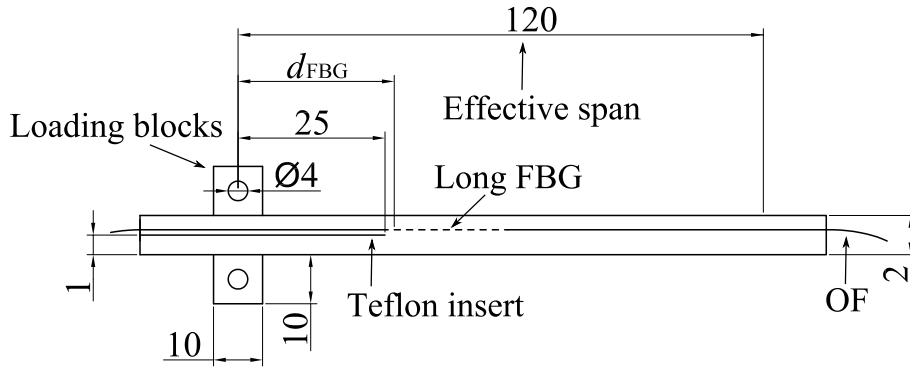


Figure 4.1: Schematic of the experimental samples' configuration (units in mm). d_{FBG} is the distance from the load application point to the beginning of the FBG.

In order to avoid the Teflon insert effect. Then, the MMB tests were conducted following the ASTM D6671 standard procedure [1] with controlled displacement. Fig. 4.2 depicts a schematic of the MMB testing set-up. Nine experiments were carried out under five different mode mixtures with details as described in Table 4.2.

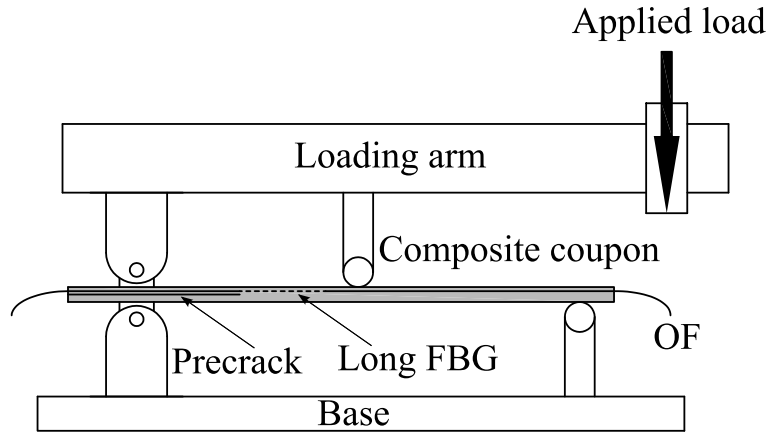


Figure 4.2: Mixed-Mode Bending rig scheme.

The cross-head of the custom-built servo electric test machine (Walter + Bai ag, type EC80-MS[®]) was displaced at a rate of 3 mm/min and the load was recorded with a 1 kN load cell. As the pre-cracks had been performed in pure mode I, the initial jump due to resin rich zone was avoided. In the samples containing an embedded FBG, the tests were interrupted at a certain crack length during the propagation stage to allow for the optical measurements. After the tests were stopped for 30 minutes, and the system was perfectly stable (i.e. no further load decreasing was

Test code	Mode Mixture (%)	embedded FBG	d_{FBG} [mm]
T22I	22	YES	39.9
T22NI	22	NO	[-]
T25I	25	YES	37.9
T25NI	25	NO	[-]
T30I	30	YES	38.7
T30NI	30	NO	[-]
T50I	50	YES	37.7
T75I	75	YES	39.9
T75NI	75	NO	[-]

Table 4.2: *Testing codes configuration. I and NI signs are instrumented and non-instrumented samples respectively. d_{FBG} is the distance from the application point of the load to the beginning of the FBG. For T22I, T22NI and T75I and T75NI, the samples were the same but tested at different crack lengths.*

detected), the optical measurement with the OLCR technique [24, 25] started. Each optical measurement took about half an hour in duration. When the tests were finished, the fracture toughness, with the recorded value of the load, was calculated by the methodology described in [1]. At first, the crack length was observed on one specimen side by means of an optical system. The samples were previously prepared by painting in white the lateral side with marks spaced one millimetre apart. The marks allowed the propagation data to be taken at every millimetre of crack increment. A detail of the lateral view of the sample during the MMB test is depicted in Fig. 4.3.

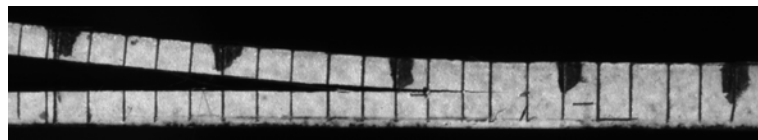


Figure 4.3: *Detail of the lateral view of a sample with marks for propagation data acquisition.*

After the pre-cracking stage, the initial crack tip position was determined. In the

samples containing an FBG sensor, the FBGs were placed at 14 mm ahead of the initial crack tip to ensure a slow propagation of the crack into the sensing zone. An iterative process accounting for the rig weight compensation was performed following the ASTM standard equations. First of all, an estimated critical load was calculated as

$$P_c^{\text{est}} = \sqrt{\frac{\frac{4}{3}G_c^{\text{est}}b^2E_{11}h^3L^2}{(3c-L)^2(a_0+h\chi)^2 + \frac{3}{4}(c+L)^2(a_0+0.42h\chi)^2}} \quad (4.1)$$

where b and h are the specimen width and half thickness respectively, E_{11} is the Young modulus in the fibre direction, L is the half span length of the set MMB apparatus, a_0 is the initial crack length, χ is the crack length correction parameter according to the standard [1] and G_c^{est} is the estimated value of the total fracture toughness computed as

$$G_c^{\text{est}} = G_{\text{IC}} + (G_{\text{IIC}} - G_{\text{IC}})B^\eta \quad (4.2)$$

where G_{IC} and G_{IIC} are the critical fracture energies in pure mode I and mode II, respectively; B is the mode mixture, η the interaction parameter between modes, and c is initial lever arm distance computed as

$$c = \frac{12\beta^2 + 3\gamma + 8\beta\sqrt{3\gamma}}{36\beta^2 - 3\gamma}L \quad (4.3)$$

where

$$\gamma = \frac{1-B}{B} \quad (4.4)$$

$$\beta = \frac{a_0 + h\chi}{a_0 + 0.42h\chi} \quad (4.5)$$

Once c was computed, the lever length was adjusted in the rig, and the distance of the centre of gravity was experimentally measured (c_g). Therefore, accounting for the estimated critical load, and the weight of the rig, c was computed again as

$$c = \left(1 + \frac{P_g}{P_c^{\text{est}}}\right) \frac{12\beta^2 + 3\gamma + 8\beta\sqrt{3\gamma}}{36\beta^2 - 3\gamma}L - \frac{P_g}{P_c^{\text{est}}}c_g \quad (4.6)$$

where P_g is the weight of the rig. As the critical load depended on the lever distance, and at the same time the lever distance depended on the critical load, the solution

process was iterative. Once the value of c converged, the lever distance was set and c_g was again experimentally determined. By means of these analytical procedures, the stability of the crack growth for each mode was analysed.

In the 50% and 75% mixed-mode tests, the analytical load-displacement curves indicated that the initial propagation phase of the crack was unstable for 25 mm long initial cracks. By using the described equations it was observed that, by increasing the initial crack length for these modes a stable propagation was obtained. Fig. 4.4 depicts the analytical load as a function of displacement for a sample with 50% mode mixture and for two different initial crack lengths. Note that while for the larger crack the curve has a smooth initiation phase of the propagation zone, for the shorter crack the initiation of the propagation shows a snapback indicating that the crack growth is unstable (i.e. the crack could overcome the sensing zone).

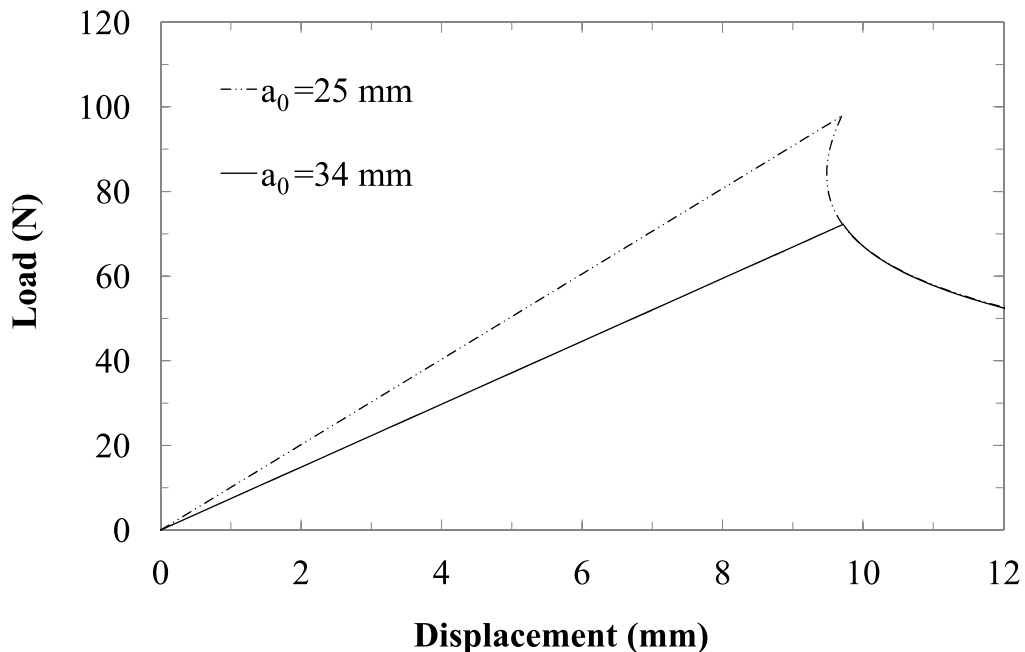


Figure 4.4: Analytical stable and unstable propagations for 50% mode mixture and two different initial crack lengths. Note that both the stable and the unstable cases propagate at the same fracture energy.

To avoid unstable propagation for the tests with 50% and 75% mode mixtures,

an initial propagation with 22% of mode II was performed until the assessment of a stable crack growth for high mixed-modes. The desired crack lengths for 50% and 75% mode mixtures were 34 mm and 40 mm, respectively. This process was applied to the tests T22I, T75I, T22NI, T75NI and T50I (Table 4.2).

4.2.3 Strain measurements

The axial strain (fibre direction) around the crack tip was measured by an optical fibre that contained a long FBG. An FBG sensor basically consists of a periodic change of the refractive index in the core of the glass fibre which has been written by means of a UV laser. The changes in strains of the FBG are directly related to the changes of the reflected wavelength and when the strain field is not uniform the local wavelength depends on the position in the FBG. In such cases, in order to determine the local wavelength along the FBG, a method based on the OLCR technique and the layer peeling algorithm was used as in [7, 24, 25]. In the case considered in this work, as the length of the FBG is long enough to be subjected to a non uniform strain field, the relation between the local wavelength and the local axial strain along the axis z , is

$$\frac{\Delta\lambda_B(z)}{\lambda_{B_0}} = (1 - p_e)\varepsilon_z(z) \quad (4.7)$$

where λ_{B_0} is the local wavelength of the unstrained sensor, $\Delta\lambda_B(z)$ is the shift of the local wavelength, and p_e is the opto-mechanical coefficient which takes the value of approximately 0.22 [82]. Note that this is a simplified form supposing no out-of-axis strain other than those created by Poisson's coefficient.

4.2.4 Crack tip identifications

The crack tip identification method consists of axial strain measurement by means of long FBG together with the OLCR technique. The identifications of the crack tips were carried out by first identifying the axial strain profile along the FBG. According to [7], the axial strain profile in a delaminated sample in pure mode I presents a bump indicating the crack tip position. But when loading under mixed-mode ratios, the decrease of the axial strain is steep (i.e. no bump is observed). Thus the crack tip is located within approximately 1.5 mm from the highest strain

value to the lowest strain value. As the maximum strain gradient is always located in the vicinity of a crack tip, the derivative of the axial strain profile is calculated to find the exact position of this maximum strain gradient which in turn is the position of the crack tip. The experimental results were then compared with numerical simulations confirming the crack tip position.

This method was verified with the sample T30I by observing the actual crack front position in the fractured surface after the test where the difference in contrast due to mode change allowed the crack front to be easily identified. The test was definitively interrupted at a certain crack length allowing for the comparison between the optical measurement, the visual inspection, by means of lateral marks, and the visual surface inspection after the two arms were split.

4.2.5 Numerical simulations

In order to avoid a large number of tests for determining the crack tip position, a number of simulations were performed. As the interest was focused on the crack tip location but not on the exact axial strain value, in this work the samples were modelled without considering the fibre. The presence of fibre bridging in the vicinity of the crack tip is not taken into account as this does not affect the crack front position. Nevertheless, this does lead to an insignificant overestimation of both the load and the axial strain profile when the crack propagates. Simulations were performed with the commercial software ABAQUS[®] v6.9.1, and the crack growth was simulated by means of cohesive elements developed by Turon *et al.* [83].

For the simulations of the experiments, the geometry of the actual samples was simplified by assuming plain strain behaviour and thus performed with 2D simulation. Four node plane elements (CPE4) were used to simulate the arms with an element size of about 0.125 mm. At the zone where the FBG was located, the mesh was refined in both the fibre and the thickness directions. The element size in the fibre direction was 0.0625 mm. The line of nodes simulating the centre of the optical fibre was separated by three elements so that the strain gradients were well captured. This element size was 0.022 mm. In order to know exactly where the FBG was placed in the thickness direction, micrographs were obtained from the

actual specimens.

A schematic of the numerical model is shown in Fig. 4.5. In relation to boundary conditions, node base 1 was restricted in the 2 direction, while node base 2 was restricted in 1-2 directions. The displacement was imposed to the reference node (RN in Fig. 4.5) which is coupled to the top and top-mid nodes, as they belong to the rig, through the lever law equation

$$\left(\frac{c}{L}\right) u_2^{\text{top}} - \left(\frac{c+L}{L}\right) u_2^{\text{top-mid}} + u_2^{\text{RN}} = 0 \quad (4.8)$$

The load was applied in three steps. The first step considered the weight of the rig. The second applied a displacement to the reference node with large increments as no delamination was expected. The third and final step applied a displacement to the reference node with very short increments to obtain a clear capture of the delamination onset and propagation.

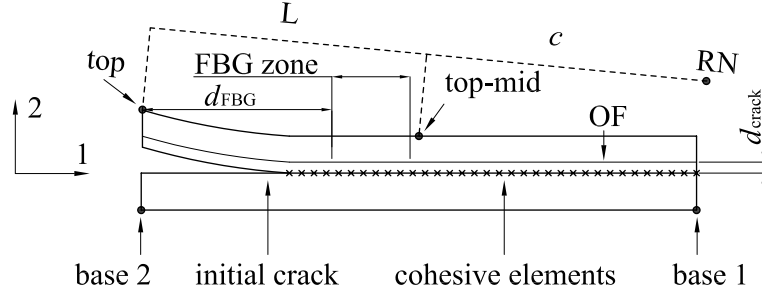


Figure 4.5: *FE model used in the simulation of different MMB tests. L is half of the span of the sample, RN is the reference node of the lever arm and d_{crack} is the distance from the crack surface to the centre of the optical fibre position.*

As previously mentioned, the crack growth was simulated by a scalar damage model in which the damage is indicated by the parameter d and takes the values from 0 to 1 depending on the damage state. When $d=0$ the cohesive element has not started to fracture and when $d=1$ the cohesive element is totally damaged. The cohesive elements were formulated under a bilinear traction-separation law, as depicted in Fig. 4.6. The required input parameters for these elements were, according to [83], the pure modes I/II fracture energies (G_{IC} and G_{IIC}) shown in Table 4.1,

the mode interaction parameter (η) determined in Section 4.3.1, the penalty stiffness (K_p), the interface strength in mode I loading (τ_3^0) and the interface strength in mode II loading (τ_{sh}^0). Further details of the numerical model can be found in [83, 84].

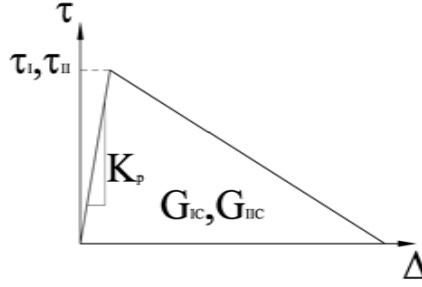


Figure 4.6: *Bilinear traction-displacement law describing the numerical constitutive equations of the cohesive zone model.*

The mode interaction parameter (η) was found by means of fitting the experimental results obtained through different modes by using Eq. (4.2). The penalty stiffness was set by following the recommendations of [83]. The interface strength in mode I loading was determined as the value of the transverse tensile strength and according to [83], in order to obtain accurate results in the simulation, the ultimate strength in mode II (τ_{sh}^0) was calculated as

$$\tau_{sh}^0 = \tau_3^0 \sqrt{\frac{G_{IIC}}{G_{IC}}} \quad (4.9)$$

4.3 Results and Discussion

4.3.1 Identification of parameters for numerical modeling

In this part, the results required for the parametrisation of the numerical model are presented. The R-curves of all the tests were used to determine the NL, VIP, 5%MAX and PROP points for different mode mixtures. According to the standard [1], NL is the point where linearity is lost, VIP is the visual initiation of crack growth, 5%MAX is the minimum value between the 5% increment of the compliance and the maximum load, and PROP is the mean value for all the propagation points.

The R-curves for the specimens tested at 22% mode ratio are shown in Fig. 4.7.

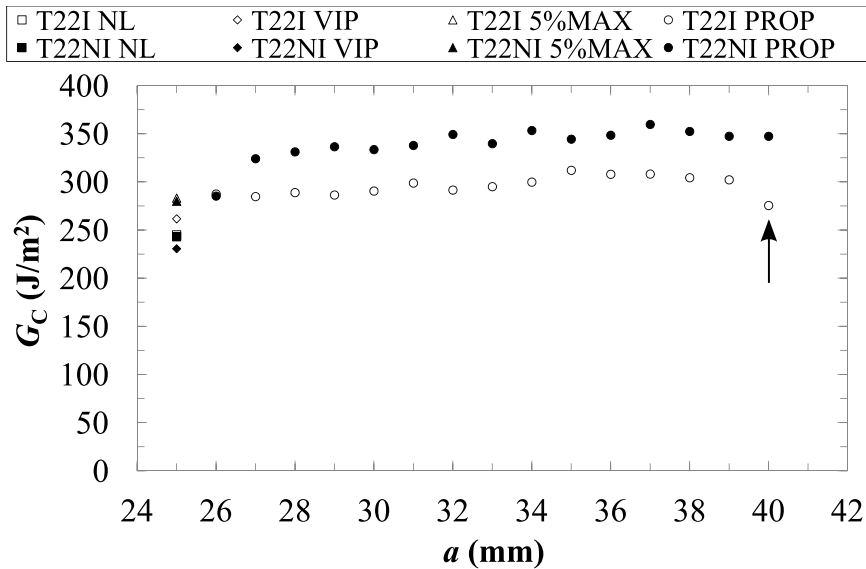


Figure 4.7: *Experimental R-curves for 22% mode ratio tests. Arrows indicate the crack length at the time when the tests are stopped at a certain visual crack length.*

Observe a dip in the critical energy in the zone indicated with an arrow. This effect is due to a relaxation effect. As the tests were stopped for the OLCR measurements, the load decreased. Fig. 4.8 depicts the R-curve for instrumented and non instrumented samples tested at 25% mode ratio. Note that the curves become flat after the first 2 millimetres of propagation, which indicates that the crack growth is stable.

The critical energy against the crack length curves for samples tested at 30% mode ratio are shown in Fig. 4.9. Note that similarly to the curves shown in Figs. 4.7 and 4.8, the curves with and without the optical fibre show the same behaviour which means that its presence has no significant effect on the fracture toughness of the coupon. In addition, note that in this case the critical energies for the instrumented samples are even higher than those of the non instrumented samples. This indicates that there is no effect of the optical fibre on the coupons mechanical behaviour.

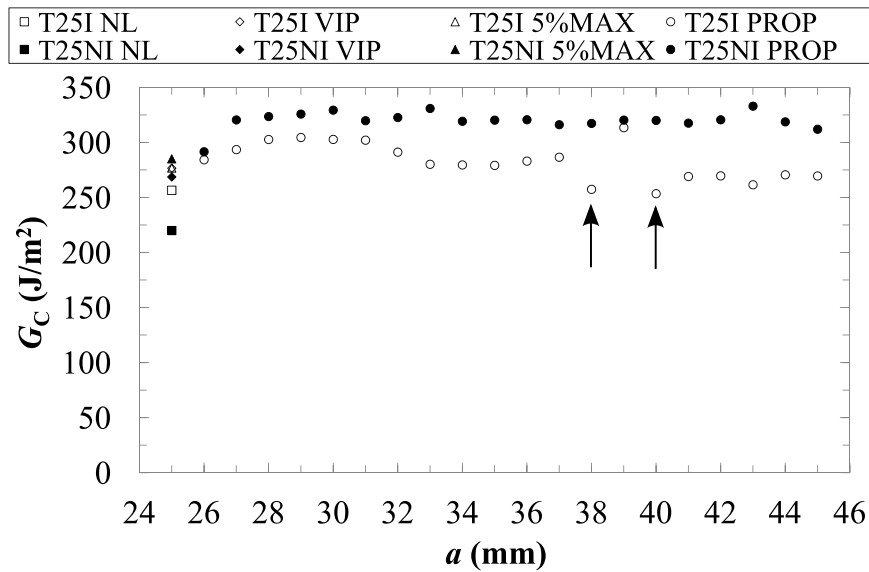


Figure 4.8: *Experimental R-curves for 25% mode ratio tests. Arrows indicate the crack length at the time when the tests are stopped at a certain visual crack length.*

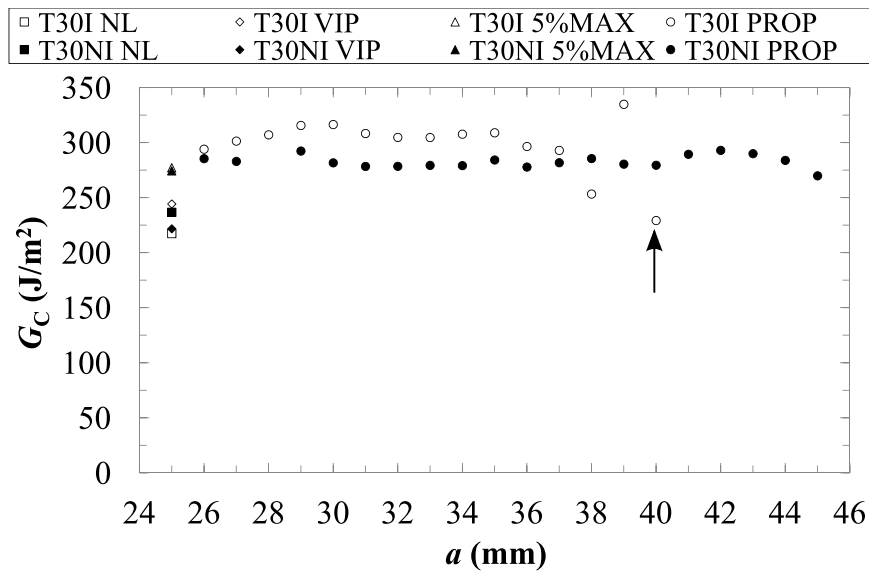


Figure 4.9: *Experimental R-curves for 30% mode ratio tests. Arrows indicate the crack length at the time when the tests are stopped at a certain visual crack length.*

Fig. 4.10 depicts the R-curve for the instrumented sample tested at 50% mode ratio. As previously stated, no dummy sample was tested at 50% mode ratio.

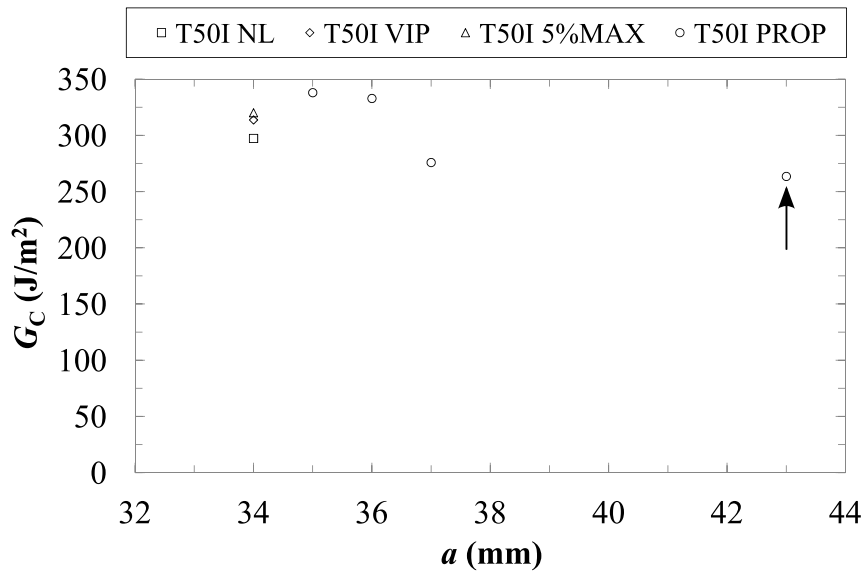


Figure 4.10: *Experimental R-curve for 50% mode ratio test. Arrows indicate the crack length at the time when the tests are stopped at a certain visual crack length.*

The R-curves of samples tested at 75% mode ratio are shown in Fig. 4.11.

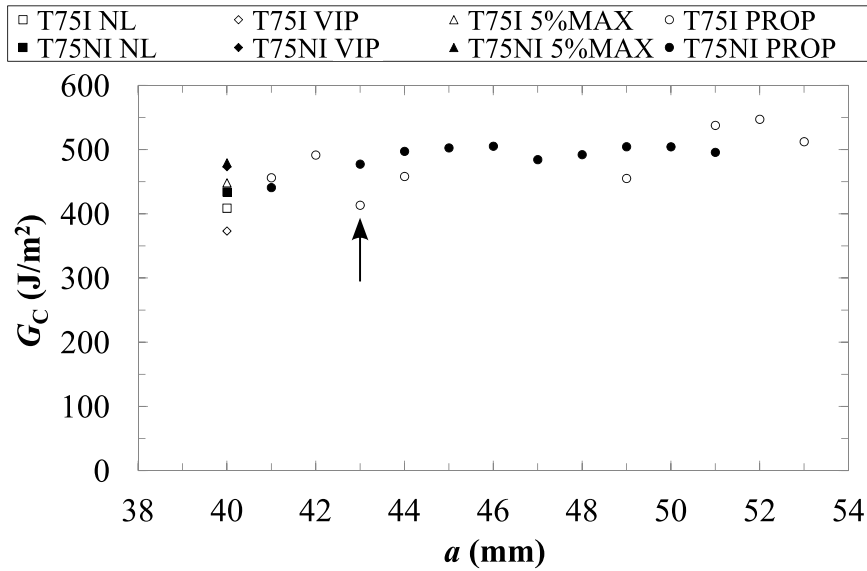


Figure 4.11: *Experimental R-curves for 75% mode ratio tests. Arrows indicate the crack length at the time when the tests are stopped at a certain visual crack length.*

Taking the information on the initiation values of G_C (NL, VIP, 5%MAX) and

the mean of propagation points of all specimens at different mode ratios, the curve of the interaction between modes was constructed. Fig. 4.12 depicts the experimental interaction of modes in the MMB test.

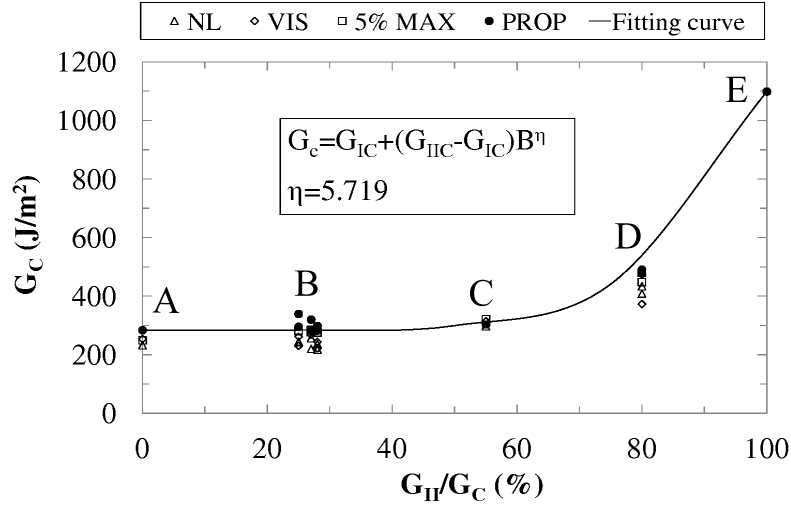


Figure 4.12: Fracture toughness as a function of mode mixture. The mode interaction parameter (η) was determined by fitting the experimental data. A and E corresponds to pure mode I and II fracture energies taken from [81] and [80], respectively. B corresponds to the experimental data of the tests at 22%, 25% and 30% mode mixtures. C is the experimental data of the test at 50% and D corresponds to the experimental data of tests at 75% mode mixture. PROP is the mean of all the propagation points for each mode.

The collected data in the propagation stage were fitted by Eq. (4.2) in order to determine the value of parameter η , needed for the simulations. The fitting results are displayed in Fig. 4.12. Note that for high mixed-mode ratios, a steep growth of the curve appears and taking η as 5.719, a good fit is obtained (correlation coefficient $r^2=0.99$).

Once the tests were carried out, the samples containing an FBG were sectioned normal to the crack direction, in the position where the FBG was located in order to examine the exact position of the fibre in relation to the crack surface (d_{crack}). In Fig. 4.13(a) a micrograph of the sample T25I, used to determine the distance from

the FBG centre to the crack surface, is presented. In all cases, as the optical fibre was adjacent to the crack surface, this distance was $62.5 \mu m$, which is half of the FBG diameter ($125 \mu m$). Fig. 4.13(b) depicts a detail of the optical fibre and the crack surface.

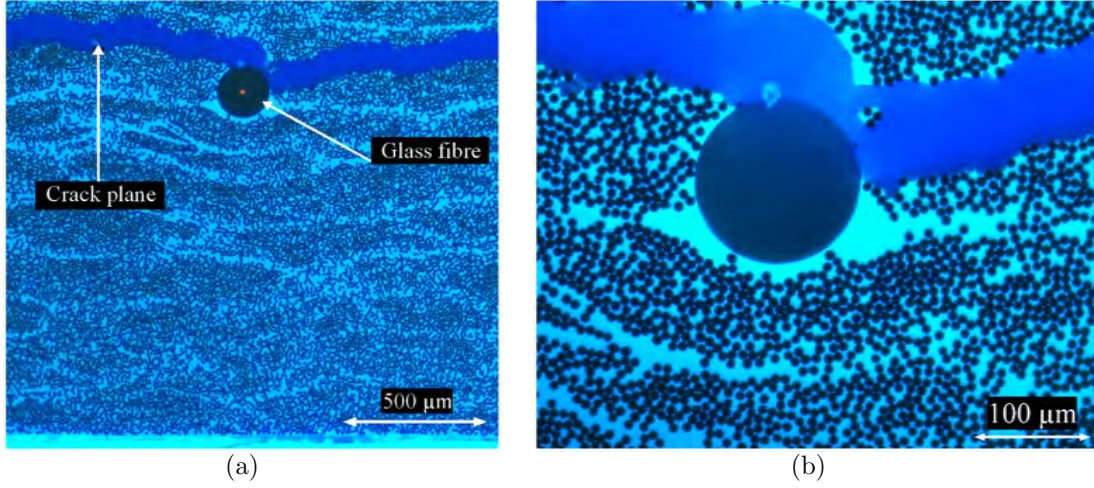


Figure 4.13: (a) sectional micrograph of sample tested at 25% at 5x and (b) detail of the optical fibre and crack surface at 20x.

Once the exact position of the FBG and the mode interaction parameter η were determined, the numerical models were implemented by using the values presented in Tables 4.1 and 4.3.

K_p [$\frac{MPa}{mm}$]	η	τ_3^0 [MPa]	τ_{sh}^0 [MPa]	d_{crack} [μm]
10^6	5.719	28.27	55.5	62.5

Table 4.3: Parameters used for the cohesive elements and geometrical simulations.

4.3.2 Experimental and numerical results

The numerical and experimental results of the load-displacement curves for all samples and different modes are below presented. As the pre-cracking was performed in pure mode I, a smooth crack initiation was observed in all curves. Note that

the specimens without FBG were continuously loaded and the agreement between stopped and non-stopped curves indicate that the embedded optical fibre had insignificant effect on the coupons' global behaviour. Nevertheless, stopping the experiments leads to a small decrease in the load attributed to relaxation. Fig. 4.14 depicts the load versus displacement curves for the sample tested at 22% mode ratio.

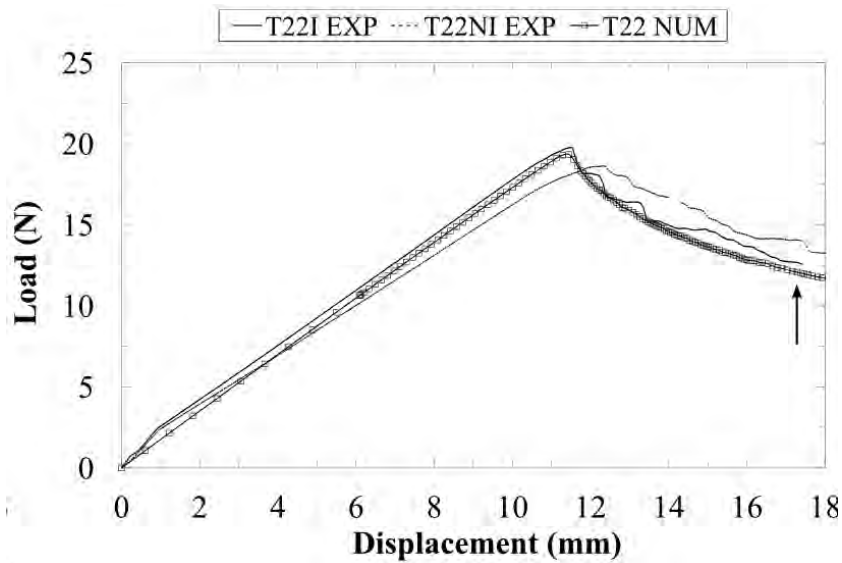


Figure 4.14: *Experimental (EXP) and numerical (NUM) load as a function of displacement curves for MMB test 22% mode mixture. Arrows indicate the moment of the OLCR measurements.*

The load against applied displacement curves for the sample tested at 25% mode ratio are shown in Fig. 4.15.

Fig. 4.16 depicts the same curves for the sample tested at 30% mode mixture. Note a slight difference between the sample containing an optical fibre and the dummy sample. This effect could be attributed to effects induced by the rig at the initial stage of the test or to a slightly different initial stiffness in the coupons. However, there is a full agreement in the propagation stage curve.

Fig. 4.17 depicts the experimental load-displacement curve for an instrumented sample and the numerical simulation at 50% mode ratio.

Finally, Fig. 4.18 depicts the load-displacement curves for samples tested at 75%

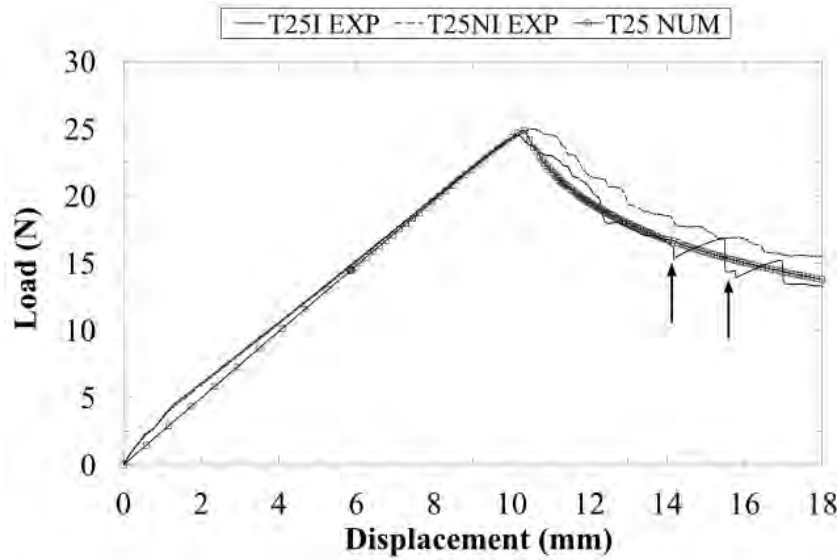


Figure 4.15: *Experimental (EXP) and numerical (NUM) load as a function of displacement curves for MMB test 25% mode mixture. Arrows indicate the moment of the OLCR measurements.*

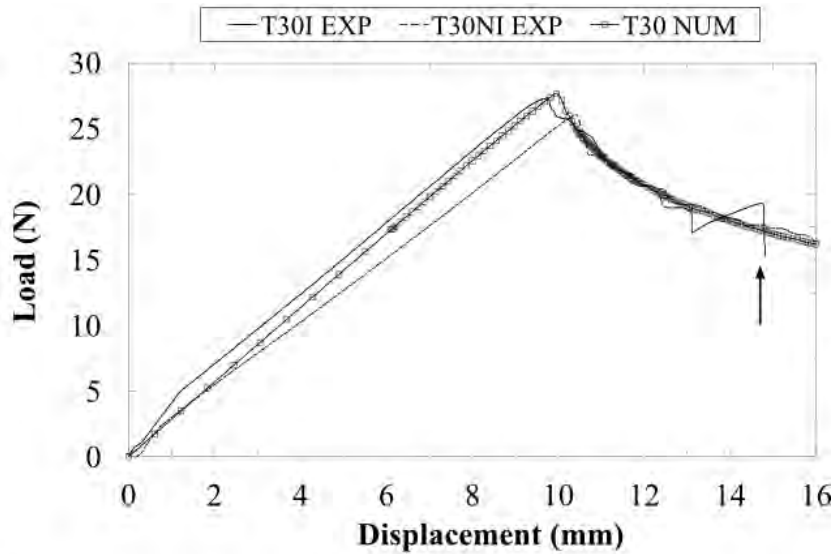


Figure 4.16: *Experimental (EXP) and numerical (NUM) load as a function of displacement curves for MMB test 30% mode mixture. Arrows indicate the moment of the OLCR measurements.*

mode mixture. This includes the results for the instrumented and the non instrumented samples as well as the numerical simulation. Note that the simulations for all mode ratios are in good agreement with the experimental data in relation to both onset and propagation stage.

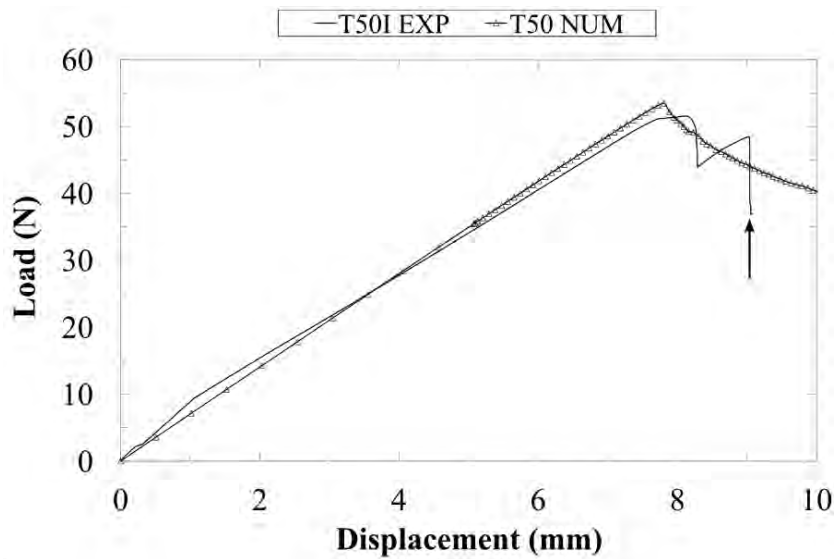


Figure 4.17: *Experimental (EXP) and numerical (NUM) load as a function of displacement curves for MMB test 50% mode mixture. Arrows indicate the moment of the OLCR measurements.*

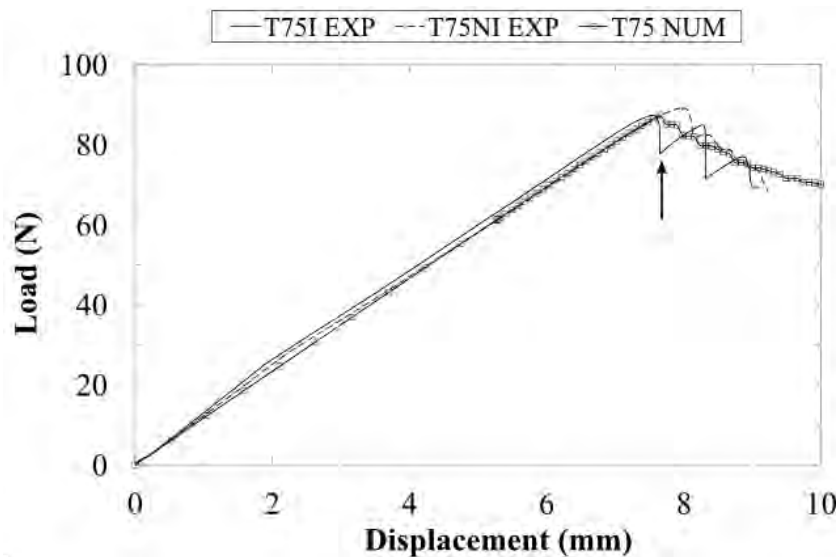


Figure 4.18: *Experimental (EXP) and numerical (NUM) load as a function of displacement curves for MMB test 75% mode mixture. Arrows indicate the moment of the OLCR measurements.*

4.3.3 Crack tip identifications

For the samples containing an FBG, the tests, as previously noted, were interrupted to capture the axial strain profile along the sensor. This strain distribution permitted the crack tip position to be located. As the optical fibre was in the upper arm of the sample, but close to its lower surface, a part of the fibre was in tension (behind

the crack tip) and a part of the fibre was not strained (ahead of the crack tip). By taking a derivative of the experimental axial strain profile, the maximum absolute strain gradient of each curve was found, and in turn, the position of the crack tip was determined. Fig. 4.19(a) depicts the experimental OLCR measurements for the sample tested at 25% mode mixture and the numerical simulations, whereas Fig. 4.19(b) depicts the derivative of the OLCR measurements.

The same curves for mode ratios 22% and 30% are shown in Figs. 4.20(a) and 4.20(b).

Finally, the curves of the OLCR measurements for 50% and 75% mode ratios are shown in Fig. 4.21.

From the numerical models, the crack tip (last element with $d=1$) corresponds at the position with the maximum absolute strain gradient, as shown in Figs. 4.19, 4.20 and 4.21. Thus, the lowest global minima in the experimental strain gradient curves, indicated with arrows, provide a precise evaluator of the crack tip position, as shown by the derivative of the numerical curves where the crack tip measurement is taken. Note that the strain derivatives from the experimental measurements do not show two local minima. Moreover, it is worth mentioning that similar experimental data reported in [25] for mode I and in [61] for mixed mode, indicate a 'bending' of the strain curve at the crack tip. However, such 'bending' is not seen in the data of the present studies. The absence of 'bending' and the two minima in the experimental strain data are attributed to the morphology in the specimens around the crack tip: on one hand, the optical fibre is in contact with the crack surface, and on the other hand, the crack is assumed to be flat, but actually it is not, as shown in Fig. 4.13(b).

Even though the simulations capture well both the onset and propagation of the delamination and the axial strain profile ahead the crack tip, the axial strain profile behind the crack tip, where the upper arm is in bending, is overestimated. The main reason might be due to the fact that the optical fibre was not fully embedded (as depicted in Fig. 4.13) which could lead to a decrease in the strain on the sensor. Modeling the optical fibre by means of the submodelling technique could

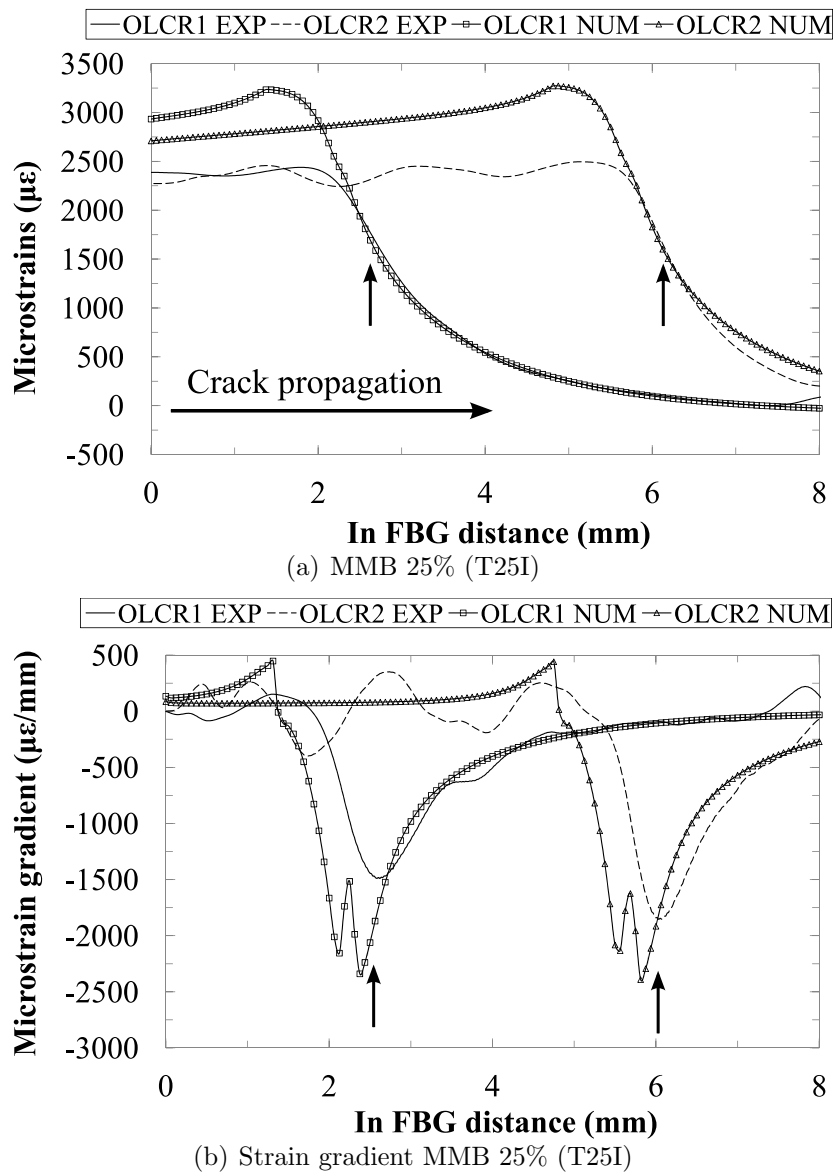


Figure 4.19: *Experimental (EXP) measurement and numerical (NUM) identification of the axial strain profiles. Crack tips are indicated with arrows. (a) depicts the axial strain while in (b) it is shown the maximum strain gradient for each profile.*

decrease this overestimation. In addition, according to Stutz *et al.* [7], the inclusion of a bridging law in the models could better fit the numerical simulations and the experimental curve for at least a few millimetres behind the crack tip.

As previously explained, two different methods were used to find the crack length

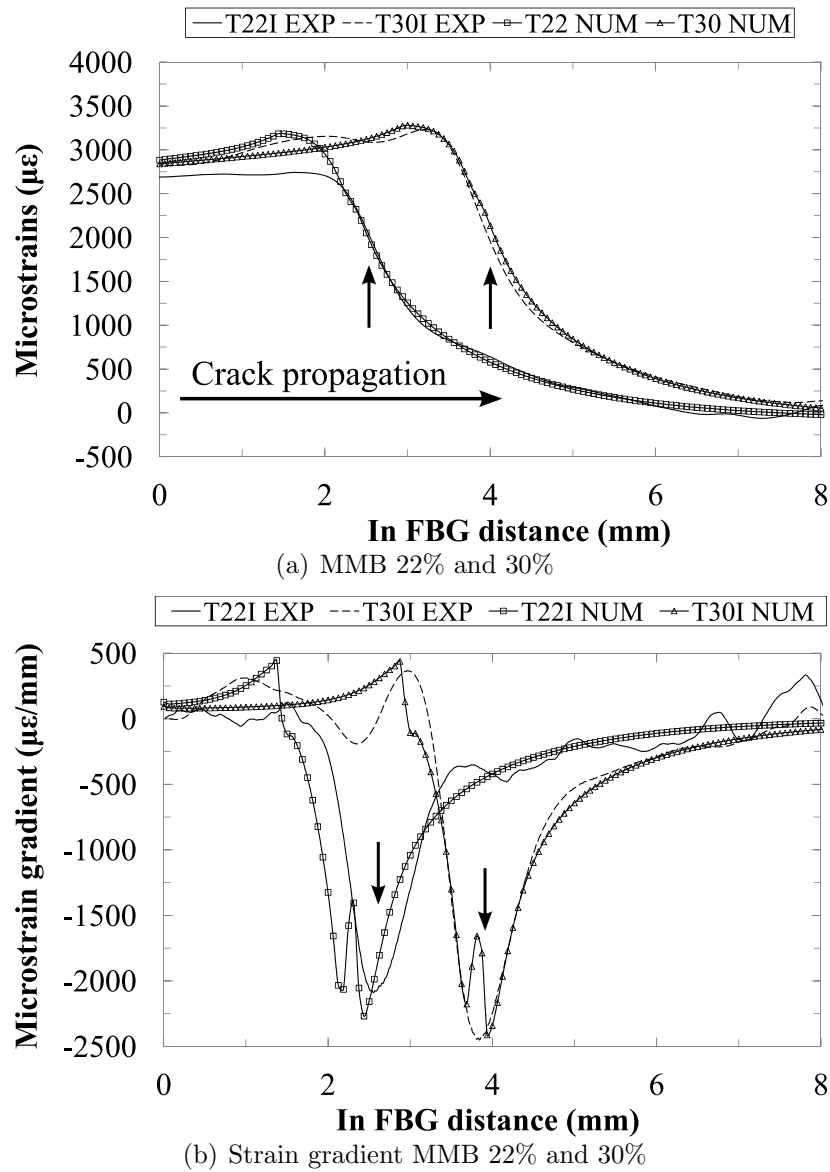


Figure 4.20: *Experimental (EXP) measurement and numerical (NUM) identification of the axial strain profiles. Crack tips are indicated with arrows. (a) depicts the axial strain for two mode ratio tests while in (b) it is shown the maximum strain gradient for each profile.*

at a determined stage of the test: on one hand, the measurement of the axial strain profile together with the derivative and on the other hand, the visual inspection of the lateral marks throughout the test. These methods were checked by a visual inspection of the fracture surfaces after the test when the arms were manually opened. For this analysis the sample T30I, whose final crack front position is depicted in Fig.

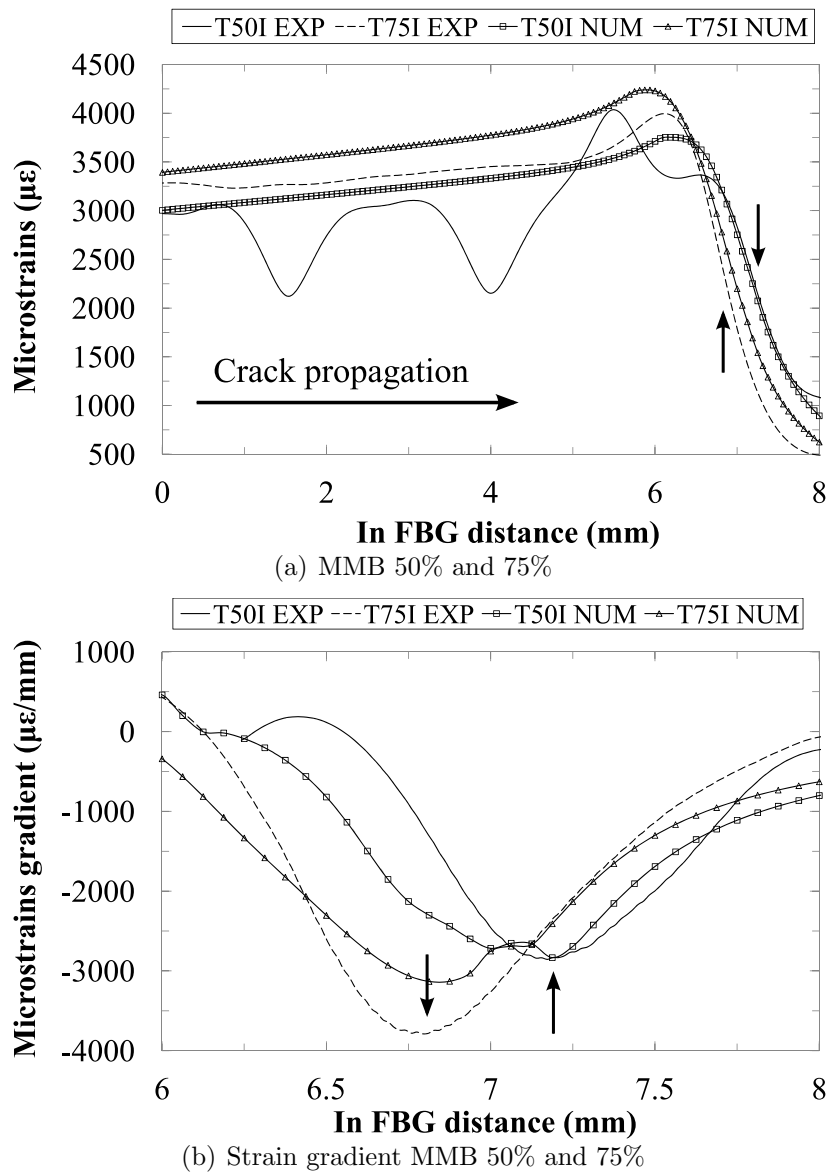


Figure 4.21: *Experimental (EXP) measurement and numerical (NUM) identification of the axial strain profiles. Crack tips are indicated with arrows. (a) depicts the axial strain for two mode ratio tests while in (b) it is shown the maximum strain gradient for each profile. Note that (b) only depicts few millimetres where the crack tip is expected to be according to (a). This has been carried out to increase precision when locating the crack tip.*

4.22, was used.

The distance from the sample end to the inlet of the FBG was 83.7 mm, and

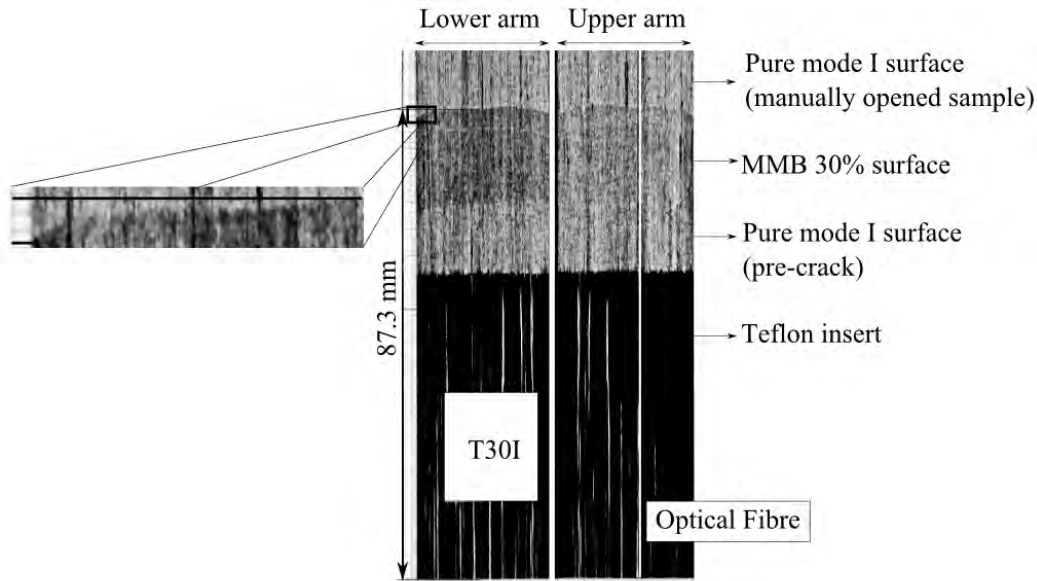


Figure 4.22: Detail of the final crack front position for test T30I. The difference between the lateral mark and the FBG measurement is highlighted in the insert.

according to data shown in Figs. 4.20(a) and 4.20(b), the crack extension in the FBG zone was 3.8 mm. Therefore, the total crack length in relation to the sample end was 87.5 mm, which is in good agreement with the results shown in Fig. 4.22. If the final crack length was checked by means of lateral marks, and by considering the crack length from the sample end, the measured mean distance from both sides of the sample would be 85.1 mm, which gives a difference of 2.4 mm between both methods. Considering the crack length from the load application point (values in Table 4.2) the crack length calculated by means of the long FBG was 42.5 mm. Meanwhile, if the difference of 2.4 mm was applied, the visual crack length would be 40.1 mm, which is in agreement with Fig. 4.9, where the visually measured crack length was about 40 mm. This analysis shows that the FBG sensors can be used as a tool to characterise crack tip position in delamination composite coupons and seemingly as precise as the visual methods used during the test.

As previously detailed, delamination in all the samples was initiated in pure mode I to avoid the initial crack jump. Then, each sample was tested at the desired mode ratio. However, testing samples with 25 mm long initial cracks at high mix

mode ratios induced unstable crack growths. Then, as the loading blocks were glued to obtain a 25 mm long initial crack for all samples, the samples tested at high mix mode ratios were opened in low mix mode ratios in order to enlarge the initial crack length until a stable crack growth was analytically assessed for the highest modes. Fig. 4.23 depicts three different crack fronts caused by three different mode ratio propagations. As the crack front was not straight, the profile gave a different crack length depending on the side from where the crack was observed, as discussed earlier and depicted in Figs. 4.22 and 4.23. According to the ASTM D6671 standard, the final crack front has to be measured at the end of the test to check whether the difference between both sides is less than 2 mm. If this is not the case, the estimation of the fracture energy is not correctly calculated. This analysis indicates that measuring the crack tip with the long FBG is more reliable because there are no uncertainties such as sample painting, lateral marks drawing, or errors in the visual crack growth controlling.

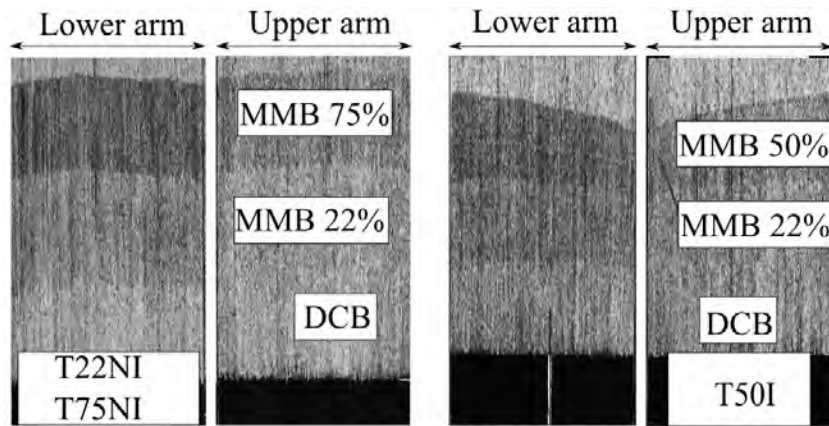


Figure 4.23: Crack propagation surface detail of three different mode propagations.

Note in Fig. 4.23 that the fracture surface at 50% mode mixture shows a large difference between both sides. This implies that knowing the exact crack tip position inside a sample is essential, since using the visual data becomes highly erroneous. It has to be highlighted that the crack surface of pure mode I opened specimens is not clearly defined, but when the mode mixture increases, the surface becomes darker and easy to identify. After the last mixed mode propagation, all the samples were manually broken (i.e. the arms were split) in order to inspect the fracture surfaces.

4.4 Conclusions

A method for crack tip positioning in composite coupons under different mixed-mode I/II ratios has been presented. A long FBG sensor embedded in a unidirectional composite sample precisely gave the position of the crack tip in different stages of the test. In addition, this crack tip location has been proved to be more effective than visual inspections during the test, and the precision of the location, by means of axial strain profile, has been improved by the use of the derivative of the axial strain being the maximum strain gradient perfectly localised. These results were confirmed through numerical simulations and visual inspection of the fracture surface after the test.

A method for obtaining the necessary parameters for the numerical modeling has been presented. After testing at different mode mixtures, the curve of the fracture energy as a function of mode mixture was constructed, and by fitting, the mode interaction parameter was determined. In addition micrographs were carried out to unambiguously locate the optical fibre within the samples.

A method for fixture weight compensation has iteratively been performed giving good results in terms of crack growth stability, including high mode ratios. The samples to be tested at high mode II ratio were opened a few millimetres in low modes so that the larger initial crack length gave a stable propagation of the crack front and the sudden onset of delamination was avoided.

It has been proved that the effect of the embedding FBGs in the samples' mechanical properties is not significant, neither in the initial loading range nor in the propagation stage.

Chapter 5

Real time crack tip monitoring in a DCB fatigue test

5.1 Introduction

High-cycle fatigue is a well known phenomenon of damage initiation and propagation in composites [85–89]. The test to measure the onset of damage is standardised [2], whereas there is a lack of a standard procedure to determine the crack growth rate (da/dN), even though research efforts have been focused on fatigue propagation standardisation in recent years [90, 91]. One of the most common approaches for the analysis of delamination under mode I fatigue loading is the fracture mechanics approach, which relates the fatigue crack growth rate, da/dN , to the amplitude of the energy release rate, ΔG . The $\log(da/dN)$ - $\log(\Delta G)$ plot can be divided into three regions: the energy threshold where the crack growth rate becomes unmeasurable (I), the region close to static failure (III), and, in between, the linear propagation zone (II), well described by the Paris law [92, 93]

$$\frac{da}{dN} = Q \left(\frac{\Delta G}{G_C} \right)^m \quad (5.1)$$

where a is the crack length, N the number of load cycles, and Q and m empirical material constants. The cyclic variation of the energy release rate (ΔG) is dependent on the loading conditions, and G_C is the static fracture toughness of the material. The loading term in the Paris law may be also expressed as a function of the maximum energy release rate G_{Imax} , or by means of the stress intensity factor,

$K_{I_{\max}}$ or ΔK_I [86].

In order to measure the crack growth rate, information on the crack length over the whole fatigue test is required. As specimen compliance can be easily monitored during the test, and there is a unique relationship between compliance and crack length, it is preferable to monitor compliance and then infer crack length [94]. Only a small set of crack tip positions and the corresponding specimen compliance values are needed to fit both parameters [86]. Crack tip positions are commonly determined by means of visual methods such as traveling cameras or microscopes [86, 87, 90]. Such methods mainly introduce two uncertainties. On the one hand, monitoring the crack length by means of visual methods does not constitute a robust method since it is considered operator-dependent [91]. On the other hand, as reported in [95], the fact that the crack length is measured at the edge of the coupons adds imprecision to the measurement because the crack front is not straight. The use of fibre Bragg grating sensors (FBGs) has been proved to overcome these limitations in fatigue propagation monitoring [8, 62, 64, 65] as it provides a direct and objective measurement of the crack length. In addition, this method is completely independent of the operator and the location of the sensor at the centre of the crack front avoids any problem associated with the crack tip monitoring through the edge.

FBG sensors are being increasingly used to measure the internal strain field of composite structures [20, 37, 38] mainly due to their low intrusiveness and their accuracy [39, 41]. [7, 25, 95] demonstrate that, the disturbance of the optical fibre to the energy release rate is minimal and very local in quasi-static delamination tests under different crack propagation modes. In addition, these works demonstrate that a direct determination of the strain field with long FBG sensors is possible through the Optical Low Coherence Reflectometry (OLCR) interrogation technique. This technique enables the measurement of the length, location and local Bragg wavelength (i.e. local strains distribution) of the FBGs [7, 24, 25, 59]. The measurements of non-homogeneous strain fields are the principal benefit of this method [26], as the full strain distribution can be measured without the need to know the initial strain state. In relation to the use of FBGs to monitor fatigue delamination, Epaarachchi *et al.* analysed the response of long FBGs embedded in glass fibre cross-ply compos-

ites [62] concluding that the shape of the output FBG spectra contained valuable information about the composite structure such as local crack initiation/propagation stage. In [64], multiplexed 6 mm long FBG sensors were used to monitor the fatigue crack growth in adhesively bonded joints of thick composite laminates, and achieved a resolution similar to that of ultrasonic testing. In the work presented by Stutz *et al.* [8], FBG arrays (each FBG was 1 mm long) were used in composite samples to determine the bridging traction present in mode I fatigue crack propagation. The authors demonstrate that, strain measurements near the delamination zone are feasible by using multiplexed short FBG sensors to construct quasi-continuous strain profiles along the sensor. A quasi-continuous strain evolution over the number of cycles was also obtained by means of multiplexed FBGs in [65], where the fatigue delamination was monitored in open-hole specimens.

In this chapter, FBGs are used to monitor the crack growth in mode I fatigue tests and then, this information is used to construct the crack growth rate curves. This method is compared to common techniques, which are based on the optical measurements at the edge of the coupons. Results indicate that, even though all curves show the same slope, the energy thresholds are strongly dependent on the crack measurement method. Taking into account the high accuracy of the measurements given by the FBGs, the present work shows that, for the CFRP studied, the errors in the energy threshold calculations reached about 11% when using visual inspection methods.

5.2 Methodology

5.2.1 Specimens

Carbon/epoxy unidirectional specimens were cut from a single plate manufactured by stacking 36 UD layers of AS4/8552 unidirectional pre-pregs. A Teflon film 20 μm thick and 60 mm long was placed at the midplane, between layers 18 and 19, to act as pre-crack insert. Two instrumented samples (FAT1 and FAT2) and one non instrumented sample (FAT3), which was used to check the effects of the optical fibre into the coupons' behaviour, were tested. The initial dimensions of the coupons

were 200x25 mm with a total thickness of 4.5 mm.

Two parallel FBG arrays were embedded two layers above the crack plane (between layers 20 and 21) in each instrumented sample, and aligned to the reinforcing fibres. The separation between the optical fibres in the X direction was 2 mm (see Fig. 5.1). Each FBG array consisted of 4 FBG sensors written into a single mode fibre SM28 with a diameter of 125 μm . The length of each FBG sensor was 1 mm, the Bragg peaks were located between 1525 and 1540 nm and spaced by 5 nm. The distance between FBGs' centres was 2mm in the Z direction, as the manufacturer recommended a separation of 1 mm between each sensor in the same fibre. The two parallel arrays were embedded in each specimen (see detail in Fig. 5.1) in order to monitor the crack length every millimetre. However, as the placement of the fibres is a manual process, this 1 mm offset was not fully achieved. The exact position of each one of the FBG sensors was accurately determined by means of the OLCR technique. As the optical fibre was cut at the sample end (left part of the specimens shown in Fig. 5.1), the OLCR interrogation gave a peak of intensity for the fibre end, and a peak of intensity for each FBG in a distance scale. The location of each FBG was converted to crack tip positions by taking into account the location of the load introduction point. The position of each FBG, in relation to the loading blocks, is reported in Table 5.1.

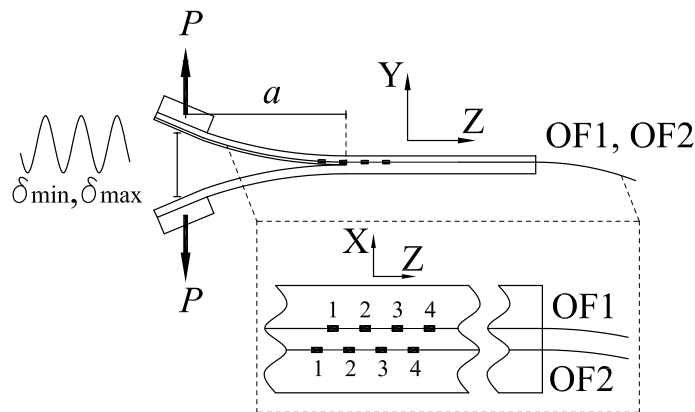


Figure 5.1: Schematic of the experimental setup with the positions of the FBGs (see Table 5.1) in the two parallel optical fibres. 1,2,3 and 4 are the four FBGs in each optical fibre. Photographs were taken from the edge of the Y-Z plane.

Specimen	OF	Sensor location [mm]			
		FBG1	FBG2	FBG3	FBG4
FAT1	1	76.08	78.43	80.34	82.45
	2	77.76	79.83	81.74	83.82
FAT2	1	73.87	75.92	77.83	80.07
	2	74.06	76.37	78.25	80.32

Table 5.1: *Distance of each sensor in relation to the loading blocks.*

5.2.2 Fatigue tests parameters

The crack length increment in a fatigue test under stroke control with constant maximum and minimum displacement, can be estimated by means of the expression of the energy release rate for a DCB specimen assuming single beam theory as

$$a_f - a_0 = a_0 \left[\left(\frac{G_{\text{Imax}}^0}{G_{\text{Ith}}} \right)^{1/4} - 1 \right] \quad (5.2)$$

where a_0 is the initial crack length, a_f is the final crack length, G_{Imax}^0 is the maximum energy release rate during each cycle at the beginning of the test and G_{Ith} is the energy threshold for which the crack no longer grows. The crack tip was placed 3 to 5 mm away from the first FBG sensor in order to avoid the loss of data due to an initial rapid crack propagation. Due to the spatial distribution of FBGs, the extension of crack length, $a_f - a_0$, was set to 13 mm. As the preliminary tests showed that $G_{\text{Imax}}^0/G_{\text{Ith}}$ was around 2, the desired initial crack length, a_0 , resulted to be 70 mm.

The fatigue tests were carried out at a frequency of 5 Hz and performed under controlled stroke with constant maximum and minimum displacement (δ_{max} , δ_{min}) in a servo-hydraulic MTS[®] 858 test machine with a load cell of 500 N. All samples were initially pre-cracked statically in pure mode I. After the pre-crack stage, a quasi-static DCB test was performed for each sample according to the standard ASTM D5528 [3] in order to determine the value of the critical displacement (δ_{cr})

corresponding to the 70 mm initial crack length of the fatigue tests. Then, the maximum value of the cyclic displacement (δ_{\max}) was computed from

$$\left(\frac{\delta_{\max}}{\delta_{\text{cr}}}\right)^2 = \frac{G_{\text{Imax}}^0}{G_{\text{IC}}} \quad (5.3)$$

where G_{IC} is the mode I static fracture toughness. This equation is valid as long as the fatigue test is performed over a specimen of the same elastic characteristics and with the same initial crack length as in the static test. The minimum value of the displacement for each fatigue test was computed taking into account δ_{\max} , and the amplitude ratio ($R = \delta_{\min}/\delta_{\max}$). The ratio $G_{\text{Imax}}^0/G_{\text{IC}}$ was set to 1, 0.85 and 1 for the tests of the samples FAT1, FAT2 and FAT3 respectively, and R was set to 0.2 for all tests.

5.2.3 Determination of crack length

The compliance of the specimen was recorded during the test in the linear region of the $P - \delta$ curve for every cycle (dynamic compliance), according to the method described in [96, 97]. The crack length was monitored by two different methods: the visual inspection method, and the method using multiplexed FBGs. The visual method, referred to as VIS in this work, consisted of taking photographs of the specimen edge, by means of a high resolution camera, at certain times and without stopping the test (Fig. 5.2). Pictures were taken every 10 cycles during the first 1,000 cycles and then, sets of 10 pictures were taken at increasing intervals in conjunction with the increasing number of cycles (at every 1,000 cycles up to 20,000 cycles, at every 10,000 up to 100,000 and at every 50,000 cycles from there on). After the test, the pictures were analysed and those showing the highest displacement (the crack tip was clearly observable) were selected for the crack length measurement.

The second method, referred to as FBG in this work, consisted of measuring the crack length with multiplexed FBGs. This technique is well reported in [7, 8]. Having 8 FBGs in each sample, with highly accurate known positions (see Section 5.2.1), and identifying the cycle at which the crack tip reaches each of them, a discrete set of crack lengths was obtained. The signal of each FBG was recorded at a frequency of 100 Hz and the test frequency was 5 Hz, therefore 20 points per cycle were measured.

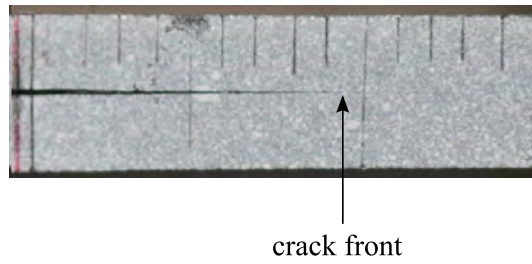


Figure 5.2: Detail of the photographed specimen edge to monitor the crack front using the visual method.

The evolution of the maximum of these 20 points with the number of cycles is shown in Fig. 5.3, for the four sensors (FBG1, FBG2, FBG3 and FBG4) of one single fibre (OF2) embedded in sample FAT2. Note that, the number of cycles is shown in logarithmic scale and that the moments when the crack was detected (v-shaped dip) are indicated with arrows as in [8].

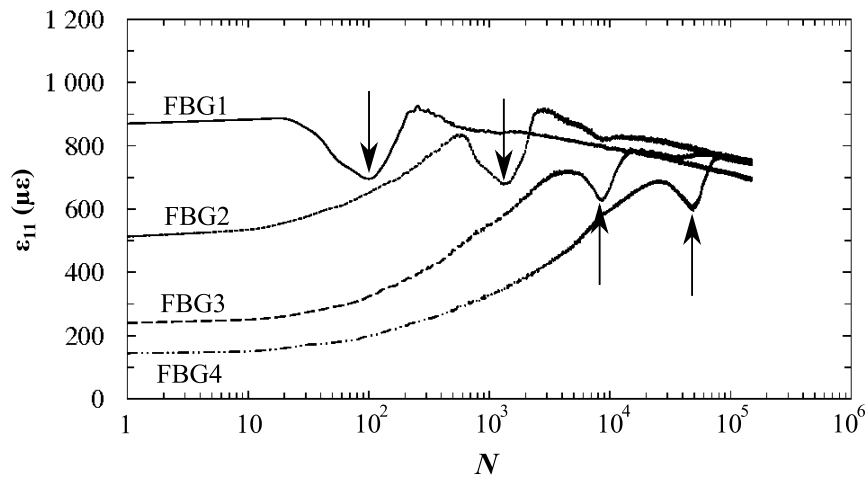


Figure 5.3: Maximum strain per cycle profiles against the number of cycles obtained from measurements in OF2 embedded in sample FAT2. Arrows indicate the moment the crack tip was measured.

Once the discrete sets of crack lengths were known by the VIS and FBG methods, and making use of the continuously recorded compliance, a direct relation could be

inferred between compliance and the crack length measured by both methods. Then, as in [94], the compliance and the crack length were fitted by means of

$$C = Da^n \quad (5.4)$$

where C is the measured compliance, a the crack length and D and n are the fitting parameters to be determined. Making use of the full evolution of the compliance over the number of cycles together with Eq. 5.4, the crack length of the whole test was computed. Then, da/dN was immediately deduced by simple derivative. On the other hand, G_{Imax} was calculated as

$$G_{\text{Imax}} = \frac{P_{\text{max}}^2}{2B} \frac{dC}{da} \quad (5.5)$$

where P_{max} is the maximum load at every cycle recorded over the fatigue test, B the width of the specimen, and dC/da the variation of the compliance with respect to the crack length during the fatigue propagation test, which can be deduced by a derivative of Eq. 5.4.

5.2.4 Strain measurements

Wavelength multiplexing consists of writing several FBGs in the same optical fibre, but with different periods. Then, each FBG has its own characteristic wavelength, also known as Bragg wavelength (λ_{B_0}), which is related to the axial strain state of the FBG. When the sensor is loaded, the changes of the reflected wavelength are related to the changes in the strain state by

$$\frac{\Delta\lambda_B(z)}{\lambda_{B_0}} = (1 - p_e)\varepsilon_z(z) \quad (5.6)$$

where $\Delta\lambda_B(z)$ is the shift of the local wavelength, and p_e is the opto-mechanical coefficient which takes the value of approximately 0.22 [82]. Note that, this is a simplified form supposing no out-of-axis strain other than those created by Poisson's coefficient and that the strain is constant over the sensors' length (1 mm). The interrogation of multiplexed FBGs during the test gives just one peak per sensor that, in this work, were measured with the SM130 interrogator from MicronOptics®.

5.3 Results and Discussion

Table 5.2 contains the mode I static fracture toughness for all samples obtained in the quasi-static DCB tests. As described in the ASTM D5528 standard [3], NL is the non-linear point where the linearity in the load-displacement curve is lost, VIP corresponds to the point where the crack front is visually seen to move, 5% MAX is the minimum value between the 5% increment of the compliance and the maximum load. PROP_{av} is the average of the propagation values for each measured crack length. Onset and averaged propagation data show slight variations within 0-10% range. Accounting for the fact that FAT1 is an instrumented sample and FAT3 is a non instrumented sample, the observed differences in the critical energies cannot be attributed to the presence of the optical fibre.

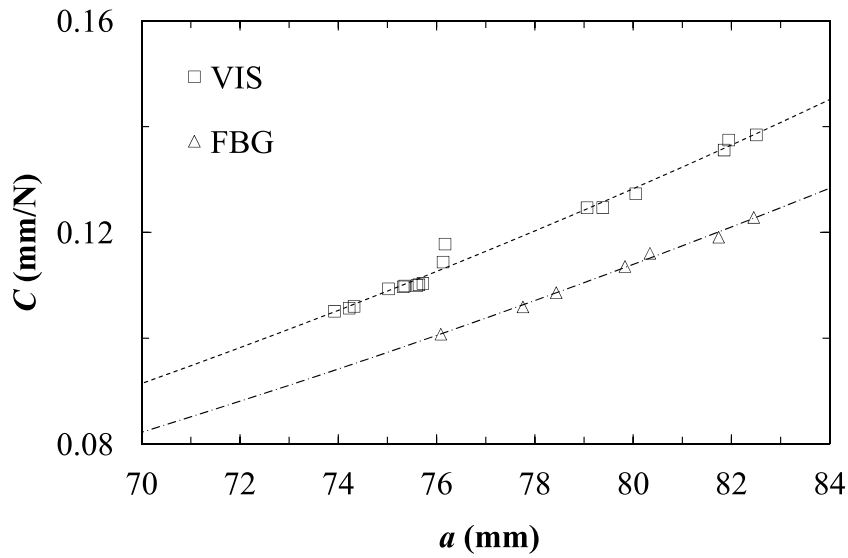
Specimen	$G_{\text{IC}} \left[\frac{\text{J}}{\text{m}^2} \right]$			
	NL	VIP	5% MAX	PROP_{av}
FAT1	232	224	252	263
FAT2	215	231	239	284
FAT3	236	225	257	268

Table 5.2: Critical energies obtained in the quasi-static DCB tests.

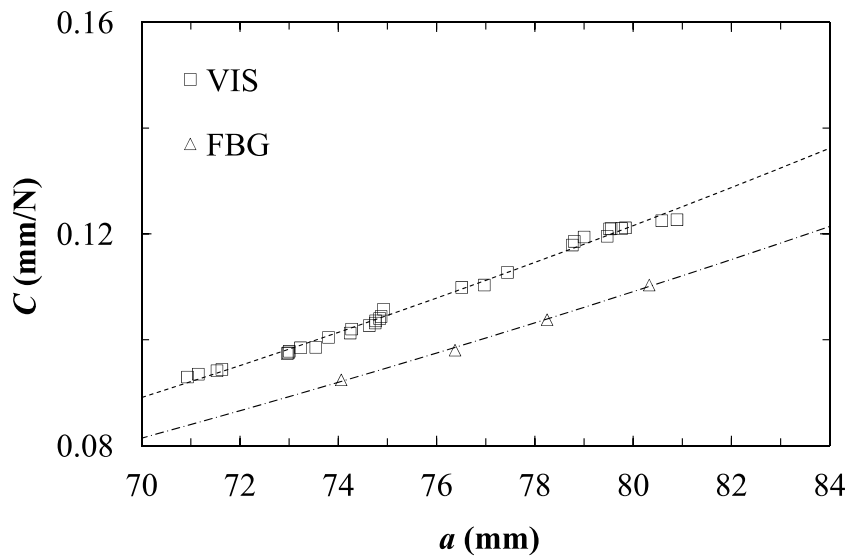
The fittings of the recorded compliance versus the measured crack lengths, were carried out through a potential law (according to Eq. 5.4) and shown in Fig. 5.4 for samples FAT1 and FAT2. Note that, 7 and 4 FBG measurements are shown in Figs. 5.4(a) and 5.4(b), respectively. This is due to the loss of one FBG in the first case, and the loss of a full FBG array in the second case.

The fitting carried out by the visual method in sample FAT3 is shown in Fig. 5.5.

The results of the fittings are reported in Table 5.3. The quality of the fittings was good ($r^2 > 0.98$), especially for the FBG method, where r^2 was always higher than the VIS method. This fact supports the higher precision and reliability of the data collected by means of FBGs.



(a) Specimen FAT1



(b) Specimen FAT2

Figure 5.4: Dependence of the specimen's compliance with the crack length for samples FAT1 and FAT2. Markers correspond to experimental values and lines correspond to the fitting curves.

The theoretical exponent n for an analysis based on single beam theory would be 3, which indicates that a data reduction method to obtain fatigue parameters based on this approach would clearly produce erroneous results.

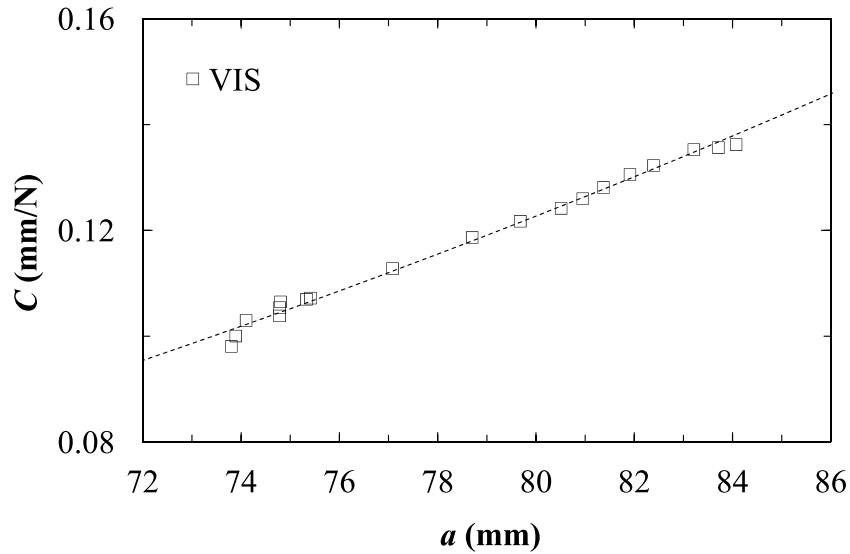
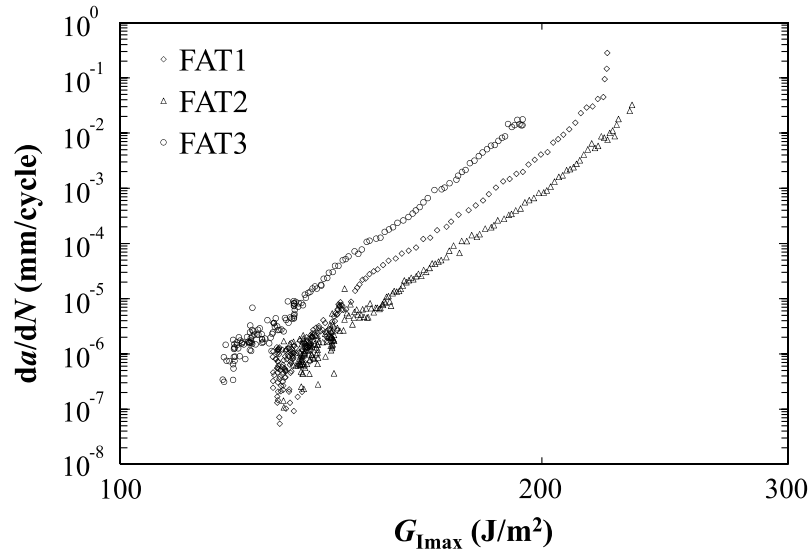


Figure 5.5: Dependence of the specimen's compliance with the crack length for sample FAT3. Markers correspond to experimental values and the line correspond to the fitting curve.

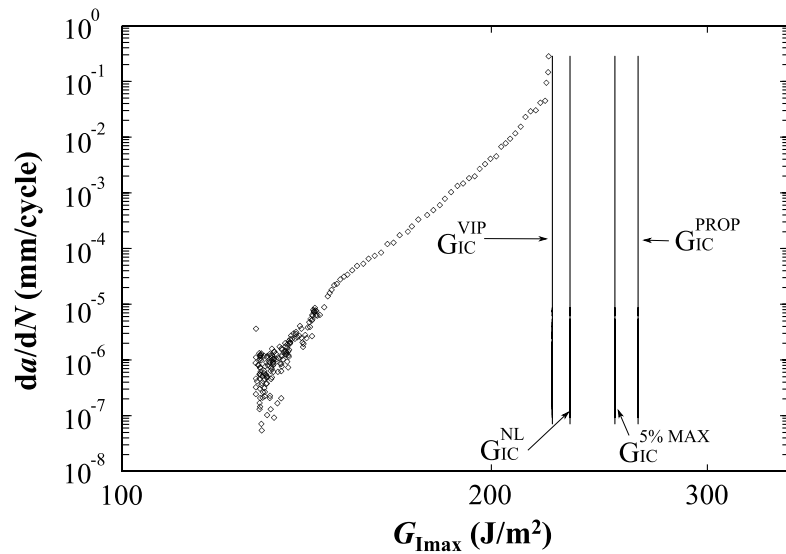
Specimen	Method	D	n	r^2
FAT1	VIS	1.943×10^{-6}	2.532	0.984
	FBG	2.564×10^{-6}	2.442	0.995
FAT2	VIS	4.506×10^{-6}	2.328	0.993
	FBG	7.314×10^{-6}	2.193	0.997
FAT3	VIS	3.543×10^{-6}	2.3853	0.988

Table 5.3: Parameters of the fitted data.

The non intrusion of the optical fibre into the specimens' behaviour under mode I fatigue test was also checked. Fig. 5.6(a) depicts the crack growth rate curves obtained by the visual method in two instrumented samples (FAT1 and FAT2) and in one non instrumented sample (FAT3). The curves show an almost identical slope and differ only in G_{Ith} . They cannot be grouped into instrumented and non instrumented samples, which indicates that the optical fibre is not changing the global behaviour of the composite coupons. In addition, G_{Ith} was 130, 138 and 120 J/m² for specimens FAT1, FAT2 and FAT3, respectively. Therefore, the maximum difference observed in the G_{Ith} (between samples FAT2 and FAT3) reaches about 13%, which is in the range of known variability in fracture toughness tests.



(a)



(b)

Figure 5.6: Fatigue crack propagation as a function of $G_{I\max}$ curves for (a) three samples obtained using the visual method and (b) compared to G_{IC} obtained in quasi-static tests for sample FAT1.

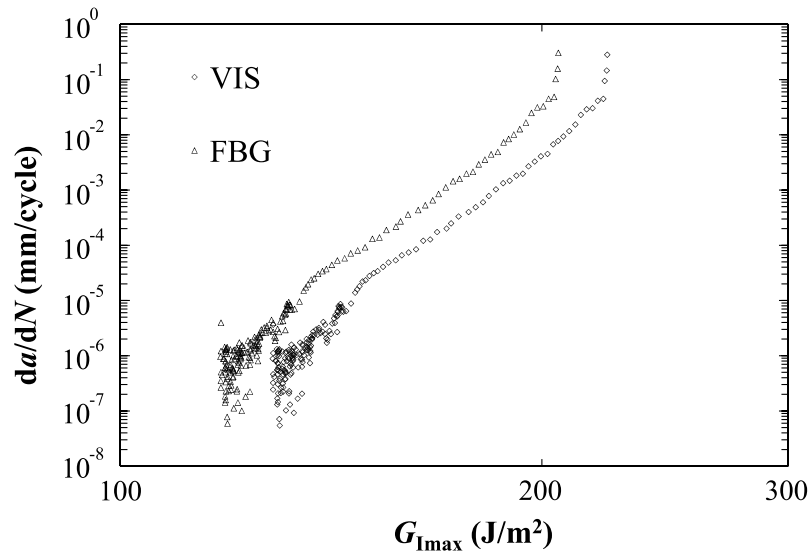
The zone of very high crack growth rates, usually referred to as zone III, is compared to the static critical energies in Fig. 5.6(b). Using the visual method, it depicts the crack growth rate result for sample FAT1, and compares it to all measured static critical energies (Table 5.2). Note that, the initiation of the propagation in

the fatigue tests corresponds to the onset of the static critical energy, calculated by means of the VIP and NL methods. Nevertheless, the 5% MAX and especially the averaged propagation values, are far from the initiation in fatigue. This fact indicates that, the damage mechanisms acting in the static growth (propagation) include contributions not acting under fatigue loading. One of these mechanisms could be fibre bridging that, as stated in [8], has a lower effect under fatigue loading than in monotonic loading.

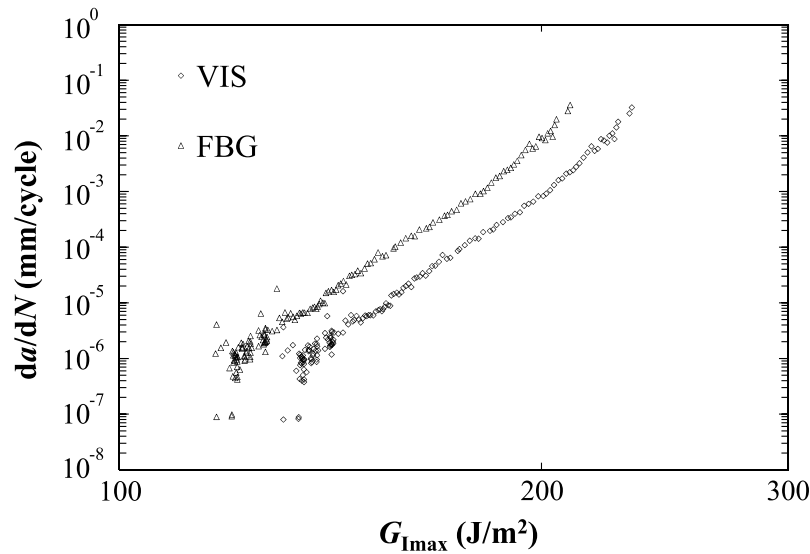
The crack growth rate versus G_{Imax} curves for specimens FAT1 and FAT2 are shown in Fig. 5.7. Note the low noise and the fact that the three expected zones of a fatigue test are clearly evidenced in these charts, i.e., the stage close to static failure zone where the crack growth raises as we approach the static critical energy; the propagation where the Paris law of Eq. 5.1 is obeyed and the zone where da/dN decreases strongly approaching a threshold (G_{Ith}) below which the crack growth rate is not measurable. It should also be remarked that, the da/dN data spans over 8 orders of magnitude, whereas 6, 4 and 5 magnitude orders are shown in [87], [88] and [89], respectively.

Zone III in specimen FAT2, does not appear in Fig. 5.9(b) because the ratio $G_{\text{Imax}}^0/G_{\text{IC}}$ was set to 0.85, whereas in specimen FAT1, this ratio was set to 1. The parameters of the Paris law (Eq. 5.1) for each instrumented specimen are summarised in Table 5.4. As FBGs have been proved to measure the location of the crack tip with high precision, the results given by the sensors are taken as the reference values. For a given specimen, a maximum relative error of 10.4% is observed in the energy threshold, whereas the slopes are almost identical (i.e. the error is less than 0.4%).

As reported in [95], the crack length measured from the specimen edge shows a significant offset with the crack length measured at the centre of the crack front. Taking into account that both methods rely on the same measurement of the compliance, the differences observed in the crack propagation results between the VIS and FBG methods are derived from the different zone used to monitor the crack. While the FBGs are measuring in the middle of the sample, the photographs used in



(a) Specimen FAT1



(b) Specimen FAT2

Figure 5.7: Fatigue crack propagation as a function of $G_{I\max}$ curves.

the VIS method monitor its edge. Fig. 5.8 depicts the evolution of the crack length for both methods over the number of cycles. The difference in the computed crack lengths (Δa , represented with cross markers) between both methods, increases with the number of cycles.

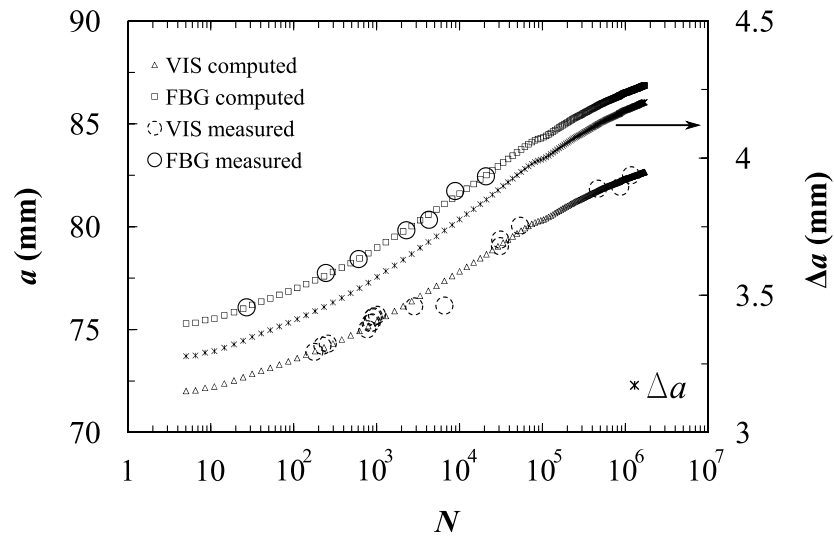
The reason behind the fact that the difference in the crack length determined

Specimen	Material constant	VIS	FBG	relative error (%)
FAT1	Q	2.62×10^{-50}	4.62×10^{-50}	76.33
	m	20.57	20.83	0.13
	$G_{\text{Ith}}[\text{J}/\text{m}^2]$	129.93	119.25	8.22
FAT2	Q	1.55×10^{-45}	3.64×10^{-45}	134.84
	m	18.77	18.83	0.32
	$G_{\text{Ith}}[\text{J}/\text{m}^2]$	130.82	117.22	10.40

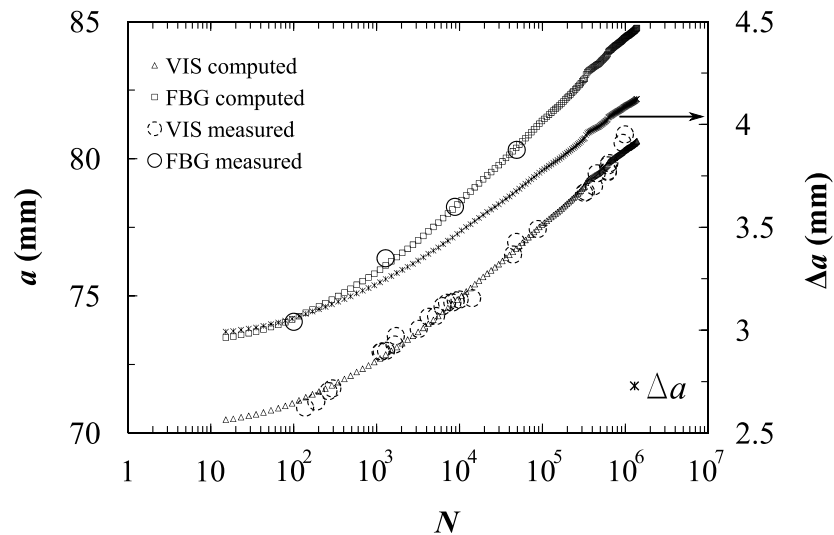
Table 5.4: *Material constants in the Paris law, obtained with different methods, in the instrumented samples.*

by both, the VIS and FBG methods, evolves as the crack extends, might be attributed to an intrinsic phenomenon related to the length of the fracture process zone changing with the crack length. This could be related to second order effects of the deflection and rotation at the arms' root, which would depend on the arm length [98, 99]. The description of the specimen arms deflecting according to single beam theory and assuming the fulfilment of the linear elastic fracture mechanics hypotheses, can not account for this effect. This hypothesis could be clarified by means of long FBGs. These sensors allow the spatial strain profile along the sensor's length to be monitored [7, 25, 95]. This procedure would enable the full reproduction of the strain state of the FBG at different stages of the fatigue test, thus providing insights into its evolution. However, this technique implies stopping the tests at each measurement, as each OLCR measurement takes approximately 30 minutes.

To reinforce the hypothesis of the consequences of monitoring the crack from the specimen's edge, a particular correction to the visual measurement, for the given specimens and configurations, is proposed. It consists of adding to each measured crack length (VIS method) the corresponding increment Δa , shown in Fig. 5.8. Then, the parameters of the compliance calibration (Eq. 5.4) are recalculated and the crack length is computed for the whole test. The crack propagation curves of the FBG measurement, the visual measurement (VIS) and the corrected visual measurement (VIS_c) are shown in Fig. 5.9. The corrected curve clearly approaches the



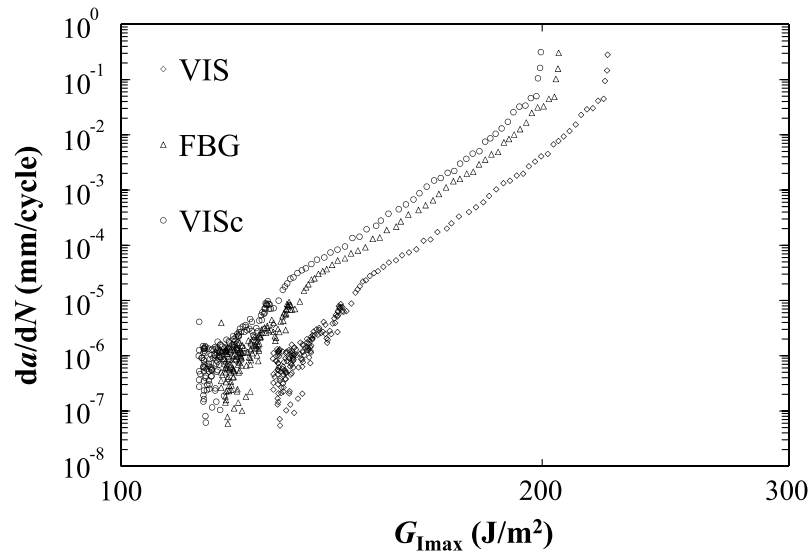
(a) Specimen FAT1



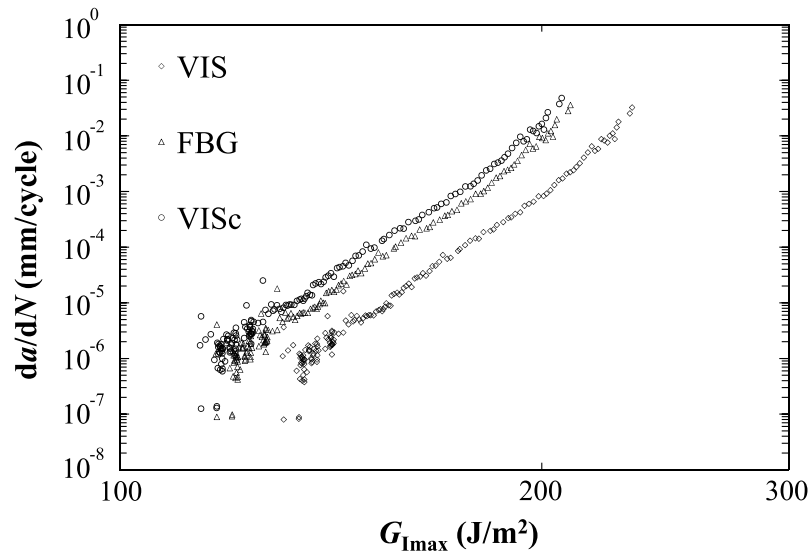
(b) Specimen FAT2

Figure 5.8: Crack length against the number of cycles (in logarithmic scale) for the VIS (from the edge) and FBG (center of the specimen) methods. Bigger markers indicate the experimental values and cross markers the difference between the measurements (Δa). The arrow indicates the axis where the data is referred to.

FBG curve. A constant increment correction ($\Delta a = ct$) would not bring both curves closer, indicating that the error introduced by the VIS method evolves with the test.



(a) Specimen FAT1



(b) Specimen FAT2

Figure 5.9: Fatigue crack propagation as a function of $G_{I\max}$ curves for FBG method, VIS method and corrected VIS method (VIS_c).

It is important to highlight that even though the exponent of the Paris law is well calculated by the VIS method, the error in the energy threshold reaches about 11%. This error is within the range of variability of the critical energy for different samples of the same material. However, taking into account that the error introduced by the VIS method is not random but systematic towards higher $G_{I\text{th}}$, and that it has been

produced in the analysis of one sample, it should not be disregarded. In terms of the design of composite structures, the consequences of the error of the VIS method depend on the design procedure. As the Paris law exponent in delamination fatigue tests is around 18-20, indicating a high sensitivity of the material to fatigue loads, most of the design procedures are addressed to avoid any fatigue damage. That is, to guarantee that any fatigue loading leads to an energy release rate below the threshold ($G_{\text{Imax}} < G_{\text{Ith}}$). Therefore, making use of G_{Ith} determined by the VIS method as design parameter would overestimate the damage resistance against fatigue loads.

On the other hand, design procedures based on limiting the crack growth, that is, assuring that the extension of the crack during the expected lifetime of the structure remains below a critical extension, would not be properly accounted for by the VIS method. Even though both methods provide the same exponent (m) in Eq. 5.1, the difference in the crack growth rate for a given loading, G_{Imax} , is about one order of magnitude. This work has shown that making use of the traditional visual methods for monitoring the crack growth during a mode I fatigue test under displacement control, leads to an incorrect estimation of the parameters required for fatigue design of composite structures.

5.4 Conclusions

A method for the interlaminar crack growth rate analysis in mode I fatigue tests using fibre Bragg grating sensors has been proposed and compared to the traditional methods, in which the crack length is monitored by optical devices. Both approaches have been applied to the study of carbon reinforced specimens.

Fibre Bragg grating sensors have been proved to be suitable tools for fatigue delamination monitoring because of their inherent accuracy and the fact that they monitor the crack from the inner part of the sample.

Even though both methods predict well the exponent m in the Paris law (a maximum relative error of 0.32% is found), the crack growth rates for a given load level are underestimated by one order of magnitude using the VIS method. In addition,

the threshold energy is overestimated, giving relative errors of about 11%. Both trends lead to unsafe structures if the VIS parameters are considered in the fatigue design.

The error of the VIS method emanates from the fact that the crack tip is determined by the observation of the specimen's edge, which is offset from the position of the crack front inside the specimen. It has been shown that the error on the crack tip location increases with the crack length and this fact deserves further investigation.

Chapter 6

Conclusions and future work

6.1 Introduction

According to Section 1.2, the main objective of the present work is to investigate the suitability of fibre Bragg grating sensors embedded in composite materials in order to monitor changes in the strain field of the host material and their applicability to detect delaminations in composite materials. In order to fulfil the global objective of this work, three partial aims are defined.

The first partial objective is to investigate the embedding conditions of FBG sensors to obtain reliable measurements of uniform strain fields. To fulfil this partial aim, numerical simulations have been performed and validated with experimental results. The influence of different parameters involving the embedment of FBGs on the strain measurements has been analysed. Spectral responses are presented as well to sustain the discussion of the reliability of the measurements, and a three dimensional model has been implemented to compare the response spectrum with that obtained in experimental tests.

With regards to the applicability of FBGs as delamination detectors, two different investigations have been undertaken. On the one hand, the suitability of FBGs to detect the crack tip in a mixed-mode delamination test has been experimentally investigated. Long FBGs were embedded into composite coupons that were then loaded under mixed-mode delamination. The experimental results are supported by

the proper numerical simulations. On the other hand, the applicability of FBGs for a real time delamination detection has been proved by means of experimental mode I fatigue delamination tests. In particular, the suitability of multiplexed FBGs as real time crack tip detectors has been experimentally investigated. In addition, the information obtained from the FBGs is used to analyse the effects of the crack tip monitoring in a fatigue test.

6.2 Conclusions

An in-depth state of the art study about FBG sensors has been developed. The most important works in recent years with FBGs as strain and temperature sensors have been reported. A large number of authors have concluded that it is desirable to have a clean response spectrum (i.e. not distorted, and no peak split observed) in order to make sure that the conversion from wavelength to strains or temperatures, fulfils the actual values present in the host material. FBGs have also been widely used as damage detectors. The main problem for an FBG close to a damaged zone is the non uniformity of the strain field. As explained, typical interrogation of FBG sensors only gives a spectral response. However, when the Bragg grating is subjected to an inhomogeneous strain field, the spectral response becomes distorted. As seen in the literature review, the use of the OLCR technique is one of the most important findings in recent years, because of its accuracy when positioning the sensors within the host structure, and because of its capability in obtaining a full reconstruction of the strain profile over the grating even for non uniform strain fields. In addition, if the OLCR interrogation of the FBGs is not available, the use of short multiplexed FBGs, where it can be assumed a uniform strain field that assesses a clean shift of the Bragg wavelength, would overcome the limitation of the non uniform strain fields.

In Chapter 3, a methodology to analyse the reliability of the response spectra of FBG sensors under uniform strain fields has been presented. The methodology was applied to laboratory specimens under longitudinal loading. The parameters involving the embedment of the sensors were analysed, and the influence of each parameter was checked. Finally, the optical response spectrum of each case was obtained by calculating the effective index of refraction values for the finite element

model of the FBG sensor and by using the T-matrix method. The axisymmetric finite element analysis results demonstrated that the most influential parameter on the FBG strain state for longitudinally tensile loaded specimens is the aspect ratio of the coupon. It has also been demonstrated that when interrogating embedded FBGs, it is important to make sure that the measurements given by the sensors are fulfilling the strain states of the host. In addition, it has also been demonstrated that when the transverse loads compared to longitudinal loads are not relevant, as in the case of UD composite specimens under longitudinal loading, the coating geometry and compliance have no effect on the precision of the measurements since there is no birefringence phenomenon to be accounted for. In other words, the use of a coating can be avoided in such cases in order to obtain higher sensibility in the FBG without losing any reliability of the measurement even though the optical fibre becomes more fragile.

In Chapter 4, a method for crack tip positioning in composite coupons under different mixed-mode I/II ratios has been presented. Several tests were carried out under different mode mixtures and the crack tip was precisely positioned at each of the tests with a long FBG sensor. In addition, this crack tip location has been proved to be at least as effective as the visual inspections during the test, and the precision of the location by means of axial strain profile has been improved by the use of the derivative of the axial strain being the maximum strain gradient perfectly localised. These results have been supported by the proper numerical simulations and visual inspection of the fracture surface after the test. Moreover, a method for obtaining the necessary parameters for the numerical modelling, i.e. the modes interaction parameter, has been presented. Finally, a method for fixture weight compensation was iteratively performed giving good results in terms of crack growth stability, including high mode ratios. It has also been proved that the effect of the embedded FBGs in the samples' mechanical properties is not significant, neither in the initial loading range nor in the propagation stage.

A method for the interlaminar crack growth rate analysis in mode I fatigue tests using multiplexed fibre Bragg grating sensors has been proposed in Chapter 5. This method was compared to the traditional methods, in which the crack length

is monitored by optical devices. Multiplexed fibre Bragg grating sensors have been proved to be suitable tools for fatigue delamination monitoring because of their inherent accuracy and the fact that they monitor the crack from the inner part of the sample. In addition, the use of multiplexed FBGs at a high data acquisition frequency has made precise real time monitoring of the crack length over a fatigue test possible. Even though both methods predict well the exponent m in the Paris law (a maximum relative error of 0.32% is found), the crack growth rates for a given load level are underestimated by one order of magnitude when using the traditional inspection methods. In addition, the threshold energy is systematically overestimated, giving relative errors of about 11%. Both trends lead to unsafe structures if the parameters obtained by the visual methods are considered in the fatigue design. To the best of this author's knowledge, the error in the visual inspection method emanates from the fact that the crack tip is determined by the observation of the specimen's edge, which is offset from the position of the crack front inside the specimen. It has been shown that the error in the crack tip location increases with the crack length, and this deserves further investigation.

6.3 Future works

The use of FBGs to sense non homogeneous strain fields and to monitor crack propagations in fracture specimens is still a field of research which needs to be further developed. As seen in Chapters 4 and 5, knowing the exact value of the axial strain component is not necessary when only changes are accounted for. In other words, when using FBGs to detect a delamination advance, there is no need to know the actual value of the strain, but rather the change promoted by a crack tip passing through. Nevertheless, there are still researchers using overly long FBGs subjected to non uniform strain fields, which even though is not necessarily negative, it is not recommendable. The most promising future works that emanate from this thesis are detailed below.

- From Chapter 3, the study should be extended to multidirectional laminates as such laminates are ultimately used in the production of composite structures. Performing a similar study on such laminates could give the answer to the

peak splitting phenomenon, a phenomenon caused by the non compensated transverse strains on the optical fibre.

- From Chapter 4, the reason why the v-shaped dip disappears when two fracture modes are interacting should be investigated and discussed. The derivative seemed to solve the problem of locating the crack tip, but there is an important question not yet answered about the meaning of the v-shaped dip.
- Linked to the previous point, it would seem that the v-shaped dip observed in the axial strain profiles of an interrogated sensor could contain useful information of the damage process zone. Long FBG sensors (or short FBGs in time domain) could give the answer to this matter. Further research with long FBGs embedded in different composite materials and interrogated under different loading conditions could help in the field of material characterisation.
- From Chapter 5, there is still a need to investigate the difference between the FBGs' measurements and the visual measurements that increase with the number of cycles in a mode I fatigue delamination test. Testing at controlled G , as well as testing at controlled load, could clarify this problem.
- From the results obtained in Chapters 4 and 5, it is deduced that the capabilities of FBGs for damage mode detection and material characterisation deserve further investigation. It seems possible to relate the cohesive zone to the axial strain profile of the sensor. In addition, the use of FBGs in a mixed-mode delamination could account for the detection of the failure mode throughout the test.
- Finally, the results obtained in Chapter 5 could be investigated to analyse whether the cohesive length varies throughout a fatigue test.

Bibliography

- [1] ASTM D 6671/D 6671M-06. Standard Test Method for Mixed Mode I-Mode II Interlaminar Fracture Toughness of Unidirectional Fiber Reinforced Polymer Matrix Composites. ASTM International. West Conshohocken PA, USA. 2006. DOI : 10.1520/D6671 – D6671M – 06, www.astm.org.
- [2] ASTM D 6115-97 (2011). Standard test method for mode I fatigue delamination growth onset of unidirectional fiber-reinforced polymer matrix composites. ASTM International. West Conshohocken PA, USA. 1997. DOI : 10.1520/D6115 – 97R11, www.astm.org.
- [3] ASTM D 5528 (2007). Standard test method for mode I interlaminar fracture toughness of unidirectional fiber-reinforced polymer matrix composites. ASTM International. West Conshohocken PA, USA. 2001. DOI : 10.1520/D5528 – 01R07E03, www.astm.org.
- [4] Hill, K.O., Meltz, G.. Fiber Bragg grating technology fundamentals and overview. *Journal of Lightwave Technology* 1997;15(8):1263–1276.
- [5] Eaton, N.C., Brew, R.C., Geiger, H.. Finite-element stress and strain analysis in composites with embedded optical-fiber sensors. *Smart Materials & Structures* 1995;4(2):113–117.
- [6] Li, H.N., Zhou, G.D., Ren, L., Li, D.S.. Strain transfer coefficient analyses for embedded fiber Bragg grating sensors in different host materials. *Journal of Engineering Mechanics-Asce* 2009;135(12):1343–1353.
- [7] Stutz, S., Cugnoni, J., Botsis, J.. Crack - fiber sensor interaction and characterization of the bridging tractions in mode I delamination. *Engineering Fracture Mechanics* 2011;78(6):890–900.

- [8] Stutz, S., Cugnoni, J., Botsis, J.. Studies of mode I delamination in monotonic and fatigue loading using FBG wavelength multiplexing and numerical analysis. *Composites Science and Technology* 2011;71(4):443–449.
- [9] Frövel, M., Pintado, J.M., Cabrerizo, F., Baráibar, I., Güemes, A.. Verificación de las mediciones de deformación de sensores de fibra óptica tipo Bragg embebidos en probetas de tracción de material compuesto Carbono/epoxi AS4/8552. In: VI Congreso Nacional de Materiales Compuestos. 2005, p. 469–476.
- [10] Frövel, M., Baráibar, I., Pintado, J.M., Stelzl, D., Güemes, A.. Performance evaluation of fibre Bragg gratings over a large temperature range. In: 5th International Workshop on Structural Health Monitoring. 2005, p. 654–661.
- [11] Steenkiste, R.J.V., Springer, G.S.. *Strain and Temperature Measurement with Fiber Optic Sensors*. Lancaster, Pennsylvania, USA: Technomic publishing company; 1997. ISBN 1-56676-480-7.
- [12] Butter, C.D., Hocker, G.B.. Fiber optics strain-gauge. *Applied Optics* 1978;17(18):2867–2869.
- [13] Tang, L.Q., Tao, X.M., Choy, C.L.. Effectiveness and optimization of fiber Bragg grating sensor as embedded strain sensor. *Smart Materials & Structures* 1999;8(1):154–160.
- [14] Emmons, M.C., Karnani, S., Trono, S., Mohanchandra, K.P., Richards, W.L., Carman, G.P.. Strain measurement validation of embedded fiber Bragg gratings. *International Journal of Optomechatronics* 2010;4(1):22–33.
- [15] Luyckx, G., Voet, E., Waele, W.D., Degrieck, J.. Multi-axial strain transfer from laminated cfrp composites to embedded Bragg sensor: I parametric study. *Smart Materials & Structures* 2010;19(10).
- [16] Voet, E., Luyckx, G., Waele, W.D., Degrieck, J.. Multi-axial strain transfer from laminated cfrp composites to embedded Bragg sensor: II experimental validation. *Smart Materials & Structures* 2010;19(10).

- [17] Hadjiprocopiou, M., Reed, G.T., Hollaway, L., Thorne, A.M.. Optimization of fibre coating properties for fiber optic smart structures. *Smart Materials & Structures* 1996;5(4):441–448.
- [18] Hadjiprocopiou, M., Reed, G.T., Hollaway, L., Thorne, A.M.. Optimisation of coating properties for fibre optic smart structures using finite element analysis. *Mathematics and Control in Smart Structures - Smart Structures and Materials* 1995;2442:109–120.
- [19] Liu, H.Y., Liu, H.B., Peng, G.D.. Tensile strain characterization of polymer optical fibre Bragg gratings. *Optics Communications* 2005;251(1-3):37–43.
- [20] Kuang, K.S.C., Kenny, R., Whelan, M.P., Cantwell, W.J., Chalker, P.R.. Embedded fibre Bragg grating sensors in advanced composite materials. *Composites Science and Technology* 2001;61(10):1379–1387.
- [21] Frövel, M., Gutiérrez, C., González, S., Carrión, G., Cabrerizo, F., Pintado, J.M.. Influence of temperature and humidity on the performance of fbg-strain sensors embedded in cfrp composites. In: *4th European Workshop on Structural Health Monitoring*. 2008, p. 393–400.
- [22] Frövel, M., del Olmo, E., Pintado, J.M.. Optical fibre Bragg grating sensors embedded in CFRP composites for structural health monitoring of aerospace structures. In: *Adaptronic Congress*. 2008, p. 61–73.
- [23] Frövel, M., Gutiérrez, C., González, S., Carrión, G., Cabrerizo, F., Pintado, J.M.. Dependence of the sensitivity of FBG-strain sensors embedded in CFRP composites on hydro-thermal conditions. In: Chang, F.K., editor. *6th International Workshop on Structural Health Monitoring*. ISBN 978-1-932078-71-8; 2007, p. 1283–1290.
- [24] Colpo, F., Humbert, L., Giaccari, P., Botsis, J.. Characterization of residual strains in an epoxy block using an embedded fbg sensor and the olcr technique. *Composites Part A-Applied Science and Manufacturing* 2006;37(4):652–661.
- [25] Sorensen, L., Botsis, J., Gmur, T., Cugnoni, J.. Delamination detection and characterisation of bridging tractions using long FBG optical sensors. *Composites Part A-Applied Science and Manufacturing* 2007;38:2087–2096.

- [26] Botsis, J., Humbert, L., Colpo, F., Giaccari, P.. Embedded fiber Bragg grating sensor for internal strain measurements in polymeric materials. *Optics and Lasers in Engineering* 2005;43(3-5):491–510.
- [27] Karalekas, D., Cugnoni, J., Botsis, J.. Monitoring of process induced strains in a single fibre composite using FBG sensor: A methodological study. *Composites Part A-Applied Science and Manufacturing* 2008;39(7):1118–1127.
- [28] Colpo, F., Humbert, L., Botsis, J.. An experimental numerical study of the response of a long fibre Bragg grating sensor near a crack tip. *Smart Materials & Structures* 2007;16:1423–1432.
- [29] Studer, M., Peters, K., Botsis, J.. Method for determination of crack bridging parameters using long optical fiber Bragg grating sensors. *Composites Part B-Engineering* 2003;34(4):347–359.
- [30] Mulle, M., Zitoune, R., Collombet, F., Olivier, P., Grunevald, Y.H.. Thermal expansion of carbon-epoxy laminates measured with embedded FBGS - comparison with other experimental techniques and numerical simulation. *Composites Part A-Applied Science and Manufacturing* 2007;38:1414–1424.
- [31] Guemes, J.A., Menendez, J.M.. Response of Bragg grating fiber-optic sensors when embedded in composite laminates. *Composites Science and Technology* 2002;62(7-8):959–966.
- [32] Prabhugoud, M., Peters, K.. Modified transfer matrix formulation for Bragg grating strain sensors. *Journal of Lightwave Technology* 2004;22(10):2302–2309.
- [33] Prabhugoud, M., Peters, K.. Finite element model for embedded fiber Bragg grating sensor. *Smart Materials & Structures* 2006;15(2):550–562.
- [34] Prabhugoud, M., Peters, K.. Finite element analysis of multi-axis strain sensitivities of Bragg gratings in PM fibers. *Journal of Intelligent Material Systems and Structures* 2007;18(8):861–873.
- [35] Prabhugoud, M., Peters, K.. Transverse strain sensitivity of fiber Bragg grating sensors. *Smart Structures and Materials: Smart Sensor Technology and Measurement Systems* 2005;5758:1–12.

- [36] Prabhugoud, M., Peters, K.. Birefringence and transverse strain sensitivity in Bragg grating sensors. *Sensing Issues in Civil Structural Health Monitoring* 2005;:433–442.
- [37] Colpo, F., Humbert, L., Botsis, J.. Characterisation of residual stresses in a single fibre composite with fbg sensor. *Composites Science and Technology* 2007;67(9):1830–1841.
- [38] Lai, M., Friedrich, K., Botsis, J., Burkhart, T.. Evaluation of residual strains in epoxy with different nano/micro-fillers using embedded fiber Bragg grating sensor. *Composites Science and Technology* 2010;70(15):2168–2175.
- [39] Carrión, G., Frövel, M., Pintado, J.M., Cabrerizo, F.. Extensive characterisation of the intrusiveness of fibre Bragg grating sensors embedded in a carbon fibre reinforced polymer. In: *4th European Workshop on Structural Health Monitoring*. 2008,.
- [40] Takeda, S., Okabe, Y., Yamamoto, T., Takeda, N.. Detection of edge delamination in cfrp laminates under cyclic loading using small-diameter fbg sensors. *Composites Science and Technology* 2003;63(13):1885–1894.
- [41] Guemes, J.A., Menendez, J.M., Frovel, M., Fernandez, I., Pintado, J.M.. Experimental analysis of buckling in aircraft skin panels by fibre optic sensors. *Smart Materials & Structures* 2001;10(3):490–496.
- [42] Takeda, S., Okabe, Y., Takeda, N.. Delamination detection in CFRP laminates with embedded small-diameter fiber Bragg grating sensors. *Composites Part A-Applied Science and Manufacturing* 2002;33(7):971–980.
- [43] Takeda, S., Minakuchi, S., Okabe, Y., Takeda, N.. Delamination monitoring of laminated composites subjected to low-velocity impact using small-diameter FBG sensors. *Composites Part A-Applied Science and Manufacturing* 2005;36(7):903–908.
- [44] Takeda, N., Yashiro, S., Okabe, T.. Estimation of the damage patterns in notched laminates with embedded FBG sensors. *Composites Science and Technology* 2006;66(5):684–693.

- [45] Yashiro, S., Murai, K., Okabe, T., Takeda, N.. Numerical study for identifying damage in open-hole composites with embedded FBG sensors and its application to experiment results. *Advanced Composite Materials* 2007;16(2):115–134.
- [46] Yashiro, S., Okabe, T., Toyama, N., Takeda, N.. Monitoring damage in holed CFRP laminates using embedded chirped FBG sensors. *International Journal of Solids and Structures* 2007;44(2):603–613.
- [47] Yashiro, S., Okabe, T., Takeda, N.. Damage identification in a holed CFRP laminate using a chirped fiber Bragg grating sensor. *Composites Science and Technology* 2007;67(2):286–295.
- [48] Takeda, S., Okabe, Y., Takeda, N.. Monitoring of delamination growth in CFRP laminates using chirped FBG sensors. *Journal of Intelligent Material Systems and Structures* 2008;19(4):437–444.
- [49] Prabhugoud, M., Pearson, J., Peters, K., Zikry, M.. Demonstration of failure identification methodology incorporating sensor degradation. *Smart Structures and Materials: Sensors and Smart Structures Technologies for Civil, Mechanical, and Aerospace Systems* 2004;5391:107–116.
- [50] Peters, K., Studer, M., Botsis, J., Iocco, A., Limberger, H., Salathe, R.. Embedded optical fiber Bragg grating sensor in a nonuniform strain field: Measurements and simulations. *Experimental Mechanics* 2001;41(1):19–28.
- [51] Peters, K., Pattis, P., Botsis, J., Giaccari, P.. Experimental verification of response of embedded optical fiber Bragg grating sensors in non-homogeneous strain fields. *Optics and Lasers in Engineering* 2000;33(2):107–119.
- [52] Peters, K., Studer, M., Botsis, J., Iocco, A., Limberger, H.G., Salathe, R.P.. Measurement of stress concentrations using embedded optical fiber Bragg grating sensors. *Smart Structures and Materials: Sensory Phenomena and Measurement Instrumentation for Smart Structures and Materials* 1999;3670:195–206.
- [53] Pearson, J., Prabhugoud, M., Zikry, M., Peters, K., Sitar, M., Davis, L.. Failure and damage identification in woven composites with fiber Bragg

- grating sensors. *Smart Structures and Materials: Sensors and Smart Structures Technologies for Civil, Mechanical, and Aerospace, Pts 1 and 2* 2005;5765:540–551.
- [54] Pearson, J., Prabhugoud, M., Zikry, M., Peters, K.. Damage progression identification in woven composites with fiber Bragg grating sensors. *Proceedings of the ASME Materials Division* 2005;100:49–57.
- [55] Pearson, J., Prabhugoud, M., Zikry, M., Peters, K.. In-situ failure identification in woven composites throughout impact using fiber Bragg grating sensors - art. no. 61742v. *Smart Structures and Materials: Sensors and Smart Structures Technologies for Civil, Mechanical, and Aerospace Systems, Pts 1 and 2* 2006;6174:V1742–V1742.
- [56] Prabhugoud, M., Peters, K.. Efficient interpretation algorithm for embedded Bragg gratings for damage detection in composites. *Smart Structures and Materials: Smart Sensor Technology and Measurement Systems* 2003;5050:159–170.
- [57] Prabhugoud, M., Peters, K.. Efficient simulation of Bragg grating sensors for implementation to damage identification in composites. *Smart Materials & Structures* 2003;12(6):914–924.
- [58] Sorensen, L.. The response of embedded FBG sensors to non-uniform strains in CFRP composites during processing and delamination. 2006.
- [59] Giaccari, P., Dunkel, G.R., Humbert, L., Botsis, J., Limberger, H.G., Salathe, R.P.. On a direct determination of non-uniform internal strain fields using fibre Bragg gratings. *Smart Materials & Structures* 2005;14(1):127–136.
- [60] Sorensen, L., Botsis, J., Gmur, T., Humbert, L.. Bridging tractions in mode I delamination: Measurements and simulations. *Composites Science and Technology* 2008;68(12):2350–2358.
- [61] Stutz, S.. Experimental and numerical studies of mode I and mode II delamination of polymer composites with embedded optical sensors. Ph.D. thesis; *École Polytechnique Fédérale de Lausanne*; 2011.

- [62] Epaarachichi, J.A., Canning, J., Stevenson, M.. The response of embedded NIR (830 nm) fiber Bragg grating sensors in glass fiber composites under fatigue loading. *Journal of Composite Materials* 2010;44(7):809–819.
- [63] Silva-Munoz, R.A., Lopez-Anido, R.A.. Structural health monitoring of marine composite structural joints using embedded fiber Bragg grating strain sensors. *Composite Structures* 2009;89(2):224–234.
- [64] Bernasconi, A., Carboni, M., Comolli, L.. Monitoring of fatigue crack growth in composite adhesively bonded joints using fiber Bragg gratings. 11th International Conference on the Mechanical Behavior of Materials 2011;.
- [65] Shin, C.S., Chiang, C.C.. Fatigue damage monitoring in polymeric composites using multiple fiber Bragg gratings. *International Journal of Fatigue* 2006;28(10):1315–1321.
- [66] Garrett, R., Pearson, J., Peters, K., Zikry, M.. Optimization of fiber Bragg grating sensor configurations for in situ failure identification in woven composites throughout impact. *Sensors and Smart Structures Technologies for Civil, Mechanical, and Aerospace Systems 2007, Pts 1 and 2* 2007;6529:U696–U707.
- [67] Garrett, R., Peters, K., Zikry, M.A., ASME, . Sensor networks for in-situ failure identification in woven composites throughout impact. *Proceedings of the Asme International Mechanical Engineering Congress and Exposition, Vol 10, Pts a and B* 2008;:203–210.
- [68] Garrett, R.C., Peters, K.J., Zikry, M.A.. In-situ impact-induced damage assessment of woven composite laminates through a fibre Bragg grating sensor network. *Aeronautical Journal* 2009;113(1144):357–370.
- [69] Lee, J.R., Ryu, C.Y., Koo, B.Y., Kang, S.G., Hong, C.S., Kim, C.G.. In-flight health monitoring of a subscale wing using a fiber Bragg grating sensor system. *Smart Materials & Structures* 2003;12(1):147–155.
- [70] Guemes, A., Fernandez-Lopez, A., Soller, B.. Optical fiber distributed sensing - physical principles and applications. *Structural Health Monitoring-an International Journal* 2010;9(3):233–245.

- [71] Sirkis, J.S., Dasgupta, A.. Optimal coatings for intelligent structure fiber optical sensors. *Fiber Optic Smart Structures and Skins III* 1990;1370:129–140.
- [72] Madsen, J.S., Jardine, A.P., Meilunas, R.J., Tobin, A., Pak, Y.E.. Effect of coating characteristics on strain transfer in embedded fiberoptic sensors. *Smart Sensing, Processing, and Instrumentation* 1993;1918:228–236.
- [73] Gutierrez, C., Rams, J., Frövel, M., Sans, D., Mayugo, J.A.. Sensores de fibra óptica grabados con redes de Bragg embebidos en un laminado Carbono/epoxi: estudio e implementación de un modelo opto-mecánico. In: *Proceedings of the V International Conference on Science and Technology of Composite Materials*. ISBN 978-84-692-5483-7; 2009, p. 265–268.
- [74] Szekrenyes, A., Uj, J.. Comparison of some improved solutions for mixed-mode composite delamination coupons. *Composite Structures* 2006;72(3):321–329.
- [75] Schipperen, J.H.A., de Borst, R.. A numerical analysis of mixed-mode delamination in carbon-epoxy prepregs. *Composite Structures* 2001;54(4):445–451.
- [76] Kim, B.W., Mayer, A.H.. Influence of fiber direction and mixed-mode ratio on delamination fracture toughness of carbon/epoxy laminates. *Composites Science and Technology* 2003;63(5):695–713.
- [77] Chen, J.H., Sernow, R., Schulz, E., Hinrichsen, G.. A modification of the mixed-mode bending test apparatus. *Composites Part A-Applied Science and Manufacturing* 1999;30(7):871–877.
- [78] Reeder, J.R., Crews, J.H.. Mixed-mode bending method for delamination testing. *AIAA Journal* 1990;28(7):1270–1276.
- [79] Blanco, N., Gamstedt, E.K., Costa, J., Trias, D.. Analysis of the mixed-mode end load split delamination test. *Composite Structures* 2006;76(1-2):14–20. 15th International Conference on Composite Materials (ICCM-15); JUN 27-JUL 01, 2005.
- [80] Renart, J., Blanco, N., Pajares, E., Costa, J., Lazcano, S., Santacruz, G.. Side clamped beam (scb) hinge system for delamination tests in beam-type

- composite specimens. *Composites Science and Technology* 2011;71(8):1023–1029.
- [81] Bonhomme, J., Arguelles, A., Vina, J., Vina, I. Fractography and failure mechanisms in static mode i and mode ii delamination testing of unidirectional carbon reinforced composites. *Polymer Testing* 2009;28(6):612–617.
- [82] Meltz, G., Morey, W.. Bragg grating formation and germanosilicate fiber photosensitivity. In: *International workshop on photoinduced self-organization effects in optical fiber*. 1992,.
- [83] Turon, A., Camanho, P.P., Costa, J., Renart, J.. Accurate simulation of delamination growth under mixed-mode loading using cohesive elements: Definition of interlaminar strengths and elastic stiffness. *Composite Structures* 2010;92(8):1857–1864.
- [84] Turon, A., Camanho, P.P., Costa, J., Davila, C.G.. A damage model for the simulation of delamination in advanced composites under variable-mode loading. *Mechanics of Materials* 2006;38(11):1072–1089.
- [85] Turon, A., Costa, J., Camanho, P.P., Davila, C.G.. Simulation of delamination in composites under high-cycle fatigue. *Composites Part A-Applied Science and Manufacturing* 2007;38(11):2270–2282.
- [86] Hojo, M., Matsuda, S., Tanaka, M., Ochiai, S., Murakami, A.. Mode I delamination fatigue properties of interlayer-toughened CF/epoxy laminates. *Composites Science and Technology* 2006;66(5):665–675.
- [87] Arguelles, A., Vina, J., Canteli, A.F., Castrillo, M.A., Bonhomme, J.. Interlaminar crack initiation and growth rate in a carbon-fibre epoxy composite under mode-I fatigue loading. *Composites Science and Technology* 2008;68(12):2325–2331.
- [88] Cvitkovich, M.K., O'Brien, T.K., Minguet, P.J.. Fatigue debonding characterization in composite skin/stringer configurations. *Composite Materials: Fatigue and Fracture, Seventh Volume* 1998;1330:97–121.

- [89] Hojo, M., Ochiai, S., Gustafson, C.G., Tanaka, K.. Effect of matrix resin on delamination fatigue-crack growth in CFRP laminates. *Engineering Fracture Mechanics* 1994;49(1):35–47.
- [90] Stelzer, S., Brunner, A.J., Argueelles, A., Murphy, N., Pinter, G.. Mode I delamination fatigue crack growth in unidirectional fiber reinforced composites: Development of a standardized test procedure. *Composites Science and Technology* 2012;72(10):1102–1107.
- [91] Brunner, A.J., Murphy, N., Pinter, G.. Development of a standardized procedure for the characterization of interlaminar delamination propagation in advanced composites under fatigue mode I loading conditions. *Engineering Fracture Mechanics* 2009;76(18):2678–2689.
- [92] Paris, P., Gomez, M., Anderson, W.. A rational analytical theory of fatigue. *Trend Eng* 1961;13:9–14.
- [93] Paris, P., Erdogan, F.. Critical analysis of propagation laws. *J Basic Eng* 1963;85:528–34.
- [94] Hojo, M., Tanaka, K., Gustafson, C.G., Hayashi, R.. Effect of stress ratio on near-threshold propagation of delamination fatigue cracks in unidirectional CFRP. *Composites Science and Technology* 1987;29(4):273–292.
- [95] Sans, D., Stutz, S., Renart, J., Mayugo, J.A., Botsis, J.. Crack tip identification with long FBG sensors in mixed-mode delamination. *Composite Structures* 2012;94(9):2879–2887.
- [96] Vicens J, Renart J, Budhe S, Costa J. Compliance real time monitoring in delamination fatigue tests. 2013. Submitted.
- [97] Vicens J, Costa J, Renart J, Turon A. New method to real time monitoring of specimens compliance in mode II delamination tests. OCT-2008. 4th International Conference on Composites Testing and Model Identification (COMPTEST-08).
- [98] Hashemi, S., Kinloch, A.J., Williams, J.G.. The analysis of interlaminar fracture in uniaxial fibre-polymer composites. In: *Proceedings of the Royal*

Society of London series A-Mathematical and Physical Sciences; vol. 427. 1990, p. 173–199.

- [99] Williams, J.G.. End corrections for orthotropic DCB specimens. *Composites Science and Technology* 1989;35:367–376.